APPLICATION OF A THERMAL FIELD EMISSION SOURCE

FOR SCANNING AUGER MICROSCOPY

David W. Tuggle
B.S., Oregon State University, 1974

A thesis submitted to the faculty
of the Oregon Graduate Center
in partial fulfillment of the
requirements for the degree
Master of Science
in
Applied Physics

January 21, 1981

The thesis "Application of a Thermal Field Emission Source for Scanning Auger Microscopy" by David W. Tuggle has been examined and approved by the following Examination Committee:

LYNWOOD W. SWANSON
Professor
Thesis Research Advisor

RICHARD A. ELLIOTT
Associate Professor

JONATHAN H. ORLOFF
Associate Professor

DOUGLAS F. BAROFSKY
Associate Professor

ACKNOWLEDGMENTS

I would like to thank my thesis advisor, Dr. Lynwood W. Swanson, for giving me the benefit of his considerable expertise in the areas of field emission and surface physics and also for the opportunity to observe first-hand the sort of critical scientific thinking which is what this business is all about. I would also like to thank Dr. Jonathan H. Orloff who did the initial electron optical design for the column, and whose knowledge of electron optics, enthusiasm for scientific work and encouragement I have been able to rely on throughout this project.

Mr. Noel Martin of FEI Co. Inc. built the electron gun and did all of the precision machine work associated with the project. Mr. J. E. Wolfe and Mr. W. Bennett, formerly of Burroughs Corp., were very helpful in advising us how to get the "bugs" out of the system. They also helped with the video electronics. I wish to express my thanks to Mr. Doug Jones of Tektronix, Inc. for his help with the magnetic shielding and for advice on Auger spectroscopy. Tektronix permitted us to use their computer for the electron optical calculations.

I would like to thank Bev Kyler and Nancy Christie for typing this thesis and for keeping after me to finish it. Finally, I would like to express my gratitude to my parents, who have always been there when I needed them.

TABLE OF CONTENTS

LIST OF TABLES

LIST OF FIGURES

ABSTRACT

Application of a Thermal Field Emission Source

for Scanning Auger Microscopy

David W. Tuggle, M.S.
Oregon Graduate Center, 1981

Supervising Professor: Lynwood W. Swanson

A thermal field emission (TFE) electron source has been incorporated into a microprobe with two magnetic lenses to produce a 0.10 μm beam spot with 0.11 μA current at 12 kV and a working distance of 13 cm, in agreement with calculated performance assuming a source angular intensity of 1 mA sr^{-1}.

Experience with cold field emitters has discouraged their use in many applications because of noise problems, instability, short life, and extreme vacuum requirements. The TFE mode of operation allows a relaxation of vacuum requirements by rapid thermal annealing of sputter-induced surface deformation, thereby minimizing the probability of emitter destruction by a regenerative vacuum arc. Additionally, the high emitter temperature maintains a low and constant coverage of adsorbed gases on the emitter surface thereby eliminating time dependent work function change.

The emitter used was <100> oriented W coated with Zr, operated at 1800 K. The microprobe was used to construct a scanning Auger

microscope which produced submicron resolution Auger elemental maps with scan times of 5 min or less.

The high voltage Zr/W<100> TF emitter not only exhibits long life ($\sim$ 5000 h on several tests), but sufficiently low noise (e.g., 0.23%) to be used in SAM applications without the need for sophisticated beam current stabilization schemes. Specimen current densities which far exceed SAM requirements can be obtained at 0.1 μm spot size with relatively simple gun optics. At present a current density of 1300 A/cm^2 or power density of 1.6×10^7 W/cm^2 has been achieved in a 0.1 μm beam spot. This corresponds to an image plane brightness of 5.5×10^7 A cm^{-2} sr^{-1} at 12 kV. The geometric stability of the emitter structure is excellent once it achieves equilibrium temperature. Measurements show the emitter drift over 16 h periods to be < 0.05 μm/h for a TFE emitter operating at 1800 K.

CHAPTER 1

INTRODUCTION

The purpose of the work presented in this thesis is to demonstrate the characteristics of an electron microprobe using a zirconiated tungsten thermal field emission (TFE) electron source. The specific application of this microprobe to scanning Auger surface analysis is only one of many possible applications of this electron source. Field emitters are inherently high brightness electron sources due to their small virtual source size and high current density. They are capable of delivering orders of magnitude more current into submicron focused spots than thermionic cathodes.

Several authors[1-4] have combined a scanning electron microscope (SEM) with an Auger electron spectrometer to determine the spatially resolved surface chemistry of a specimen. Since typical SEMs deliver less than a nanoamp to the specimen and the Auger process is typically very low yield (10^{-4}), plus CMA electron spectrometers have a transmission of only about 15% at most, the Auger signal is so weak that extremely long data acquisition times are required. Commercial instruments[5,6] designed specifically for Auger analysis and using a LaB_6 thermionic pointed cathode can deliver beam currents on the order of a nanoamp at high spatial resolution and therefore have a better signal to noise (S/N) ratio than the modified SEMs. Field emitters, due to their extreme brightness, can deliver 10 to 100 nA

into the same size spot as the LaB_6 cathode, and thereby increase the Auger S/N ratio (see Figure 1-1). The only reservations toward using a field emission (FE) source are that these sources typically have a reputation for instability and noise, and at high current densities an energy spread in the emitted beam occurs which could cause an increase in focused spot size.

There are several advantages in operating a field emitter at an elevated temperature (the thermal-field mode), one of which is a reduction in beam noise. The emitter used in this instrument is

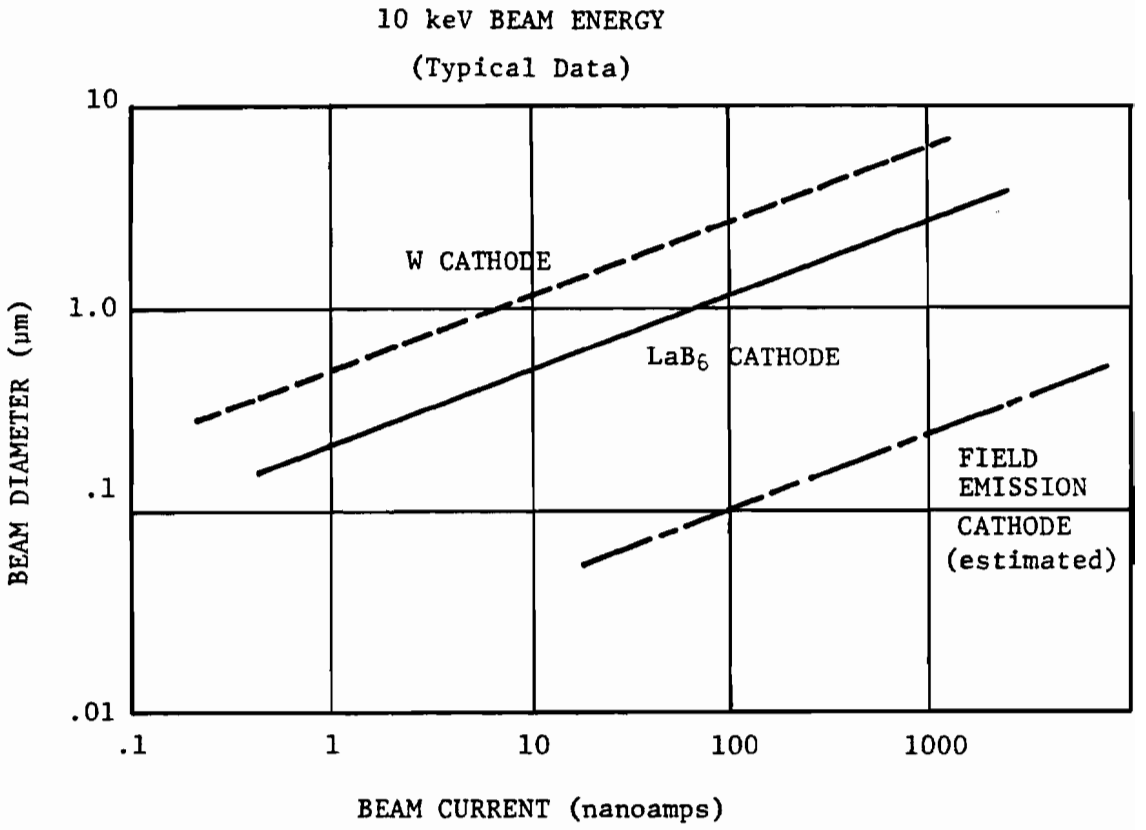

Figure 1-1. Beam diameter vs. beam current.

operated at 1800 K. It is a <100> oriented electrochemically etched tungsten wire on which zirconium has been deposited. The net effect of the <100> orientation and the zirconium adsorption is to create a low work function (100) plane at the emitter tip. This results in the electron emission being confined to a half-angle of less than 9 degrees,[7] which decreases total current required for a given axial brightness, as compared to unconfined field emission sources.

Table 1-1[8] is a comparison of thermionic, field and photo cathode electron sources. It can be seen that the zirconiated tungsten <100> oriented (Zr/W<100>) thermal field electron (TFE) emitter has a brightness orders of magnitude above any of the other cathodes. The scanning Auger microscope (SAM) described here has been designed[9] to incorporate the Zr/W<100> TFE source. Beam noise, stability, mechanical drift, spot size and I-V data have been measured for the source and electron optics. Auger spectra have been obtained and scanning Auger elemental maps have been recorded.

The first part of this thesis comprises a review of electron optics, cathode characteristics and Auger spectroscopy. The last part covers the specifics of this particular experimental system and the results and conclusions derived from the system.

TABLE 1-1

CATHODES AND THEIR PROPERTIES

Type of Emission	Type of Cathode	Emission, A/cm^2	Operating Temperature, T_c	Upper Pressure Limit, Torr	β $A/cm^2/sr$ at 20 kV
Thermionic	W	0.6	2470	10^{-4}	1.8×10^4
		7.3	2700		1.9×10^5
Thermionic	Ta	0.5	2300	10^{-5}	1.6×10^4
Thermionic	Rh	0.2	2300	10^{-4}	6.5×10^3
Thermionic	Thoriated W	1-3	2000	5×10^{-6}	$3.75 \times 10^4 \rightarrow 1.1 \times 10^5$
Thermionic	Oxide coated	0.5	1100	10^{-6}	3.4×10^4
Thermionic	Dispenser	0.5 to 6	1150 to 1400	5×10^{-6}	$3.3 \times 10^4 \rightarrow 3.2 \times 10^5$
Thermionic	LaB_6	20.4	2100	10^{-6}	9.5×10^5
Field	Single x-tal W	Up to 10^4	Room	10^{-10}	10^8
Temp-field	Zirconiated W		1400 to 1800	10^{-9}	10^{10}
Photo	Pd	2×10^{-5}	Room	10^{-7}	2×10^{-1}
Photo	CsI	5×10^{-6}	Room	10^{-4}	2×10^{-1}

REFERENCES

1. W. C. MacDonald, "Scanning Electron Microscopy," 4, (IITRI, Chicago, 1971), p. 89.
2. M. P. Seah and C. Lea, "Scanning Electron Microscopy: Systems and Applications," (Newcastle, 1973), p. 276-281.
3. E. K. Brandis, "Scanning Electron Microscopy," (IITRI, Chicago, 1975), p. 141.
4. A. Christou, "Scanning Electron Microscopy," 8, (IITRI, Chicago, 1975), p. 149.
5. Physical Electronics Model 590 Scanning Auger Microprobe.
6. JEOL JAMP-10 Auger Microprobe.
7. L. W. Swanson and L. C. Crouser, J. Appl. Phys. 40, 4741 (1969).
8. K. Amboss, "Scanning Electron Microscopy," 9, (IITRI, Chicago, 1976), p. 699.
9. Initial electron optical design by J. H. Orloff.

CHAPTER 2

ELECTRON OPTICS

A. Introduction

All electrostatic and magnetic fields of either axial or plane symmetry possess the properties of optical lenses. This fact allows the use of light optical concepts, such as aberrations, cardinal points, etc. to be used to describe an electrostatic or magnetic electron lens. In fact a direct mathematical analogy between optical refractive index and electrostatic field potential exists. A somewhat less direct connection between refractive index and magnetic flux also exists.

Before the widespread use of high speed digital computers, a great deal of work was done with the few lens geometries for which analytical expressions could be written and solved for the axial field. The results, expressed in terms of focal lengths and aberration coefficients, gave electron optical designers some guidelines as to how to minimize aberrations while obtaining the desired focusing properties. Electrolytic tanks and resistor network analogs were used to obtain lens fields for a wider class of lenses, but with limited accuracy. Finite difference and finite element digital computer solutions for Laplace's equation now permit any lens geometry to be tested for its characteristics before it is built. These

techniques also allow the calculation of electron trajectories for non-paraxial electron rays. Munro[1] has carried the computer technique one step further and written a program which automatically modifies the lens geometry after each calculation to minimize the sum of the squares of the aberration coefficients.

The first sections of this chapter deal with glass optics. Then a review of magnetic lens electron optics is presented and finally two topics are covered which are peculiar to electron optics, quadrupole lenses and deflection systems.

B. Gaussian Imaging

Conventional geometrical optics is based on Snell's law, $n_1 \sin \theta_1 = n_2 \sin \theta_2$, which relates the angles of incidence (θ_1) and refraction (θ_2) at an interface between two media of different refractive indices, n_1 and n_2. This law can be derived from the definition of the refractive index $n_1 = c/v_1$, where c = speed of light in a vacuum and v_1 = speed of light in medium with index n_1, and the condition of wavefront continuity at the interface between n_1 and n_2. In order to obtain manageable equations relating the incident and transmitted rays in an optical system, the sine function in Snell's law is expanded in a Maclaurin expansion as follows:

$$\sin \theta = \theta - \frac{\theta^3}{3!} + \frac{\theta^5}{5!} - \frac{\theta^7}{7!} + \cdots \qquad (2\text{-}1)$$

Approximating Snell's law by $n_1 \theta_1 = n_2 \theta_2$ (first order theory), one obtains aberration free imaging or Gaussian imaging. Since we

will not be concerned with mirrors or single refracting surfaces, but rather with lenses, we can proceed directly to the analysis of a glass lens with spherical surfaces.[2]

In Figure 2-1, a lens with refractive index n_2 is immersed in a medium with index n_1. The light ray proceeds along the path ACFE. The centers of curvature for the lens surfaces are at points D and B.

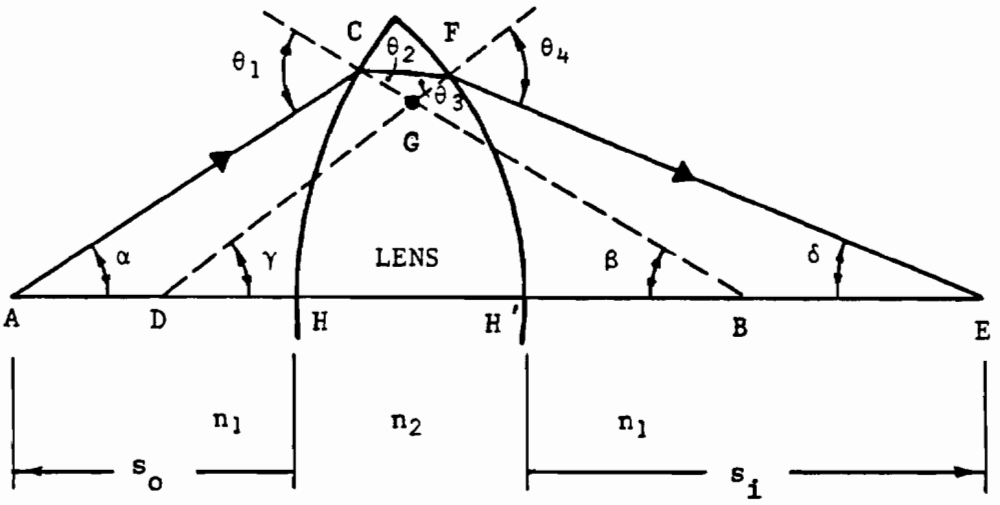

Figure 2-1. Glass lens.

Regarding the trangles ABCA and DEFD we can state immediately

$$\alpha + \beta = \theta_1 \quad \text{and} \quad \gamma + \delta = \theta_4 \ . \tag{2-2}$$

The triangles DBGD and CGFC have an angle in common. Thus, the sum of the other two angles in each triangle is equal to this common angle,

$$\gamma + \beta = \theta_2 + \theta_3 \ .$$

Applying the first order approximation to Snell's law at the lens surfaces yields

$$n_1 \theta_1 = n_2 \theta_2 \quad \text{and} \quad n_2 \theta_3 = n_1 \theta_4 .$$

Combining these gives

$$\theta_1 + \theta_4 = (n_2/n_1)(\theta_2 + \theta_3) .$$

Substituting for θ_1 and θ_4 from equation 2-2, we have

$$\alpha + \delta = (n_2/n_1 - 1)(\gamma + \beta) .$$

Using the object and image distances as defined in the diagram and noting that BC = r_1 and DF = r_2, the radii of curvature for the lens surfaces, for small angles we can write

$$a \cong CH/s_o \qquad \beta \cong CH/r_1$$

$$\gamma \cong FH'/r_2 \qquad \delta \cong FH'/s_i$$

Also, for small angles and thin lenses we can write

$$CH \cong FH'$$

Collecting the last three sets of equations into one yields

$$\frac{1}{s_o} + \frac{1}{s_i} = \left(\frac{n_2}{n_1} - 1\right)\left(\frac{1}{r_1} + \frac{1}{r_2}\right) . \qquad (2\text{-}3)$$

This is known as the lens maker's equation. If the right hand side of the equation is replaced by 1/f, where f is the focal length, then in this thin lens approximation, the focal lengths for both the image and the object sides of the lens are the same, a condition not true in general.

In general, if $s_o \to \infty$ then $1/s_i \to 1/f_i$ and if $s_i \to \infty$ then $1/s_o \to 1/f_o$ where f_i and f_o are the image object space focal lengths, respectively. The object or image distances approaching ∞ correspond to rays parallel to the optical axis.

We have established that rays entering the lens parallel to the axis all converge to a point at f_i and that rays leaving the point f_o at any angle are collimated and emerge parallel to the axis. From these two facts the object and image distances and corresponding magnification can be obtained through use of Figure 2-2 and by applying a simple "lever arm rule."

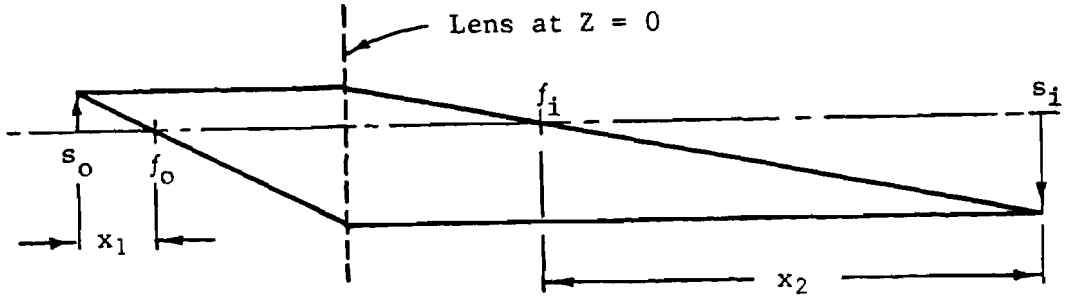

Figure 2-2. Magnification diagram.

$$\frac{1}{s_o} + \frac{1}{s_i} = \frac{1}{f} \qquad m = \frac{s_i}{s_o} \tag{2-4}$$

This is known as the Gaussian formula in optics; an equivalent statement $x_1 x_2 = f^2$ and $m = -f/x_1 = -x_2/f$ is known as the Newtonian formula.

C. Aberrations

If we include the second term in the expansion of sin θ in Snell's Law,

$$\sin \theta \cong \theta - \theta^3/3!$$

we obtain imperfect imaging (third order theory). There is some confusion regarding the order of various aberrations. Regarding the expansion of sin θ as determining the order of the aberrations, there are only third, fifth, seventh, etc. order aberrations.[3] However, some authors refer to the dependence of the aberration on the power of either the ray height as it enters the lens or the aperture angle as determining the order of the aberration. Additionally, calculations which determine the caustic cross section (blur diameter) in terms of the deviations of a wavefront from spherical symmetry are based on the order of terms in a polynomial expansion of the wavefront.[4] Born and Wolf[5] refer to the distinction between wave aberrations, based on the optical path length error as a function of Cartesian coordinates which yields fourth, sixth, eighth, etc. order

aberrations and ray aberrations, which are of third, fifth, etc. order in the coordinates.

The primary image defects, obtained by using $\theta - \theta^3/3!$ for $\sin\theta$ in Snell's Law, were first investigated by Seidel.[6] He expressed the deviation of a ray from the path prescribed by the Gaussian formulas in terms of five sums, the Seidel sums. The magnitude of each sum is proportional to the magnitude of characteristic and identifiable aberrations observed in the image plane of the optical system. These are called spherical aberration, coma, astigmatism, Petzval curvature (usually called curvature of field) and distortion. The following paragraphs sketch the results of third order theory.

Spherical aberration is caused by the difference in focal lengths for rays close to the axis (paraxial) and rays close to the edge (marginal) of the lens. Figure 2-3 illustrates this aberration.

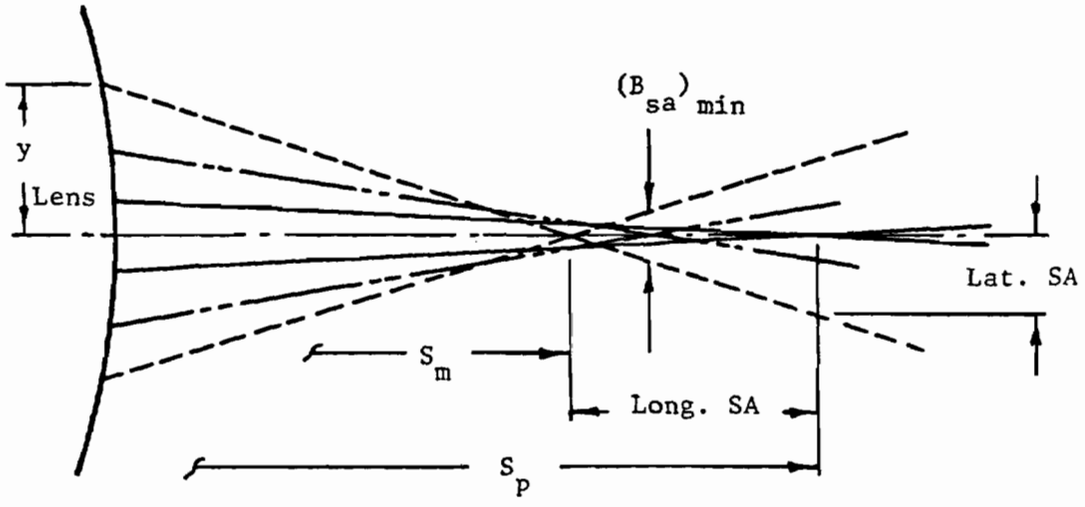

Figure 2-3. Spherical aberration.

The magnitude of this aberration can be measured by the difference in focal points between paraxial and marginal rays (longitudinal S.A.) or by the radius of the blur circle at the paraxial focal point (lateral S.A.). Additionally, the aberration can be expressed in terms of the minimum blur diameter,

$$(B_{sa})_{min} = \frac{1}{2} \text{ Lat SA} = \frac{1}{2} (y/s_p) \text{ Long SA},$$

which occurs at a distance 3/4 of the way between the paraxial and marginal foci. Angular blur is also useful, being defined as

$$\beta_{sa} = (B_{sa})_{min}/s_p = \frac{1}{2} (y/s_p^2) \text{ Long SA}.$$

Longitudinal S.A. varies in proportion to the square of the semi-aperture and lateral SA varies as the cube of the semiaperture. A point source is imaged as a bright spot surrounded by a halo.

Coma is due to a variation in lateral magnification for paraxial and marginal rays. The marginal rays are imaged either closer to or further from the optical axis, resulting in a point object appearing as a point image with a comet-like tail extending either toward or away from the optical axis (negative or positive coma). In Figure 2-4 the comatic image is drawn and next to it is shown the lens aperture.[7] Ray locations in the aperture and image planes are shown by corresponding letters. Note that rays going around the aperture circle once go around the image circle twice. The measures of coma are the tangential coma and sagittal coma, indicated in the figure.

The sagittal coma is one-third the value of the tangential coma. Coma is proportional to the square of the semiaperture and directly proportional to the field size (distance away from the axis).

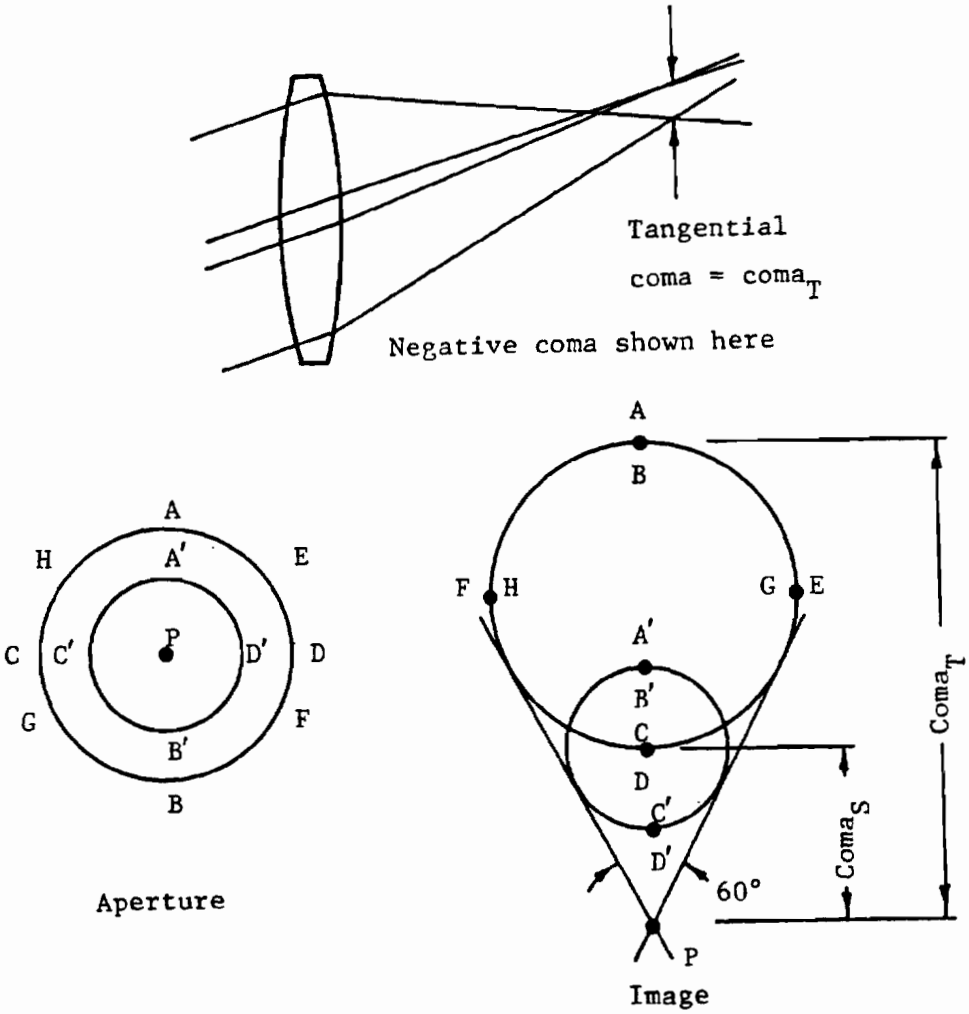

Figure 2-4. Coma

Astigmatism is another off-axis aberration caused by the tangential and sagittal fan of rays for an off-axis object point imaging in different planes. If one cuts through a spherical surface at a non-normal angle with a fan of rays, the rays encounter different surface curvatures depending on their orientation. In Figure 2-5, the tangential rays (which form lines in directions tangent to a circle in the image space) come to a focus closer to the lens than the sagittal (or radial) rays.

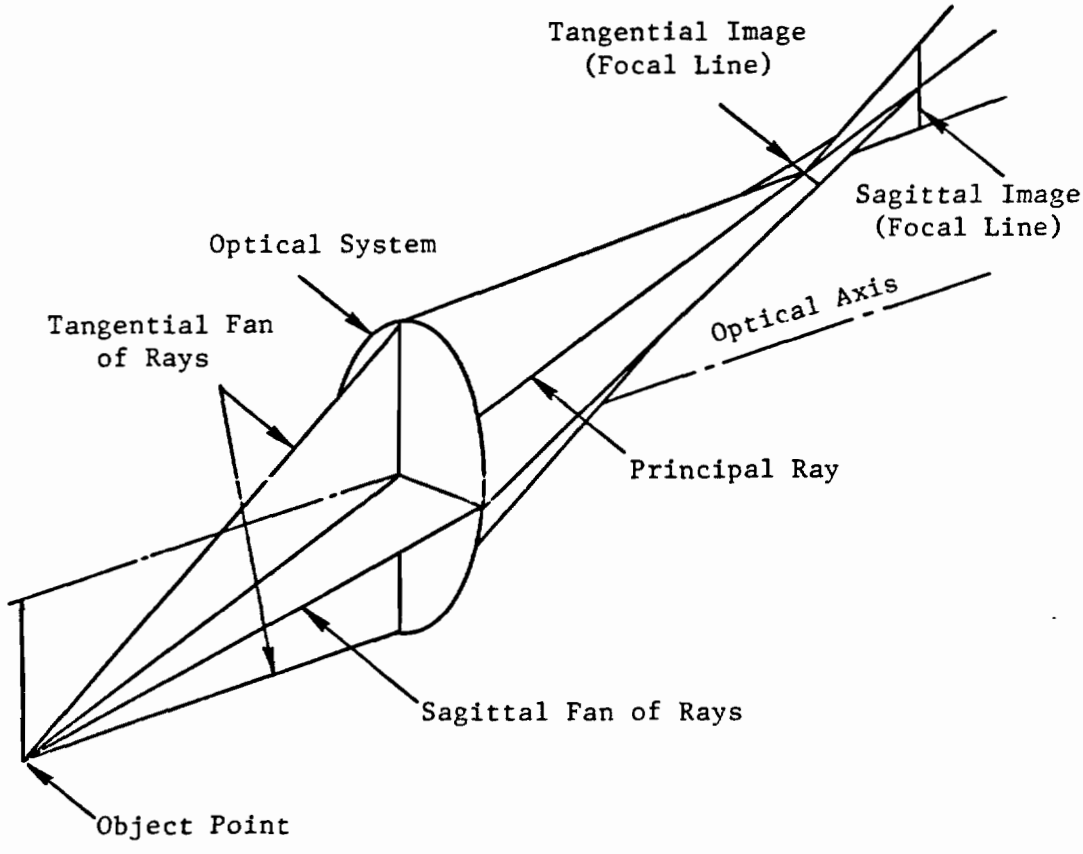

Figure 2-5. Astigmatism.[7]

This is called undercorrected astigmatism, as distinguished from the case of a closer sagittal focus which is overcorrected. A point object is imaged as two lines, between which the image appears as an elliptical or circular blur. The magnitude of the difference between the tangential and sagittal focal surfaces is dependent on the square of the field size. Also, the length of the lines is proportional to the aperture size.

Petzval curvature or field curvature is a curvature of the image surface in the absence of astigmatism. Figure 2-6 indicates the Petzval surface for both positive and negative lenses, as well as the further curvature and splitting of the image surface into tangential and sagittal surfaces if astigmatism is also present. The magnitude of the deviation from a plane is proportional to the square of the field size.

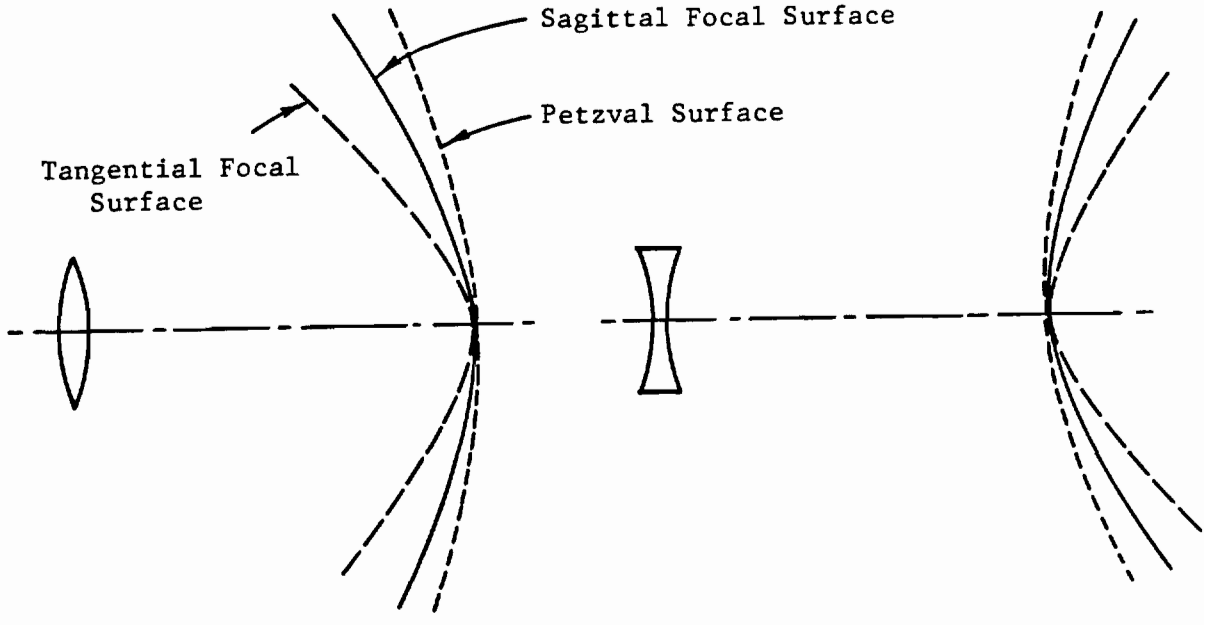

Figure 2-6. Field curvature.

Distortion is a variation in linear magnification with off-axis distance in the image surface. An increase in magnification with image height is called pin cushion distortion; the opposite is called barrel distortion. The magnitude of distortion is proportional to the cube of the image height (see Figure 2-7).

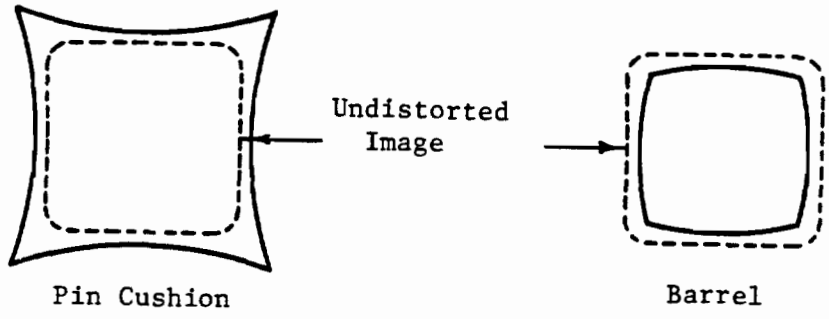

Figure 2-7. Distortion.

The five Seidel aberrations have been considered for the monochromatic case only. Since the index of refraction varies with wavelength or color of the light, the five monochromatic aberrations are affected by chromatic aberration as well. Longitudinal chromatic aberration (in the absence of the other aberrations) is the distance between the focal points for the shortest and longest wavelengths in the incident light. Lateral chromatic aberration is the difference in magnification of a lens for differing wavelengths (see Figure 2-8).

Table 2-1 (from Smith[8]) summarizes the aberrations and their dependence on the semiaperture y and the image height h.

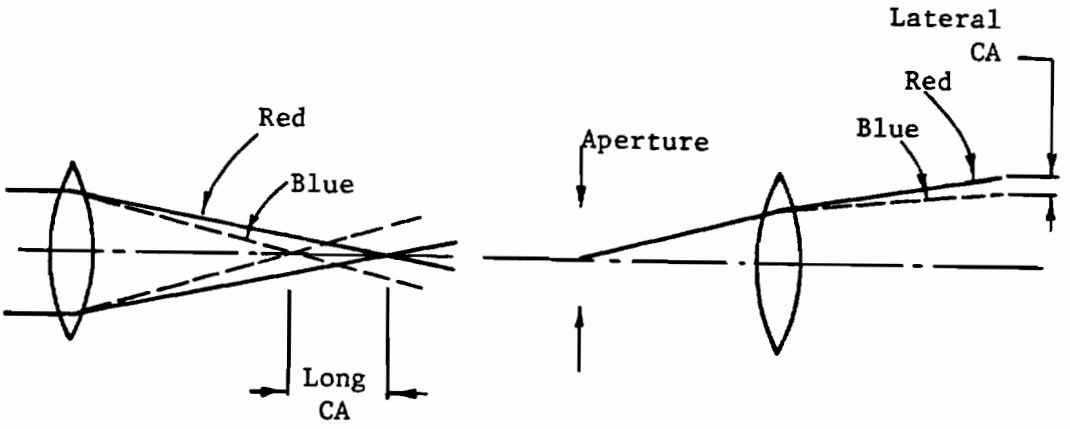

Figure 2-8. Chromatic aberration.

TABLE 2-1

OPTICAL ABERRATIONS

Aberration	vs. Aperture	vs. Field Size
Spherical (long.)	y^2	-
Spherical (lateral)	y^3	-
Coma	y^2	h
Petzval curvature	-	h^2
Astigmatism	-	h^2
Length of astigmatic lines	y	h^2
Distortion (linear)	-	h^3
Distortion (percentage)	-	h^2
Axial chromatic (long.)	-	-
Lateral chromatic	-	h

D. Cardinal Points of a Lens

Before proceeding any further, it is necessary to define some terms which will be used later. Figure 2-9 shows the cardinal points of a lens. Positive distances are shown by the arrows. The subscript o denotes the object side; i denotes the image side of the lens. Further subscripts will be used as follows:

p = Paraxial; m = Marginal; 1,2,3, *etc.* = *first, second, third* lens in a system.

P_o and P_i are the object and image principal points. The principal planes are shown by the dotted lines. These are the planes where the effective change in direction occurs for the rays passing through the respective focal points. For a thin lens P_o and P_i are coincident and $f_o = f_i$. Notice that the physical lens is not shown. If distances are referred to a physical point on the lens, then the object and image distances are usually denoted by z_o and z_i, and the distances to the principal planes are z_{po} and z_{pi}.

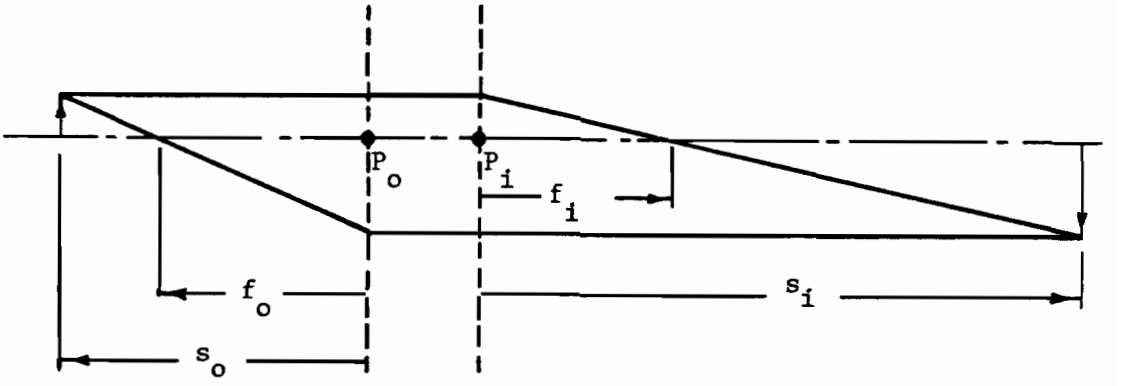

Figure 2-9. Cardinal points.

E. Relaying Spherical Aberration

If we have a sequence of lenses, it becomes necessary to determine how the individual aberrating elements affect the final image. We will only investigate spherical aberration effects in this section, since for our application spherical and chromatic will be the only significant aberrations which cannot be corrected or minimized in some way.

Consider an optical system in which a point object is imaged to a point image (on axis) via a two lens collimating system, as shown in Figure 2-10. Let each lens have positive spherical aberration (marginal rays are focused closer to the lens than paraxial rays). We can use the Gaussian formula for the paraxial rays and for the

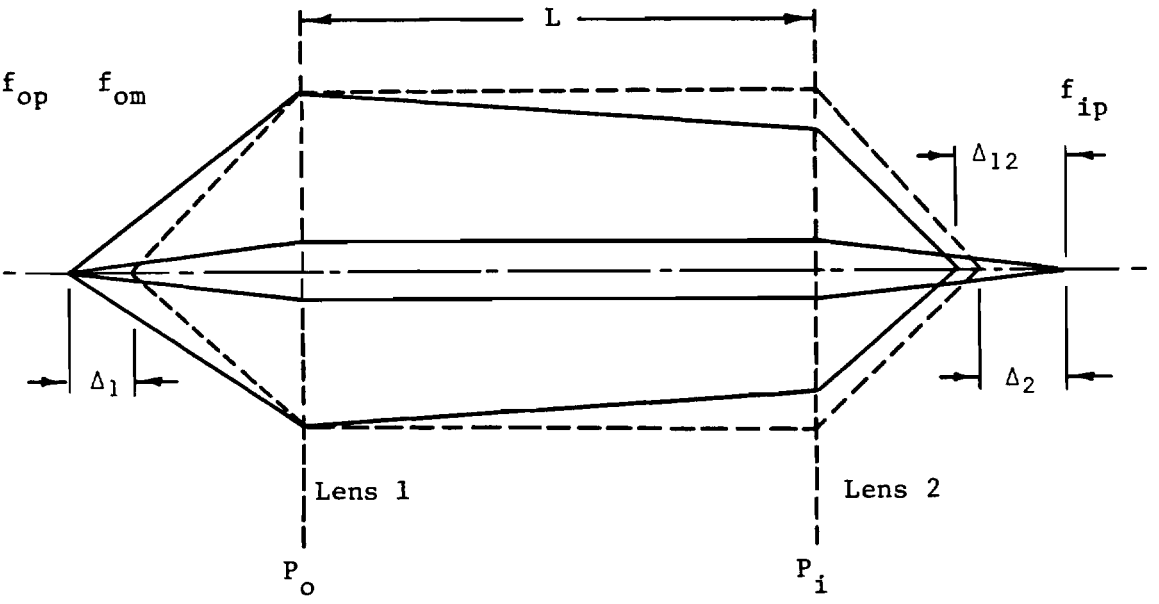

Figure 2-10. Relaying spherical aberration (Case 1). (Both lenses)

marginal rays, providing we use a different focal length. For the paraxial rays of the first lens,

$$\frac{1}{f_{op}} = \frac{1}{s_{op}} + \frac{1}{s_{ip}} = \frac{1}{s_{op}} + \frac{1}{\infty} = \frac{1}{s_{op}} \quad . \tag{2-5}$$

For the dotted lines, which define Δ_l, the longitudinal spherical aberration (Long. SA) of the first lens referred to the object side, we have

$$\frac{1}{f_{om}} = \frac{1}{f_{op} - \Delta_l} = \frac{1}{s_{om}} \quad . \tag{2-6}$$

For the solid marginal lines which converge upon leaving the first lens, and which are the actual marginal rays from a point source detected at f_{op},

$$\frac{1}{f_{om}} = \frac{1}{f_{op}} + \frac{1}{s_{im}} \tag{2-7}$$

We want to determine s_{im}, the point where the marginal rays come to a focus, so that we can use this as an object point for marginal ray input to the second lens. Combining equations 2-6 and 2-7 to eliminate f_{om} and rearranging terms yields

$$\frac{1}{s_{im}} = \frac{1}{f_{op} - \Delta_l} - \frac{1}{f_{op}}$$

which gives the result

$$s_{im} = \frac{f_{op}^2}{\Delta_1} - f_{op} \qquad (2\text{-}8)$$

Another effect to consider is that the marginal rays no longer are at the distance y off-axis when they reach the second lens. The slope of the marginal ray leaving the first lens is $-y/s_{im}$. After traveling a distance L, it has moved closer to the axis by a distance Ly/s_{im}. Its distance from the axis is then $y(1 - L/s_{im})$. Since Long. SA varies as y^2, the Long. SA of the second lens is effectively reduced by a factor of $(1 - L/s_{im})^2$. Note that when we have the final result and wish to convert to Lat. SA, the reduced aperture of the second lens will again have to be taken into account.

Let Δ_2 be the Long. SA of the second lens, with an aperture y. It is now necessary to append another subscript to the parameters to distinguish between the first and second lens. As shown in Figure 2-11, the collimated paraxial beam focuses at f_{ip2}. The marginal rays, if collimated, would have focused at $f_{ip2} - \Delta_2 = f_{im2}$. The actual marginal rays come from a virtual object at s_{im1}, given above in equation 2-8. We can therefore apply the Gaussian formula, remembering that for the actual marginal rays Δ_2 is reduced by a factor of $(1 - L/s_{im1})^2 \equiv \eta^2$.

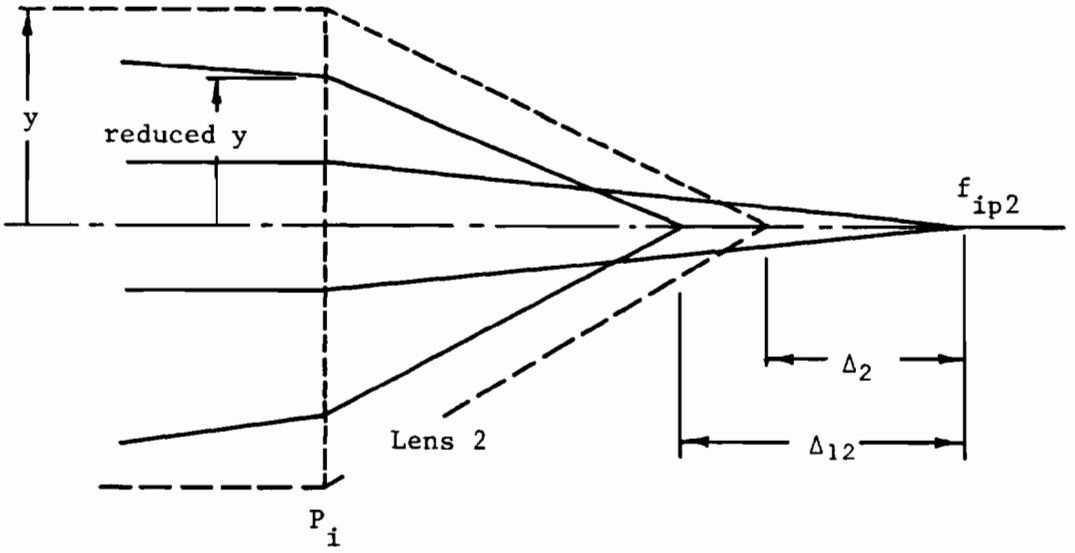

Figure 2-11. Relaying spherical aberration (Case 1) (Lens 2 only)

$$s_{om2} = -s_{im1} + L \tag{2-9}$$

$$\frac{1}{f_{im2}^*} = \frac{1}{f_{ip2} - \Delta_2 \eta^2} = \frac{1}{s_{om2}} + \frac{1}{s_{im2}} \tag{2-10}$$

In the latter equation f_{im2}^* is the effective marginal image focal point, including the effect of the reduced second lens aperture. The reduction factor is η. The marginal rays are focused by the second lens to a distance s_{im2} where

$$\frac{1}{s_{im2}} = \frac{1}{f_{ip2} - \Delta_2 \eta^2} - \frac{1}{-s_{im1} + L} . \tag{2-11}$$

Using equation 2-8 to rewrite s_{im1} and η in terms of f_{op1} and Δ_1, the above equation becomes

$$\frac{1}{s_{im2}} = \frac{f_{op1} - f_{op1}^2/\Delta_1 + L - f_{ip2} + \Delta_2 \eta^2}{\left(f_{ip2} - \Delta_2 \eta^2\right)\left(f_{op1} - f_{op1}^2/\Delta_1 + L\right)} \quad . \tag{2-12}$$

Finally, the overall Long. SA, denoted by Δ_{12}, is given by

$$\Delta_{12} = f_{ip2} - s_{im2} = f_{ip2} - \frac{\left(f_{ip2} - \Delta_2 \eta^2\right)\left(f_{op} - f_{op}^2/\Delta_1 + L\right)}{f_{op1} - f_{op1}^2/\Delta_1 + L - f_{ip2} + \Delta_2 \eta^2} \quad . \tag{2-13}$$

To convert this to Lat. SA we note that the aperture y is reduced by η.

$$\text{Lat. } SA_{12} = \left(\eta y / f_{ip2}\right) \text{ Long. SA}$$

$$= \eta y - \frac{\left(\eta y - \eta y^3 \Delta_2 / f_{ip2}\right)\left(f_{op} - f_{op}^2/\Delta_1 + L\right)}{f_{op1} - f_{op1}^2/\Delta_1 + L - f_{ip2} + \Delta_2 \eta^2} \quad . \tag{2-14}$$

To get the entire equation back in terms of Lat. SA, use the following definitions:

$$\Delta_1 = \text{Long. } SA_1 = \frac{f_{op1}}{y} \text{ Lat. } SA_1 \tag{2-15}$$

$$\Delta_2 = \text{Long. } SA_2 = \frac{f_{ip2}}{\eta y} \text{ Lat. } SA_2 \tag{2-16}$$

to rewrite equation 2-14 as

$$\text{Lat. } SA_{12} = y - \frac{\left(\eta y - \eta^2 \text{ Lat. } SA_2\right)\left(f_{op1} - y f_{op1}/\text{Lat. } SA_1 + L\right)}{f_{op1} - f_{op1} y/\text{Lat. } SA_1 + L - f_{ip2} + \left(\eta f_{ip2}/y\right) \text{Lat. } SA_2} \tag{2-17}$$

Now let's investigate a slightly different condition, shown in Figure 2-12. The point source has been moved to the right so that now the marginal rays are collimated and the paraxial rays diverge slightly.

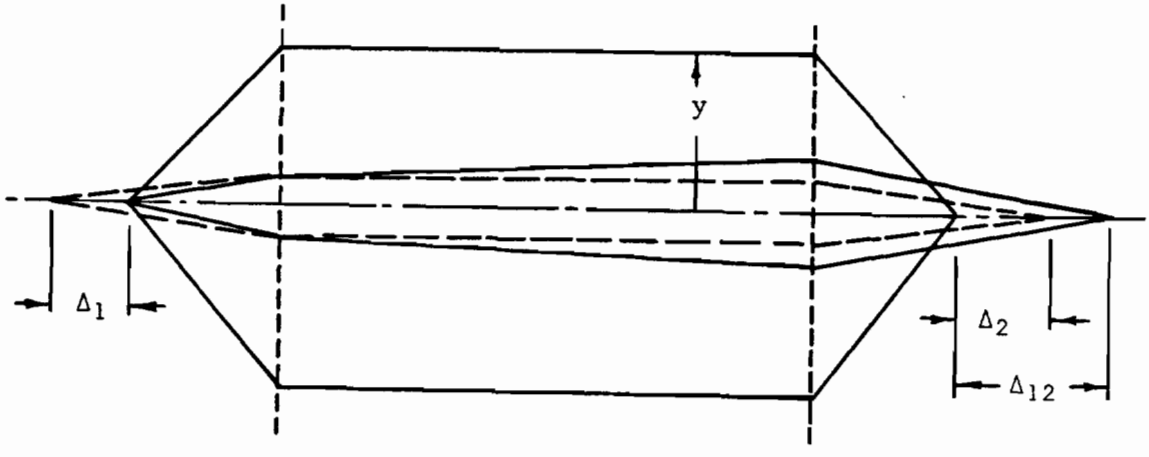

Figure 2-12. Relaying spherical aberration (Case 2).

For the diverging paraxial rays (solid lines) we have

$$\frac{1}{f_{op1}} = \frac{1}{f_{om1}} + \frac{1}{s_{ip1}} = \frac{1}{f_{op1} - 1} + \frac{1}{s_{ip1}} \quad . \tag{2-18}$$

Solving for s_{ip1},

$$s_{ip1} = \frac{f_{op1}^2}{\Delta_1} - f_{op1} \quad . \tag{2-19}$$

Unlike the previous case, where the marginal rays extended only to ny and no further, here the paraxial beam spreads out and the energy density decreases but there is no "edge" to the paraxial beam. The energy density at the second lens has a dip in the center (on axis) and so the focused image contains a reduced intensity contribution from the paraxial cone of rays which causes the image to appear as an annular ring. The outer edge of the annular ring still determines the blur diameter, even though the central intensity is reduced. In this case, then, we can neglect the effect on spherical aberration of the diverging paraxial beam. The image formed by the first lens (at s_{ip1} for paraxial rays; at ∞ for marginal rays) becomes the object for the second lens.

$$s_{op2} = L - s_{ip1} \; ; \quad s_{om2} = \infty \tag{2-20}$$

We now apply the Gaussian formula to the second lens:

$$\frac{1}{f_{ip2}} = \frac{1}{s_{op2}} + \frac{1}{s_{ip2}} = \frac{1}{L - s_{ip1}} + \frac{1}{s_{ip2}}$$

$$s_{ip2} = \frac{(f_{ip2})(L - s_{ip1})}{L - s_{ip1} - f_{ip2}} \qquad (2\text{-}21)$$

Since the incoming marginal beam is collimated, the marginal rays are focused at $f_{im2} = f_{ip2} - \Delta_2$. The final Long. SA is

$$\Delta_{12} = s_{ip2} - f_{im2} = \frac{f_{ip2}\left(L - f_{op1}^2/\Delta_1 + f_{op1}\right)}{L - f_{op1}^2/\Delta_1 + f_{op1} - f_{ip2}} - f_{ip2} + \Delta_2 \qquad (2\text{-}22)$$

using equation 2-19 to obtain s_{ip1} in terms of f_{op1} and Δ_1.

As before, we can convert this equation into terms involving Lat. SA. The result is:

$$\text{Lat. } SA_{12} = \frac{f_{ip2}\left(L - \dfrac{yf_{op1}}{\text{Lat. } SA_1} + f_{op1}\right)}{L - \dfrac{yf_{op1}}{\text{Lat. } SA_1} + f_{op1} - f_{ip2}} - f_{ip2} + \frac{f_{ip2}}{y}\,\text{Lat. } SA_2 \qquad (2\text{-}23)$$

To summarize the results of this section, we can rewrite the expressions for Lat. SA, dropping extra subscripts since in the final equations f_1 and f_2 can be used for f_{op1} and f_{ip2} with no ambiguity. We can also introduce the aperture half angles $\alpha_1 = \frac{y}{f_1}$, $\alpha_2 = \frac{y}{f_2}$, and $\alpha_L = \frac{y}{L} = \frac{\alpha_1 f_1}{L}$. As previously stated,

$$\eta \equiv (1 - L/s_{iml}). \tag{2-24}$$

Using equation 2-8 for s_{iml} and equation 2-15 for Δ_1,

$$\eta = 1 - \frac{L}{f_1\left(\frac{\alpha_1 f_1}{\text{Lat. SA}_1} - 1\right)} \quad . \tag{2-25}$$

For the first case (diverging marginal beam) the result is:

$$\text{Lat. SA}_{12} = \eta\left[f_2\alpha_2 - \frac{\left(1 - \frac{\eta\ \text{Lat. SA}_2}{\alpha_L}\right)\left(\frac{1}{\alpha_1} \quad \frac{f_1}{\text{Lat. SA}_1} \quad \frac{1}{\alpha_L}\right)}{\frac{1}{\alpha_1} - \frac{f_1}{\text{Lat. SA}_1} + \frac{1}{\alpha_L} - \frac{1}{\alpha_2} + \frac{\eta\ \text{Lat. SA}_2}{\alpha_2}}\right] \tag{2-26}$$

For the second case (collimated marginal beam),

$$\text{Lat. SA}_{12} = \frac{1}{\alpha_2}\left(\frac{f_2}{\frac{1}{\alpha_L} - \frac{f_2}{\text{Lat. SA}_1} + \frac{1}{\alpha_1} - \frac{1}{\alpha_2}} + \text{Lat. SA}_2\right) \quad . \tag{2-27}$$

F. Magnetic Lenses

Consider a system with cylindrical symmetry and a region of that system containing a rotationally symmetric magnetic field ($B_\theta = 0$). If an electron is injected into the region and is traveling with a velocity $(0,0,v_z)$, then the radial component of the field acts on the moving electron with a force which creates a θ component in the velocity, v_θ. Then v_θ interacts with B_z resulting in an inward radial force. The momentum of the electron is thus redirected by the magnetic field into angular and radial components which, for a collimated beam of electrons, produces a focused spot.

We now look at the process quantitatively.[9] The magnetic scalar potential ψ, for which

$$\overline{B} = -\mu\overline{\nabla}\psi \ , \tag{2-28}$$

can be expanded for a rotationally symmetric field as

$$\psi(r,z) = \psi(z) - \frac{r^2}{4}\psi''(z) + \frac{r^4}{64}\psi''''(z) \quad . \ . \ . \tag{2-29}$$

This expansion follows from the fact that ψ obeys Laplace's equation. Using this and equation 2-28 above, we can obtain expansions for the magnetic field at an off-axis point in terms of the axial field and its derivatives.

$$B_z(r,z) = B(z) - \frac{r^2}{4}B''(z) + \frac{r^4}{64}B''''(z) \ . \ . \ . \tag{2-30}$$

$$B_r(r,z) = -\frac{r}{2}B'(z) + \frac{r^3}{16}B'''(z) \quad . \ . \ . \tag{2-31}$$

If we consider only paraxial electrons we can approximate the field by the first terms of the expansions.

$$B_z(r,z) \cong B(z) \tag{2-32}$$

$$B_r(r,z) = -\frac{r}{2} B'(z) \tag{2-33}$$

The dynamics of electron motion in a magnetic field containing no θ component are as follows:

1) inward force = Lorentz force + centrifugal "force"

$$m \ddot{r} = -e B_z r \dot{\theta} + m r \dot{\theta}^2 \tag{2-34}$$

2) $\frac{d}{dt}$ (angular momentum) = moment of Lorentz force

$$\frac{d}{dt} (m r^2 \dot{\theta}) = r(e \dot{r} B_z - e B_r \dot{z}) \tag{2-35}$$

3) axial force = Lorentz force

$$m \ddot{z} = e B_r r \dot{\theta} \tag{2-36}$$

If we substitute equation 2-33 into 2-35, we obtain

$$\frac{d}{dt} (m r^2 \dot{\theta}) = e B_z r \dot{r} + e \frac{r^2}{2} \frac{\partial B_z}{\partial z} \dot{z} = \frac{d}{dt}\left(\frac{e}{2} r^2 B_z\right)$$

Integration with respect to time yields

$$m r^2 \dot{\theta} = \frac{e}{2} r^2 B_z + C \ . \tag{2-37}$$

If $\dot{\theta} = 0$ where $B_z = 0$ outside the lens, then $C = 0$. Therefore,

$$\dot{\theta} = \frac{e}{2m} B_z \tag{2-38}$$

indicating that the angular velocity of a paraxial beam is only dependent on the axial component of the magnetic field.

If we substitute equation 2-38 for $\dot{\theta}$ and equation 2-33 for B_r in equation 2-36, we have

$$\begin{aligned} \ddot{z} &= - \left(\frac{e}{2m}\right)^2 r^2 B_z \, \partial B_z/\partial z \\ &= - \left(\frac{e}{2m}\right)^2 \frac{r^2}{2} \frac{\partial B_z^2}{\partial z} \end{aligned} \tag{2-39}$$

This expression is of a higher order than first, so we can neglect it and say that the axial velocity of the paraxial beam is constant.

The radial equation 2-34, with equation 2-38 substituted for $\dot{\theta}$, becomes

$$\ddot{r} = -(e^2/4m^2) B_z^2 r \tag{2-40}$$

The inward radial force is proportional to the radius and its direction is independent of the polarity of the magnetic field. If the time variable is eliminated from this equation, it becomes the trajectory equation:

$$\frac{d^2r}{dz^2} = -(e/8mV) B_z^2 r \, . \tag{2-41}$$

Here V is the accelerating potential for the electrons. Let prime stand for differentiation with respect to z. Then, if we integrate this equation with respect to z, we get the difference between the slopes of the incoming (object) and outgoing (image) rays of an electron beam.

$$r_i' - r_o' = -(e/8mV) \int_{-\infty}^{\infty} r\, B_z^2\, dz \qquad (2\text{-}42)$$

If the incoming beam is collimated $r_o' = 0$. If the lens is a "thin lens," then the ray direction of the lens is changed with no appreciable change in r, the off-axis ray distance. Then the above equation reduces to

$$\frac{r_i'}{r_o} = -\frac{e}{8mV} \int_{-\infty}^{\infty} B_z^2\, dz = \frac{1}{f_i} . \qquad (2\text{-}43)$$

This formula for the focal length of a weak magnetic lens was first derived in 1926 by Busch.[10]

Most practical lenses of interest for electron microscope applications do not admit an analytical solution for their cardinal points. In particular, the lenses used in the SAM have such a large bore/gap ratio that there seems to be no approximation for the axial magnetic field that is valid.[11]

A finite element method computer program by Munro[12] was used to generate values for the cardinal point coordinates for the two Celco

magnetic lenses. This program also generates values for C_s and C_c, the spherical and chromatic aberration coefficients.

Briefly, the Munro program solves Laplace's equation for the magnetic scalar or vector potential, depending on whether just the pole pieces or the entire lens structure plus coil winding is specified. The axial magnetic field is then calculated from the potential.

A paraxial electron trajectory is then run using the paraxial ray equation with the electron leaving the object point on axis with unity slope, $r'(z_o) = 1$, if the aberrations are to be referred to the object side or with the electron approaching the image point with negative unity slope, $r'(z_i) = -1$, if the aberrations are to be referred to the image side. Using the appropriate r(z) solution, the aberration integrals are then computed.

The spherical aberration coefficient (C_s) computed by Munro's program gives the lateral spherical aberration

$$\text{Lat. SA} = C_s\alpha^3$$

where α is the aperture half-angle, y/f_o or y/f_i.

The minimum blur diameter is given by

$$(B_{SA})_{\text{min.}} = 1/2 \text{ Lat. SA} = 1/2\ C_s\alpha^3.$$

The longitudinal chromatic aberration coefficient (C_c) gives the difference in axial intercept produced by an increment in voltage dV by

$$\text{Long SA} = C_c \frac{dV}{V} \quad .$$

The longitudinal chromatic aberration can be converted to lateral chromatic aberration by the geometric considerations shown in Figure 2-13.

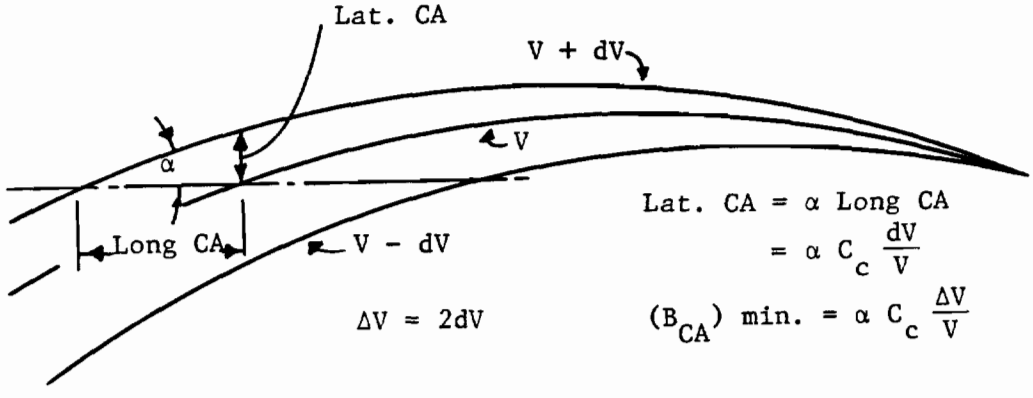

Figure 2-13. Conversion of Long. CA to Lat. CA.

G. Quadrupole Lenses--Stigmator

An electrostatic or magnetic quadrupole produces a line focus. An electron beam traveling in the z direction is converged in one plane, say the x,z plane and is diverged in the orthogonal plane, the y,z plane (see Figure 2-14).

A magnetic quadrupole is produced by four hyperbolic-faced pole pieces arranged as shown in Figure 2-15. Fortunately, almost any shape of the four pole pieces will produce hyperbolic

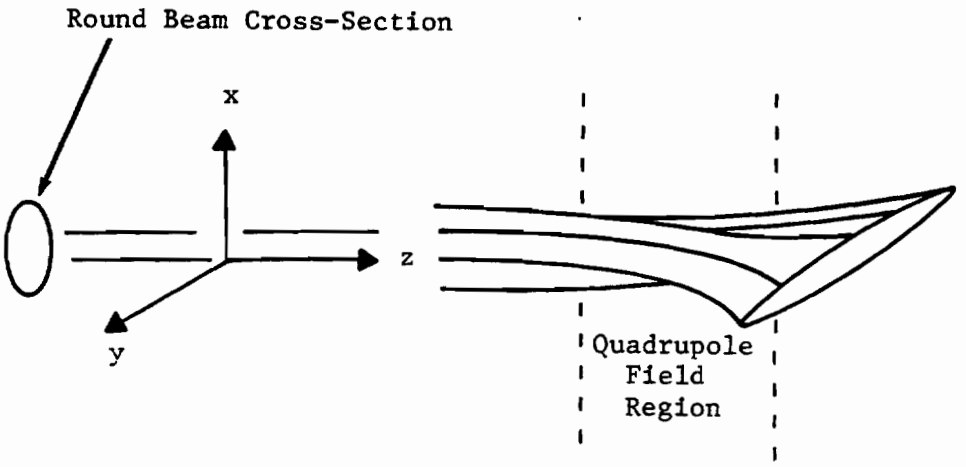

Figure 2-14. Quadrupole field effect on electron beam.

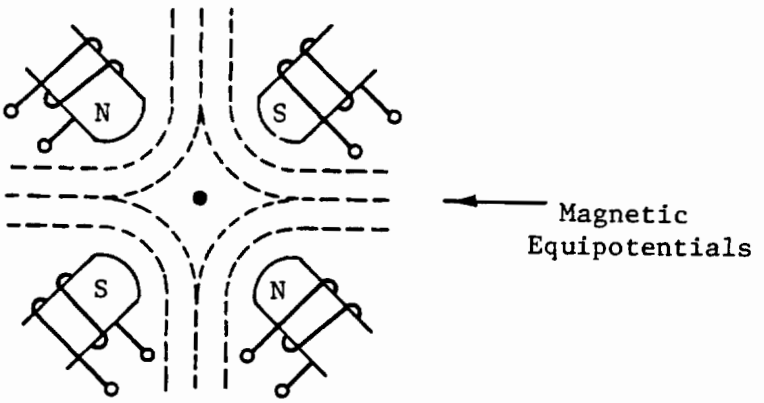

Figure 2-15. Magnetic quadrupole.

equipotentials in the vicinity of the z axis;[13] even air core coils will be satisfactory for applications in which an intense field is not required.

Besides the line focusing property, the quadrupole lens possesses another property distinct from those of the axially symmetric lens, namely that of strong focusing. In the axially symmetric lens, the electron beam moving along the z axis encounters only magnetic field lines which are approximately parallel to its motion. In the quadrupole lens the field lines are perpendicular to the z axis and so a given field strength has a larger focusing effect on an electron beam in a quadrupole lens. Two quadrupole lenses can be used in series to achieve a point focus by rotating the second lens by $\pi/2$ about the z axis so the diverging and converging properties add to yield a net convergence in both the x,z and y,z planes.

The use of the quadrupole lens in the SAM system is not for focusing but rather for astigmatism correction. The off-axis astigmatism, analogous to the Seidel aberration, and the astigmatism due to mechanical imperfections of the magnetic lens combine to produce an eliptically shaped spot, i.e., orthogonal axes have different focal points. The introduction of a weak quadrupole lens which can be varied in magnitude and rotated about the beam axis (z axis) can eliminate the astigmatism by introducing a converging-diverging field which exactly cancels the lens astigmatism. This quadrupole lens is called a stigmator.

Two points about this device require some discussion. First, lenses and other mechanical parts of the system are not necessarily restricted to rotational asymmetries of second order (elliptical). If, after correction of the second order asymmetry by a quadrupole, the spot shows a third order asymmetry then an additional stigmator of hexapole geometry can be used to correct this asymmetry.[4,14]

The second point is that placement of the stigmator in the optical column can be important if one is trying to image an extended object. If the stigmator introduces a correcting asymmetry to the beam at some distance from the lens which produces the astigmatism, the correction will be correct at only one point in the field of view. Placing the stigmator within the lens gap to correct the problem "at its source" produces a larger stigmatic field.[15]

H. Deflection

An electron of velocity u_o, upon encountering a magnetic field B transverse to its motion, will be deflected into a circle of radius

$$r_e = \frac{m\ u_o}{e\ B}$$

in the plane containing the vectors u_o and B. If the field extends only over a small portion of the electron's path, the electron will be deflected from its path by an angle ϕ where

$$\tan \phi = \frac{z}{r_e} = \frac{e\ B\ z}{m\ u_o}$$

and z is the extent of the magnetic field along the initial direction of motion.[16] The electron leaves the deflection field region with a redirected velocity vector of the same magnitude with which it entered. The effective deflection "principal plane" is at the center of the deflecting field.

In looking at the electrostatic deflection case, it may be thought that a transverse E field imparts a transverse velocity to the beam, which, when summed with the initial velocity results in not only a redirected but also increased magnitude velocity vector. Actually, electrostatic deflection produces the same overall result as magnetic deflection because of the fringing fields around the deflection plates which reduce the longitudinal velocity vector in such a proportion as to leave the magnitude of the velocity unchanged.[17] This is an inherent characteristic of the electric field and not due to a specific deflecting electrode geometry.

Magnetic deflection with the coils outside the vacuum barrier permits a greater flexibility in positioning the coils and modifying their design than would be allowed using either magnetic or electrostatic deflection inside the vacuum system. Additionally, magnetic deflection systems, like magnetic lenses, are less aberrating than electrostatic systems. For the SAM system, since as the magnification increases the field size decreases, deflection aberrations are not a problem. If one were to require that the field of view at high magnification be shifted electrically rather than mechanically

then more attention would have to be given to deflection coil design and placement.

Munro[1] has done a comparative study of various magnetic deflection system configurations using a computer program to calculate the overall properties of a combination of lenses and deflecting yokes. He states that conventional post-lens single deflection systems can have better properties than conventional pre-lens double deflection systems. His study is primarily concerned with the extreme requirements of e-beam lithography. In the SAM, the requirements to maintain a 0.1 μm spot over a 10 × 10 μm field can be adequately met by a simple saddle coil yoke.

The saddle coils produce a field at an axial point z given by the Biot-Savart formula as

$$B_x(z) = \frac{N\ I\ \mu_o\ \sin\theta}{\pi}\left[\frac{H(H^2 + 2R^2)}{R(H^2 + R^2)^{3/2}} - \frac{h(h^2 + 2R^2)}{R(h^2 + R^2)^{3/2}}\right]$$

where the variables are defined by Figure 2-16.

There is an optimum geometry which produces a uniform field for these coils.[18] A coil set with a length to diameter ratio of 2 and arcs of 120° will have no second order central field derivatives in any direction. The length to diameter ratio of the coils in the SAM is approximately 0.6 due to physical limitations.

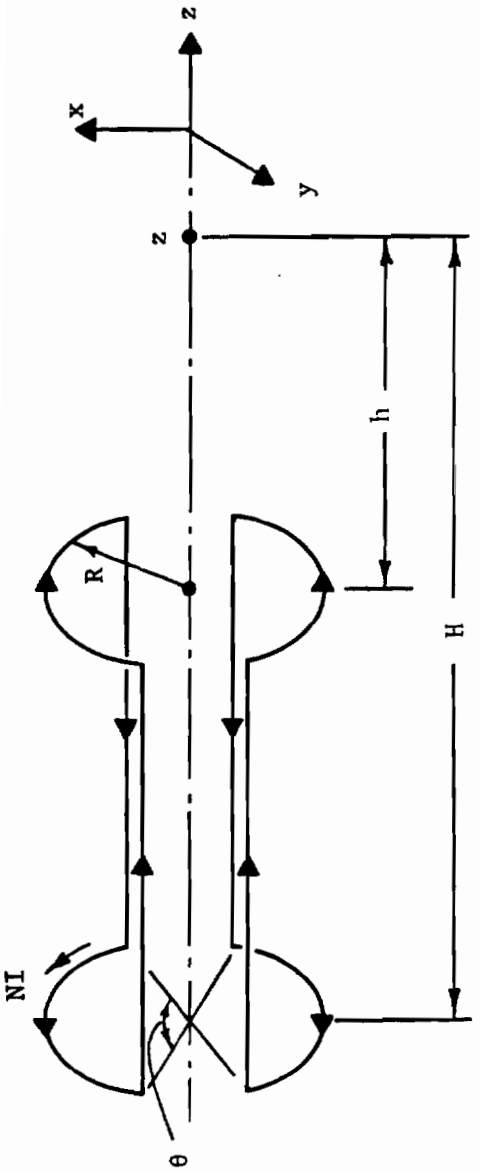

Figure 2-16. Saddle deflection coils.

REFERENCES

1. E. Munro, J. Vac. Sci. Technol. 12, 1146 (1975).
2. R. L. Siddon, The Physics Teacher, Dec., 647 (1978).
3. F. A. Jenkins and H. E. White, "Fundamentals of Optics," (McGray-Hill, 1957), 130.
4. F. Lenz, Proc. Intl. Conf. El. Microscopy, London, 83 (1954).
5. M. Born and E. Wolf, "Principles of Optics," (Macmillan, 1959), 206.
6. L. Seidel, Astr. Nachr. 43, No. 1027, 289; No. 1028, 305; No. 1029, 321 (1956).
7. W. J. Smith, "Modern Optical Engineering," (McGraw-Hill, 53), 1966.
8. W. J. Smith, op. cit. 63.
9. A. B. El-Kareh and J. C. J. El-Kareh, "Electron Beams, Lenses and Optics," (Academic Press, 1970), 248-254.
10. H. Busch, Arch. Electrotechn. 18, 583 (1927).
11. T. Mulvey and M. J. Wallington, Rep. Prog. Phys. 36, 379-381 (1973).
12. E. Munro, "A Set of Computer Programs for Calculating the Properties of Electron Lenses," Engineering Dept., Univ. of Cambridge (1975).
13. P. Grivet, "Electron Optics," (Pergamon Press, 1972), 293.
14. W. D. Riecke, Optik 19, 81 (1962).

15. F. Lenz, Optik 15, 393 (1958).

16. O. Klemperer, "Electron Physics," (Butterworths, 1972), 15.

17. C. A. Coombes, Am. J. Phys. 47, 555 (1979).

18. D. M. Ginsberg and M. J. Melchner, Rev. Sci. Instrum. 41, 122 (1970).

CHAPTER 3

ELECTRON SOURCE

A. Introduction

This review deals with the theory of thermionic, field and thermal field emission. The latter describes the electron source for the scanning Auger microscope (SAM). The characteristics of this source which are of importance in an electron beam microprobe are then examined in more detail, namely the brightness, the effective Gaussian source size and the energy spread of the emitted electrons. The measured characteristics of the Zr/W thermal field emitter used in this microprobe system are given in the results section of this paper, including noise measurement.

B. Thermionic Emission

Thermionic emission results when electrons in a metal achieve sufficient momentum normal to the metal surface to overcome the metal-vacuum potential barrier. The electrons can be assumed to be a gas of particles, each with an internal degeneracy of two, thus being subject to Fermi-Dirac statistics.[1]

At T = 0, the kinetic energy of the electrons of highest energy is μ_o. Now, if we raise the temperature of the metal, the Fermi distribution function develops a "tail" with a finite number of electrons

which have energies greater than μ_o (see Figure 3-1).

$$N(\epsilon) = \frac{3N}{2\mu_o^{3/2}} \frac{\epsilon^{1/2}}{e^{(\epsilon - \mu)/kT} + 1} \qquad (3\text{-}1)$$

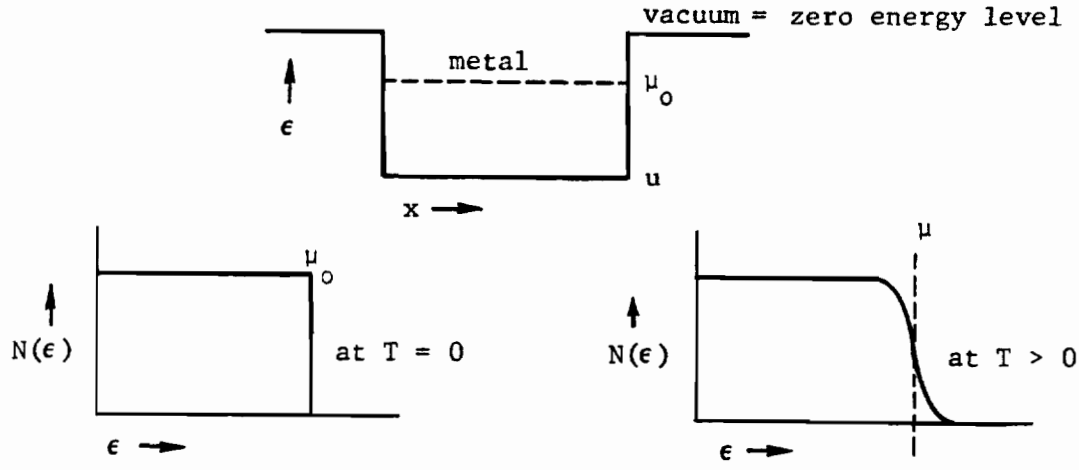

Figure 3-1. Fermi-Dirac statistics.

In Figure 3-1, μ_o = chemical potential at T = 0; μ = chemical potential at the temperature T; u = energy at bottom of conduction band; ϵ = energy/electron. These higher energy electrons tend to leak into the vacuum, reducing the number of electrons in the metal reservoir.

Assuming the reflection coefficient at the surface of the metal is zero allows us to make a connection between the number of electrons hitting the surface and the thermionic emission current density. Then, if we neglect the change in potential outside the metal caused by the space charge of electrons and note that the concentration of

electrons in the vacuum is in equilibrium with the concentration in the metal, then we can set the chemical potentials equal:

$$-\phi = \mu - u$$

where ϕ is known as the work function of the metal.

Multiplying through by N_o (Avogadro's number) we obtain

$$-W = G - U = -N_o\phi$$

or

$$W = U - G$$

(free energy/mole) = total internal energy - Gibbs free energy. The work function is so much greater than the mean energy produced thermally ($\phi/kT \gg 1$) that we can neglect the unity term in the sum in the denominator of the distribution function, equation 3-1, which reduces the problem to classical statistics. Then, the chemical potential $-\phi$ of a gas in terms of its pressure P is

$$-\phi = \frac{G}{N_o} = kT \ln \left[\left(\frac{h^2}{2\pi\, mkT} \right)^{3/2} \frac{1}{Q_i} \frac{P}{kT} \right] \qquad (3\text{-}2)$$

where Q_i = the factor in the partition function due to internal degrees of freedom = 2, the degeneracy of the electron gas.

Solving this for P yields

$$P = 2kT \left(\frac{2\pi\, mkT}{h^2} \right)^{3/2} e^{-\phi/kT} \qquad (3\text{-}3)$$

This gives the vapor pressure of the external gas of electrons in terms of the work function.

From the pressure, one can determine the number of gas particles which strike a unit surface per unit time and thereby determine the current density

$$J = \frac{4\ em\ (kT)}{h}\ e^{-\phi/kT} \tag{3-4}$$

The quantum mechanical reflection and coefficient at the potential barrier is a function of the size and shape of the potential step, which is fixed and the normal kinetic energy of the electrons, which is at or above the vacuum level. Since the Fermi distribution function falls off rapidly with energy past μ_o, the major contribution of emitted electrons comes from those electrons exactly at the vacuum level, from which we can assume the reflection coefficient is constant and incorporate its effect on the emitter current by the factor (1 - r). Denoting the work function by ϕ and evaluating the pre-exponential factor yields

$$J = 120.1\ (1 - r)\ T^2\ e^{-\phi/kT}\ \ A/cm^2. \tag{3-5}$$

This is known as the Richardson equation.

The work function is not temperature independent, however. We have indicated that

$$\phi = u - \mu\ .$$

The expansion of the lattice with temperature tends to increase u, but the vibrational and thermal effects on the lattice tend to decrease it. μ is also affected in the same way. These effects amount to typically a 10^{-3} to 10^{-4} eV/K correction to ϕ.

In cases of low fields and high temperatures, the thermionic current is primarily temperature dependent and is described by the Richardson equation. If the field is increased to the point where the top of the potential barrier is lowered, but not to the point where appreciable tunneling can occur, the process is described as Schottky[2] emission (See Figure 3-2). The Richardson equation is then modified by an applied field factor,

$$J = 120.1\ T^2\ e^{-\phi/kT}\ e^{\ cF^{1/2}/kT}$$

where $c = \left(\frac{e^3}{4\pi\epsilon_o}\right)^{1/2}$.

Typical current densities produced by a tungsten thermionic emitter are on the order of 1 to 10 A/cm^2.

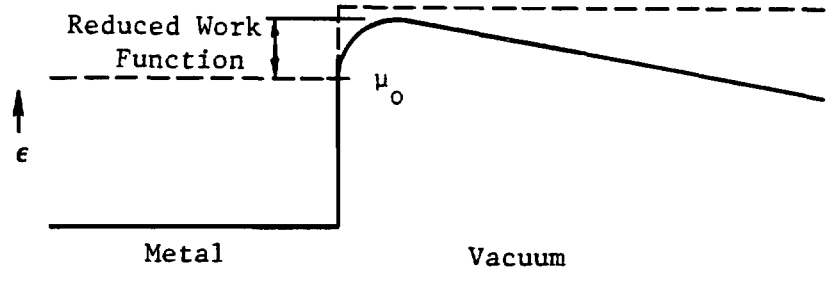

Figure 3-2. Schottky potential barrier lowering.

C. Field Emission

Field emission of electrons from a metal surface occurs when the external applied electric field deforms the potential barrier to such an extent that electrons can tunnel through the deformed barrier. Figure 3-3 indicates the barrier deformation.

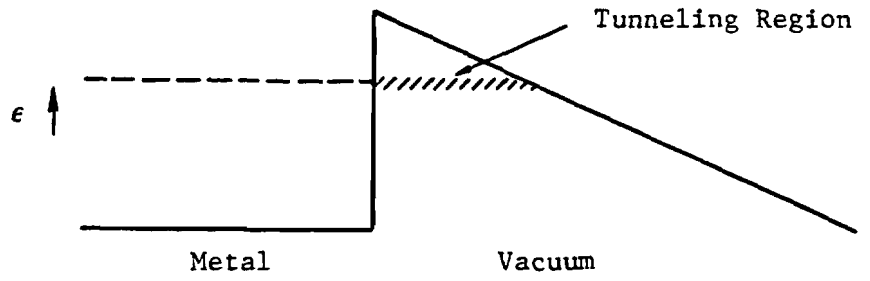

Figure 3-3. Basic field emission.

With a typical applied field of 0.3 V/Å and a work function ϕ of 4.5 eV (clean tungsten), the tunneling distance is approximately 15 Å.

In 1928, R. H. Fowler and L. Nordheim published a paper entitled Electron Emission in Intense Electric Fields[3] which set forth the now well-known Fowler-Nordheim equation relating the field emission current to the applied field and work function of the emitter. They considered field emission as a one-dimensional tunneling problem at T = 0°K. They calculated the WKB transmission coefficient through the potential barrier for electrons of kinetic energy W

(energy normal to the emitter surface). It was found to be approximately

$$D(W) = \frac{4[W(C - W)]^{1/2}}{C} \; e^{-4k(C - W)^{3/2}/3F} \qquad (3\text{-}6)$$

where C = height of the potential barrier, F = electric field applied, and $k^2 = 8\pi^2 m/h^2$, a constant.

The number of electrons N(W) incident on a surface of unit area per unit time with a normal kinetic energy W, evaluated according to Sommerfeld's theory, was shown to be

$$N(W) = \frac{4\pi mkT}{h^3} \; L \; \frac{W - \mu}{kT}$$

where

$$L(\beta) = \int_0^\infty \frac{dy}{e^{\beta + Y} + 1} ; \quad \mu = \text{Fermi level energy.}$$

Combining D(W) and N(W) to get the field emitted current density for all energies W,

$$J = \frac{4\pi mekT}{h^3} \int_0^\infty D(W) \; L \left(\frac{W - \mu}{kT}\right) dW$$

where e = electron charge. For low temperature, we can replace L(β) by β when β is negative and by zero otherwise. Since $\beta = \frac{W - \mu}{kT}$, when $W > \mu$ the integral L(β) is zero. Using the equation 3-6 for D(W) and integrating,

$$J = \frac{16\pi me}{Ch^3} \int_0^{\mu} W^{1/2} (C - W)^{1/2} (\mu - W) e^{-4k(C - W)^{3/2}/3F} dW.$$

Then, evaluating k, letting $\phi = C - \mu$ = the work function, and noting that for large W ($\simeq \mu$) the exponential term allows the integral to be approximated, we obtain

$$J = \frac{e}{2h} \frac{\mu^{1/2}}{(\phi + \mu)\ \phi^{1/2}} F^2\ e^{-4k\phi^{3/2}/3F}$$

Evaluating the constants,

$$J = 6.2 \cdot 10^{-6} \frac{\mu^{1/2}}{(\phi + \mu)\ \phi^{1/2}} F^2\ e^{-6.8 \cdot 10^7\ \phi^{3/2}/F} \qquad (3\text{-}7)$$

where J is in A/cm^2, μ and ϕ are in eV, and F is in V/cm. This is known as the Fowler-Nordheim equation.

In cases of high fields and low temperature, the Fowler-Nordheim equation describes the current vs. field relationship. A Fowler-Nordheim plot of log J/F^2 vs. 1/F will have a slope proportional to $\phi^{3/2}$. Therefore, work functions can be measured experimentally from the I-V data, if the relationship between I and J (the emitting area) and between V and F (the field factor β) is known, or conversely these parameters can be determined if the work function is known.

For typical fields in the range of .3 to .6 V/Å, the current densities range from 10^2 to 10^4 A/cm^2.

An image charge treatment of the potential at the surface yields the result as shown in Figure 3-4:

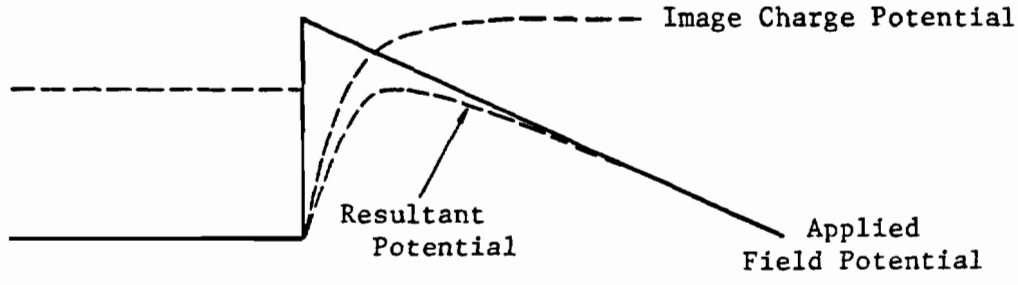

Figure 3-4. Image charge effect.

The potential is decreased by the image term as follows:

$$V = -Fex - e^2/4x.$$

The image term can be incorporated into the Fowler-Nordheim equation as a correction factor to the exponent, $\alpha(y) = (1 - y)^{1/2}$ where

$$y = 3.8 \cdot 10^{-4} F^{1/2}/\phi .$$

Gomer[4] summarizes the results of various ways of including the image corrected potential. Under most conditions encountered in practice, y is 0.2 to 0.35, so that a reduction in the applied field of the order of 10 to 20 percent results from the image effect.

D. Thermal-Field Emission

Thermal-field emission occurs in the ranges of temperature and applied field which are intermediate between thermionic emission and field emission.

Murphy and Good[5] have given a unified treatment of the emission of electrons which is valid for the thermionic, field, and the intermediate transition region as well. They form expressions for the transmission coefficient through the potential barrier, D(F,W) and for the number of electrons per second per unit area incident on the barrier, N(T,ϕ,W) and integrate the product to find the emission current density:

$$J(F,T,\phi) = e \int_{-W_a}^{\infty} D(F,W)\ N(T,\phi,W)\ dW$$

where W_a is the energy at the bottom of the Sommerfeld well in the metal. The following potential energy diagram illustrates the relevant energy and position parameters (Figure 3-5).

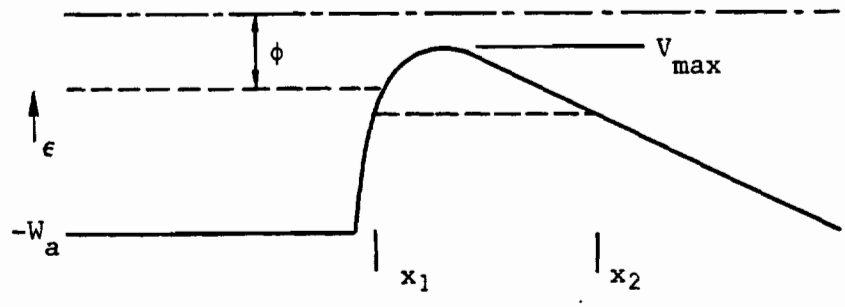

Figure 3-5. Field emission tunneling diagram.

The transmission coefficient is taken to be unity for $W > V_{max}$. For $W < V_{max}$, it is evaluated by a parabolic WKB-type approximation which depends on the shape of the potential curve between the points x_1 and x_2 for a given W.

The integral for $J(F,T,\phi)$ can be evaluated analytically by making appropriate approximations for various ranges of F and T. The integral reduces to the Richardson-Schottky equation for the thermionic region and to the Fowler-Nordheim equation in the field emission region. The intermediate or transition region current density is given by

$$J = \frac{F}{2\pi}\left(\frac{kTt}{2\pi}\right)^{1/2} \exp\left(-\frac{\phi}{kT} + \frac{F^2\,\Theta}{24(kT)^3}\right)$$

where $\Theta = 3t^{-2} - 2vt^{-3}$ and v and t are slowly varying functions of F and T.

Using the expressions from Murphy and Good and integrating numerically rather than using analytic approximations with limited regions of validity, El-Kareh, Wolfe and Wolfe[6] have generated graphs of J vs. F for various temperatures and work functions and also normal, tangential, and total energy distributions for the emitted electrons. The authors indicate that their theoretical results agree with published experimental results, at least over the range of current densities considered. The FWHM for the energy spread from the above mentioned study is predicted to be no greater than about 0.6 eV for a wide range of ϕ, F, and T. Recently,

however, Bell and Swanson[7] have measured total energy distributions at high current densities and have found an anomalously high ΔE which increases with current density J and is independent of temperature. This work was done for emitters of both low and high work function and gave the same anomalous results.

The thermal-field electron (TFE) emitter has several advantages over the thermionic cathode and the cold field emitter. Both the cold and thermal field emitters yield greater current densities than the thermionic cathode. In an electron optical system, since brightness (A/cm^2 sr) is a conserved quantity, in order to obtain a high current density in a focused spot, a high brightness cathode is necessary.

Experience with cold field emitters has discouraged their use in many applications because of noise problems, instability, short life, and extreme vacuum requirements. The TFE mode of operation allows a relaxation of vacuum requirements by rapid thermal annealing of sputter-induced surface deformation, thereby minimizing the probability of emitter destruction by a regenerative vacuum arc. Additionally, the high emitter temperature maintains a low and constant coverage of adsorbed gases on the emitter surface thereby eliminating time dependent work function change.

E. The Zr/W<100> TFE Emitter

Zirconium adsorption on tungsten has been shown to selectively lower the work function of the (100) crystal plane from 4.5 eV to

approximately 2.6 eV.[8,9] In the Fowler-Nordheim equation for field emitter current density, the dominant factor has the form $\exp(-\text{const.}\ \phi^{3/2}/F)$ where ϕ is the work function and F is the electric field at the tip. If the work function is reduced to 2.6 eV, the field required for a given current density is 44% of that required for a work function of 4.5 eV. Since the field factor $B = F/V$ is inversely proportional to the emitter radius, the radius of the low work function emitter can be increased by a factor of $(0.44)^{-1} \approx 2.3$ over that of the high work function emitter, with no reduction in current density at a given voltage. An added advantage of the selective (100) plane work function reduction is the angular confinement of the beam to a half angle of less than about 9°, which decreases "wasted" current and excessive dissipation in the electron gun.

The Zr/W <100> TFE emitter is made by the following method.[10] A tungsten wire (.005 in. dia.) is triple-pass zone refined in the <100> direction. The end of the wire is then electrochemically etched to the desired radius. A zirconium hydride ring is attached to the shank of the emitter. The emitter, attached to a tungsten hairpin filament, is placed in the electron gun. Under vacuum in the system, the emitter is heated to allow the zirconium to diffuse along the surface of the wire and out to the tip. After several hours of operation the emitter stabilizes with the low work function (100) plane at the tip producing a high angular confinement of the emitted electron beam.

Operating experience with this type of field emitter, combined with reports from others[11] has shown it to be a stable, reliable, low noise source of high brightness. As with any elevated temperature source, an increased flicker noise amplitude over that of a cold emitter is expected; however, the large emitter radius allowed by the low work function surface reduces current fluctuations to an acceptable level. Our experience has shown that the higher voltage (larger radius) emitter has two additional advantages over a lower voltage one. First, it is more rugged and resistant to the transients that destroy emitters of smaller radii. Second, it has been noticed that the larger emitter radius reduces the anomalously high beam energy spread observed at high emitter current density.[7] This advantage is substantiated by our spot size versus current data for the Zr/W <100> TFE emitter. The larger radius emitter requires, however, a higher voltage for a given angular intensity since the field factor (β) is reduced, where the field $F = \beta V$ and V is the applied voltage.

The Zr/W <100> TF emitter used in this microprobe system combines the advantages of TFE emission, a large tip radius and a lowered work function.

F. Source Parameters (Electron Optics)

The electron beam brightness, measured in A/cm^2 sr, is strictly conserved only in the limit of an infinitely small central zone of the beam in an aberration-free optical system and in regions in

which the potential is the same.[12] The aberration-free condition is approached as the solid angle of the beam decreases.

D. B. Langmuir[13,14] demonstrated that the theoretical maximum current density (j') in a focused spot was limited by the cathode current density (j), the accelerating voltage (V) and the image plane semi-angle of convergence (α). The result was

$$j' = j\left(\frac{Ve}{kT} + 1\right)\sin^2\alpha$$
$$\simeq j\left(\frac{11600\ V}{T}\right)\alpha^2 .$$

The approximation is valid when used for small convergence angles and acceleration voltages such that $Ve >> kT$, which is usually the case. The derivation of the above Langmuir limit assumed a plane cathode with a sharply bounded cathode emission region and a semi-Maxwellian electron velocity distribution.

Worster[15,16] considered the brightness of electron beams for a general velocity distribution at the cathode. He showed that for emission in the Schottky region the Langmuir law still held, even though the velocity distribution is not Maxwellian. He also demonstrated that for field emitted beams an analogous expression

$$j' \simeq j\left(\frac{eV}{d}\right)\alpha^2$$

held, where

$$d = \langle E_t \rangle$$

where $\langle E_t \rangle$ is the average tangential electron energy at the cathode.

The parameter d is approximately proportional to the applied field and is independent of temperature. In the field emission region $d > kT$, i.e. the average tangential energy of the emitted electrons is greater than it would be for Schottky emission at the same temperature.

Worster also considered off-axis brightness in a cylindrically symmetric field emission system and determined that in the vicinity of an axial cross-over in a field emission gun (see Figure 3-6), the current density varied as

$$j' \approx j\left(\frac{eV}{d}\right) \exp\left(\frac{-r^2}{M^2\ a^2}\right)$$

where r = radial distance from axis, a = cathode tip radius and M = gun magnification, defined as

$$M = (\phi/\theta)\ (d/eV)^{1/2}$$

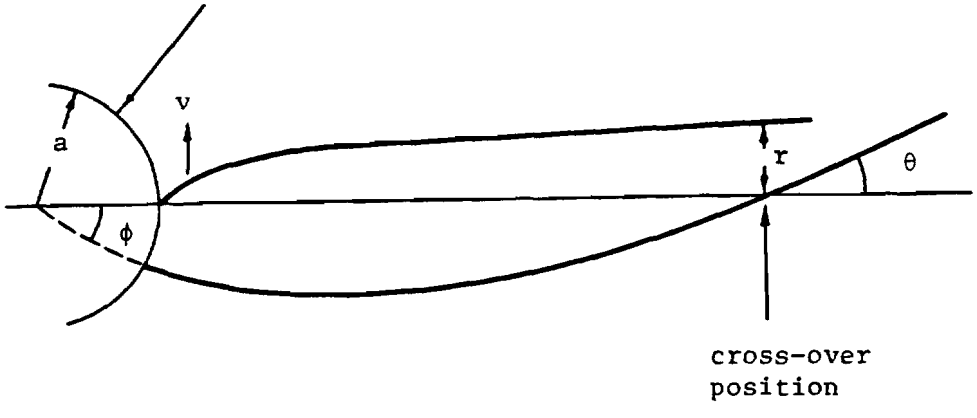

Figure 3-6. Electron gun cross-over.

The standard deviation of the Gaussian current density at the cross-over is thus proportional to the magnified tip radius.

Another important source parameter is the Gaussian source diameter. If the trajectories of electrons as they enter into a field-free space in the electron gun are projected back toward the emitter, they form a crossover which is the virtual object of the optical system. Several studies of this virtual source size have been made. El-Kareh[17] wrote a computer program with an automatically contracting mesh size to solve Laplace's equation for the entire electron gun. He computed a source diameter of approximately 120 Å for V = 5000 V and T = 1800 K.

Wiesner[18] used a sphere-on-cone emitter model and a plane anode with no aperture in front of the emitter:

> "...we note...that optimum apparent source radii for field emission are obtainable in the approximate range of two to four nanometers with beam half-angles (at the first anode) of two to eight milliradians. Operation of a 1.0 μm radius cathode in strong Schottky emission (E_{00} = 400 V/μm) can yield an apparent source radius of about five to seven nanometers. The source size degrades more and more rapidly for weaker applied fields."

Several authors[19,20] have considered the problem of the maximum attainable resolution of a field emission microscope (FEM), which gives a rough indication of the apparent source size. The geometry

of the FEM is so much different than that of the electron gun that it is not too useful to consider these studies in detail here.

A final electron optical parameter of the source to be considered here is the energy spread of the emitted electrons. The previously mentioned paper by El-Kareh et al.,[6] contained graphs of normal-, total- and tangential-energy distributions for various fields, temperatures, and work functions. Figure 3-7 reproduces some of the results of this paper for a work function of 2.7 eV. The total energy distribution is seen to have a FWHM value at 2000 K of about 0.5-0.7 eV.

As previously mentioned, Bell and Swanson[7] have measured a total energy spread which shows an anomalous broadening at high current densities. This is assumed to be due to a Boersch-effect collective coulomb interaction in the vicinity of the emitter. This anomaly increases the expected energy spread from approximately half a volt to one volt or greater at high angular current intensities ($\sim$ 1 mA/sr).

The collective coulomb interaction over an entire electron optical system has been investigated by Groves et al.,[21] by calculating electron trajectories on a computer. The area in the immediate vicinity of the field emitter was excluded from the coulomb interaction effect due to difficulties in calculating trajectories through several orders of magnitude of field strength. The field emission source was taken into account, however, by using a ray trace "seeded" by the velocity spread measured by Bell and Swanson and by a separate term of the magnified Gaussian source diameter. The effect of the

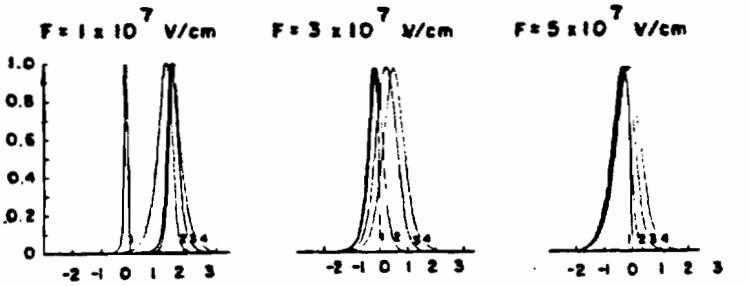

Normal Energy Distribution

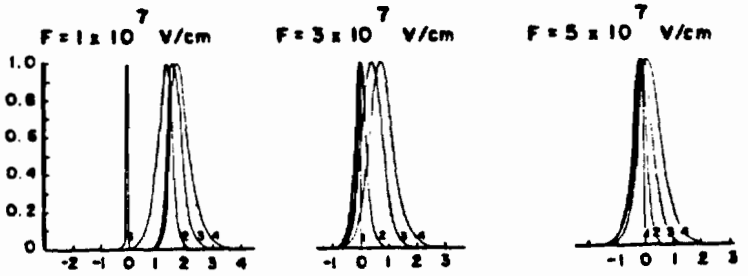

Total Energy Distribution

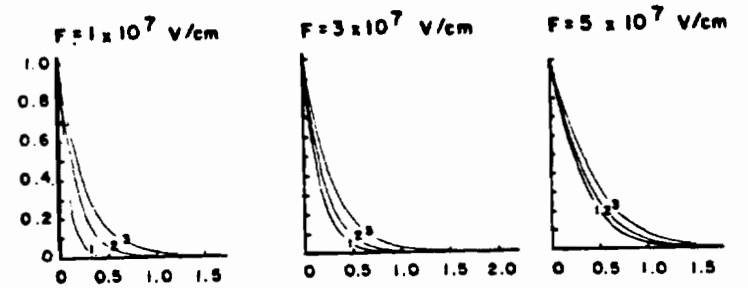

Tangential Energy Distribution

Figure 3-7. Graphs of the distribution of emitted electrons versus energy (eV) relative to the Fermi level for temperatures of (1) T = 1 K, (2) T = 1000 K, (3) T = 2000 K, (4) T = 3000 K. The maximum amplitude of each case is normalized to unity. ϕ = 2.7 eV.

coulomb interaction was to introduce a "broadening" term directly proportional to beam current and column length and inversely proportional to beam aperture angle. The results show that for a system similar to ours, a 0.1 μm spot diameter cannot be maintained at currents much above 100 nA. At greater currents the collective coulomb interaction over the length of the column increases the spot diameter.

G. Noise

In addition to the shot noise produced by any electron source,[22] the field emitted current contains noise produced by surface migration of atoms and adsorption and desorption of residual gases, resulting in work function fluctuations. Information contained in the spectral density function W(f) can be interpreted in terms of activation energies for surface diffusion,[23] adsorbate coverage,[24] and temperature. Gomer[25] has presented a method of determining surface diffusion coefficients on a single crystal plane from the autocorrelation of the noise current. Chen and Gomer[26] present some results, again in terms of autocorrelation, for the W(110) surface with oxygen adsorbate. The surface of the Zr/W<100> field emitter is a Zr-O-W composite structure[27] and therefore an interpretation of the spectral density function would be premature until it has been studied in more detail. The spectral density is presented in this paper in an operational sense, as it affects the S/N ratio of the Auger spectra generated by the system.

Space charge suppression of noise can be significant at high current densities for field emitters. Pushpavati and Van der Ziel[28] have shown theoretically that noise current increases with beam current until the current density attains a value on the order of 10^5 to 10^6 A/cm^2 at which point space charge noise suppression should cause the noise current to decrease with a further increase in beam current. Since the Zr/W<100> emitter is operated in our system with a current density on the order of 10^5 A/cm^2, this noise suppression mechanism may be operating but a decrease in noise percentage with current was not observed. An interesting further development in the above mentioned study is an electron velocity fluctuation due to current fluctuation which should vary inversely proportional to j/F^2. Since j increases exponentially ($e^{-1/F}$) with field, at some current density the velocity fluctuations in the emitted beam should start to be suppressed. Against this effect must be balanced the coulomb repulsive force between electrons as previously mentioned.

A noise contribution observed in multi-element vacuum tubes, partition noise is probably not operative in the Zr/W<100> TFE electron gun. Partition noise is an additional noise generated as a result of random distribution of current between various positive electrodes, which occurs when the following conditions may be assumed:[29]

1) For any small area of the cathode, an emitted electron always has the same probability of arriving at the target (going through the aperture).

2) Whether a particular electron will arrive at the anode or at the target is otherwise completely random.

We do have a partition of current between the target and the anode but the areas of the cathode which contribute to target current and to anode current are separate and the only place where both conditions would obtain would be an annular area on the cathode where the emitted electrons would intercept the aperture edge. It therefore seems that this effect would be insignificant. An equal amplitude and opposite phase noise current component would be present in the anode current if partition noise were present in the target current.

REFERENCES

1. J. Mayer and M. Mayer, "Statistical Mechanics" (Wiley, 1940), p. 387.
2. W. Schottky, Phys. Z. 15, 872 (1914).
3. R. H. Fowler and L. Nordheim, Proc. Roy. Soc. A 119, 173 (1928).
4. R. Gomer, "Field Emission and Field Ionization" (Harvard Univ. Press, 1961), p. 10-11.
5. E. L. Murphy and R. H. Good, Phys. Rev. 102, 1464 (1956).
6. A. B. El-Kareh, J. C. Wolfe and J. E. Wolfe, J. Appl. Phys. 48, 4749 (1977).
7. A. E. Bell and L. W. Swanson, Phys. Rev. B 19, 3353 (1979).
8. L. W. Swanson and N. A. Martin, J. Appl. Phys. 46, 2029 (1975).
9. V. N. Shrednik, Sov. Phys.-Solid State 3, 1268 (1961).
10. N. A. Martin, private communication.
11. J. E. Wolfe, J. Vac. Sci. Technol. 16, 1704 (1979).
12. P. Grivet, "Electron Optics" (Pergamon Press, 1972), p. 109.
13. D. B. Langmuir, Proc. Inst. Radio Engrs. 25, 977 (1937).
14. H. Moss, "Narrow Angle Electron Guns and Cathode Ray Tubes" (Academic Press, 1968), 205 ff.
15. J. Worster, J. Phys. D 2, 457 (1969).
16. J. Worster, J. Phys. D 2, 889 (1969).
17. A. B. El-Kareh, J. Vac. Sci. Technol. 12, 1227 (1975).

18. J. C. Wiesner, "Point Cathode Electron Sources," Ph.D. Dissertation, University of California, Berkeley, Ch. 3 (1970).

19. R. H. Good and E. W. Müller, "Handbuch der Physik" Bd. XXI, p. 203 ff.

20. R. Gomer, J. Chem, Phys. 20, 1772 (1952).

21. T. Groves, D. L. Hammond, and H. Kuo, J. Vac. Sci. Technol. (in press).

22. O. Klemperer, "Electron Physics" (Butterworths, 1972), p. 89 ff.

23. J. Beben, Ch. Kleint and R. Meclewski, 26th Intl. F E Symp. (West Berlin, 1979), p. 64.

24. Ch. Kleint, R. Meclewski, and R. Blaszczyszyn, Surf. Sci. 70, 151-164 (1978).

25. R. Gomer, Surf. Sci. 38, 373-393 (1973).

26. J. Chen and R. Gomer, Surf. Sci. 79, 413-444 (1979).

27. L. R. Danielson and L. W. Swanson, Surf. Sci. 88, 14-30 (1979).

28. P. J. Pushpavati and A. Van der Ziel, IEEE Trans. on El. Dev. ED-12, 395-398 (1965).

29. A. Van der Ziel, "Noise" (Prentice-Hall, 1954) p. 106.

CHAPTER 4

AUGER ELECTRON SPECTROSCOPY

A. Theory

Auger electron spectroscopy (AES) is a well established tool for the analysis of the chemical composition of surfaces. The Auger effect, discovered in 1925 by Pierre Auger,[1] was first observed in a cloud chamber which had been irradiated by x-rays. He noted that electrons of constant energy were emitted, even though the x-ray energy was varied.

In the application of the Auger effect to surface chemical analysis, a sample in an ultrahigh vacuum (UHV) system is bombarded with a beam of 3 to 10 keV electrons. Some of these electrons will collide with inner shell electrons in the atoms of the sample, knocking them out of the atom (say from the K shell). (See Figure 4-1.) Then an electron from a higher energy level (say the L_1 shell) will drop to the K shell to fill the vacancy. The energy from this transition can be released either as an x-ray photon or as an Auger electron. The Auger electron is an electron (say from the L_3 shell) that is ejected from the atom and becomes part of the secondary yield. The overall Auger process is described by the shells involved (KL_1L_3). Transitions can occur involving other shells, e.g., MNN, LMM, LLV where V denotes the valence band. Since three energy levels are involved,

and at least two core electrons, hydrogen does not produce Auger electrons. Where the valence band is involved, information about the valence band density of states may be obtained from the shape of the Auger spectral peak.

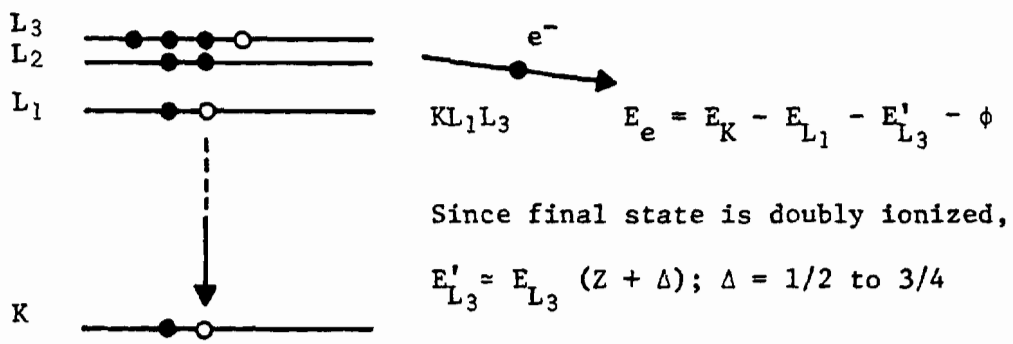

Figure 4-1. Auger transition.

Figure 4-2 shows the x-ray yield and Auger electron yield vs. atomic number of the target material. This illustrates one of the advantages of AES over x-ray spectroscopy for low atomic number elements.

If an electron spectrometer is used to obtain a spectrum of the number of secondaries vs. energy (N(E)), then the spectrum will show small peaks where the Auger electron characteristic energies lie. Since the peaks show up only as small bumps on the large background signal of the N(E) spectrum, a derivative spectrum dN/dE is usually

used and the peak heights of the dN/dE spectrum are used to obtain quantitative results.

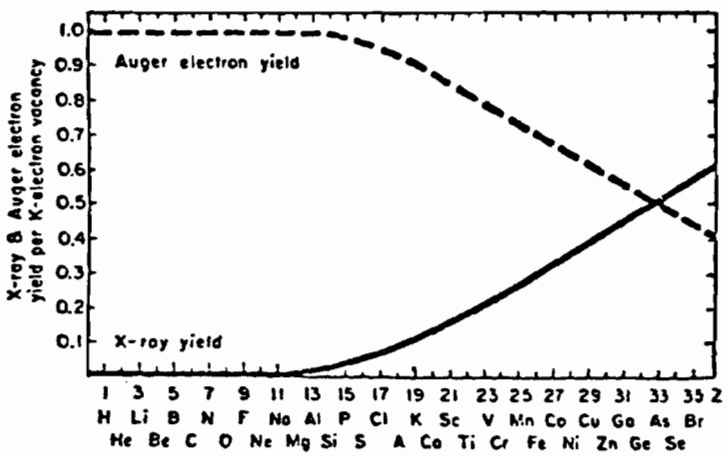

Figure 4-2. Yield vs. atomic number.

AES is extremely surface sensitive for although Auger electrons are produced as far into the bulk as the primary beam will penetrate, in order for them to be detected as an Auger peak, they must not lose energy in getting to the surface. Since Auger electrons range in energy from 20 to 2000 eV, the degree of surface sensitivity is dependent to some extent on the particular peak used. Experimental data[2] indicate a range of surface sensitivity from 5 to 20 angstroms, depending on the target material.

Palmberg[3] pointed out the way to get useful quantitative results from Auger spectra. He showed that absolute sensitivity factors can be assigned to all elements which are modified only by a

matrix-dependent backscattering factor. Books of Auger spectra for the elements are available which allow quantitative analysis based on peak to peak height of the differentiated spectrum.

B. Instrumentation

AES was not used routinely until the development of two techniques which allowed the construction of systems with high detection efficiencies. One technique involved the use of an improved electron spectrometer over the modified Low Energy Electron Diffraction (LEED) systems which were initially used.

The cylindrical mirror analyzer[4] (CMA) uses the geometry shown in Figure 4-3 to produce a second order focus for electrons of a selected energy.

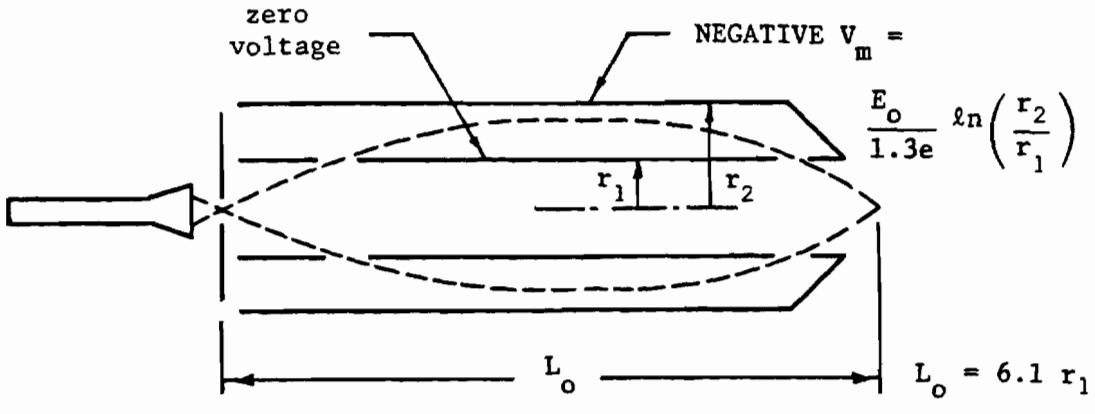

Figure 4-3. CMA diagram.

An aperture is placed at the focal point, the size of which determines the energy resolution of the CMA. Physical Electronics Industries (PHI) makes a CMA with selectable apertures for resolutions of 0.2, 0.6, and 1.2%. This allows the tradeoff between data acquisition time (signal level) and energy resolution to be varied to suit conditions. An electron multiplier is positioned behind the aperture. The energy window of the device is varied simply by changing the voltage on the outer cylinder. This spectrometer has a typical transmission of 10 to 15%.

The other technique which brought AES into routine use was the method of detecting the differentiated spectrum and doing all comparisons in terms of differentiated spectra. A comparison of N(E) and dN/dE spectra is shown in Figure 4-4.

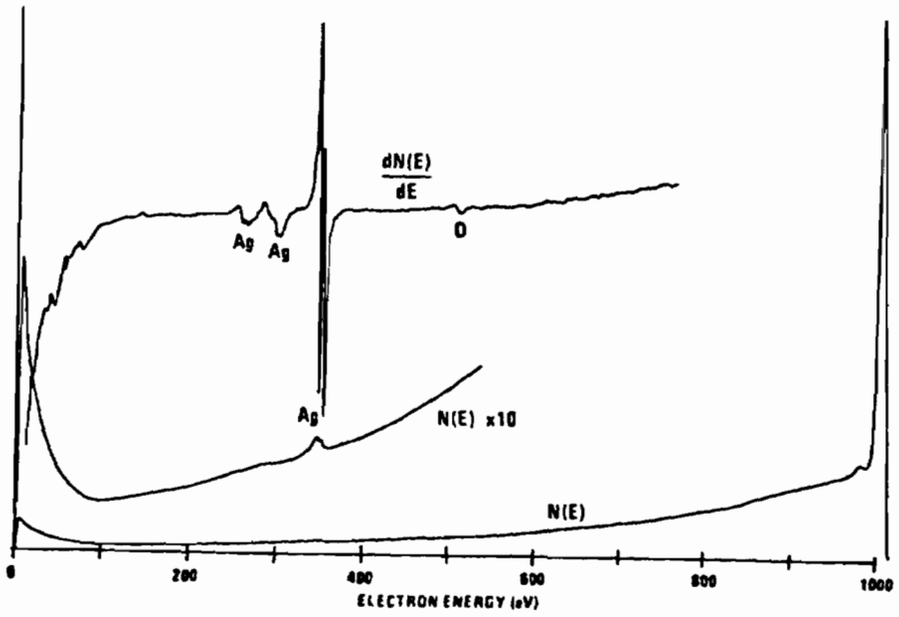

Figure 4-4. Auger spectrum (Ag).

The differentiation of the spectrum is accomplished with a lock-in amplifier. If the outer cylinder of the CMA is modulated with the reference output so as to vary the energy window slightly about its set value, and the electron multiplier output is fed to the lock-in amplifier input, the lock-in amplifier output is proportional to dN/dE. Two methods can then be used to average out noise fluctuations to obtain a usable spectrum. The lock-in time constant can be increased to bandwidth limit the output, thus requiring a reduction of scan rate of the spectrum. Alternatively, if a signal averager is available, a better method is to perform high speed repetitive scans with the lock-in time constant turned off and average the output.

Fairly recently, digital techniques have produced N(E) spectra for use with primary beam currents below 10 nA. Surface topography effects are accentuated in the N(E) spectrum, but they can be corrected for by non-real time computation. Sensitivity factors are not yet available for N(E) spectra. Low primary beam currents are desirable to minimize surface damage, so in a few cases it is necessary to use N(E). When possible, it is easier and quicker to use a higher beam current and the dN/dE mode of data collection. Topographical effects are minimized by differentiation. If it were possible to collect the electrons which are stopped by the energy resolving aperture in the CMA, this current could be used to correct for residual topographical effects in the dN/dE spectrum.

C. Auger Signal Detection[5]

The cylindrical mirror analyzer (CMA) response function can be significantly affected by the termination of the field at each end of the mirror, by stray magnetic fields, and by electron multiplier characteristics. Neglecting these difficulties, the analyzer transmission can be assumed to be a Gaussian peak on the electron energy spectrum.

$$\text{Transmission} = \int_{-\infty}^{\infty} \exp\left[-\alpha\left(\frac{E - E'}{E}\right)^2\right] N(E')\, dE'.$$

As $\alpha \to \infty$, the Gaussian peak approaches a delta function. For an analyzer resolution $\Delta E/E$ of 0.8%, $\alpha \simeq 4$. If the resolution is sufficiently great, the Gaussian integral of $N(E')$ can be replaced by the average of the function over E. The above integral then becomes

$$N(E)\ \Delta E = \left(\frac{\Delta E}{E}\right) N(E)\ E.$$

The Gaussian analyzer response peak must be smaller than the Auger peak for this equation to hold. Extracting the constant resolution from the above equation, the unnormalized transmission of the CMA becomes

$$E \cdot N(E). \tag{4-1}$$

Because of the constant resolution $\Delta E/E$, the analyzer yields proportionally greater signals for greater energies, even though the

N(E) may be unchanged. The instrument resolution is usually determined experimentally by scanning the elastic peak.

The modulating voltage is applied to the CMA mirror element as a sine wave superimposed on the dc analyzing voltage. Expanding this function in a Taylor series about the point sin $\theta = 0$,

$$N(E + a \sin \theta) = N(E) + aN'(E) \sin \theta + (a^2/2)\, N'' \sin \theta + \ldots$$

The powers of the sine function are then converted to harmonics by trigonometric identities.[6] The coefficients of the first and second harmonics are

$$\text{1st harmonic} = aN^{I}(E) + (a^3/8)\, N^{III}(E) + (a^5/192)\, N^{V}(E) + \ldots$$

$$\text{2nd harmonic} = (a^2/4)\, N^{II}(E) + (a^4/48)\, N^{IV}(E) + (a^6/1536)\, N^{VI}(E) \ldots$$

where the superscript Roman numerals refer to the order of the derivative. For small modulation (small a) the first harmonic (fundamental) is proportional to the first derivative of the energy spectrum, the second harmonic to the second derivative, etc. If the modulation is increased, becoming comparable in width to the N(E) peak width, the signal is distorted by the addition of higher derivative terms and the proportionality between signal strength and modulation amplitude is lost. Also, if the modulation is small, the fact that the CMA response is E·N(E) instead of just N(E) can be taken into account by just multiplying the harmonics by a factor proportional to E.

A tuned phase lock amplifier produces an output

$$V_{out} = \frac{1}{2\pi} \int_0^{2\pi} V_{in} \sin \theta \, d\theta,$$

neglecting amplifier gains which just contribute a scale factor. If the signal $N(E + a \sin \theta)$ is sent to the input of a tuned input lock-in amplifier, the output is

$$V_{out} = \frac{1}{2\pi} \int_{\pi/2}^{5\pi/2} N(E + a \sin \theta) \sin \theta \, d\theta.$$

Let $E' = -a \sin \theta$; then

$$V_{out} = -\frac{1}{a\pi} \int_{-a}^{a} N(E - E') \frac{E'}{(a^2 - E'^2)^{1/2}} \, dE' .$$

This has the form of the convolution of two functions: the input function $N(E - E')$ and the instrument response function $E'/(a^2 - E^2)^{1/2}$. In this case, the "instrument" is the lock-in amplifier with sinusoidal modulation. The modulation is an integral part of the "instrument" since different modulations produce different instrument responses. Figure 4-5 is a plot of this response function.

Convoluting the response function with a Gaussian peak shape (assumed) for both small and large modulation amplitudes, output signals result as shown in Figure 4-6.

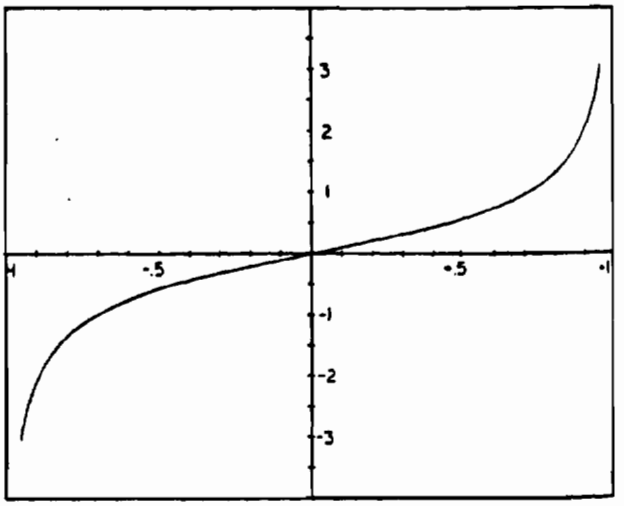

Figure 4-5. Lock-in amplifier response function.

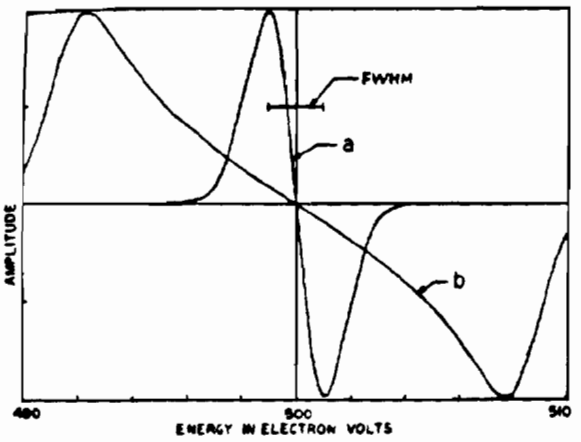

Figure 4-6. Response to Gaussian peak.
(a) 0.25 eV p-p modulation.
(b) 20 eV p-p modulation.

The relative intensity between the curves a and b of Figure 4-6 is ~ 60. The assumed Gaussian FWHM was 2 eV and the two modulations are (a) 0.25 eV p-p and (b) 20 eV p-p. For the large modulation, the signal is no longer an approximation to the derivative.

Figure 4-7 is a normalized plot of the peak to peak signal heights vs. modulation amplitude, also normalized to ΔE, the FWHM of the Gaussian peak. Since a Gaussian peak has been assumed, this model is only an approximation to the Auger spectrum.

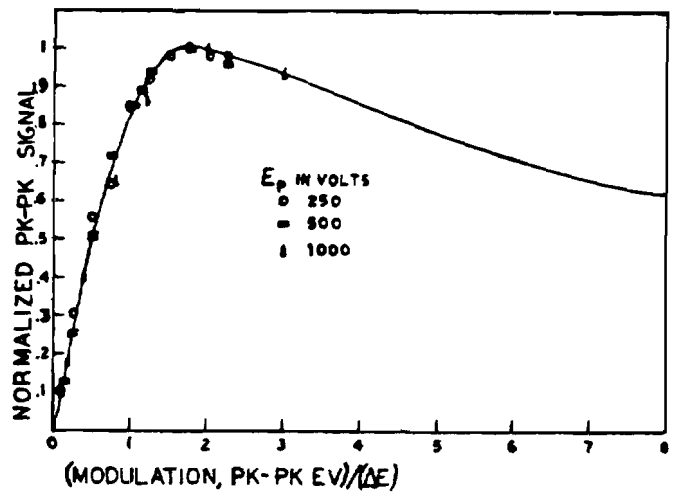

Figure 4-7. Auger signal vs. modulation amplitude.

D. Auger S/N Considerations

The rms shot noise associated with an electron beam probe current of I_p is

$$\text{rms } \Delta I_p = \sqrt{2eI_p\Delta f} \tag{4-2}$$

where Δf is the bandwidth in which the noise is measured. Assuming that the secondary emission process yields a current $I_s = \delta(E)\ I_p$ where δ is the secondary emission ratio which is a function of E_s, the secondary energy and E_p, the primary beam energy, and further assuming that E_p is constant and that, to the first approximation, each primary liberates exactly δ secondaries, the fluctuation in secondary emission current is

$$\text{rms } \Delta I_s = \sqrt{2eI_p\delta^2(E_s)\Delta f}$$

whereas the secondary current itself is just

$$I_s = \delta(E_s)I_p$$

The S/N ratio of the secondary current I_s is therefore

$$\frac{S}{N} = \frac{I_s}{\text{rms } \Delta I_s} = \sqrt{\frac{I_p}{2e\Delta f}} \tag{4-3}$$

If the S/N of a secondary signal is proportional to $\sqrt{I_p}$, then it can be inferred that the primary beam is shot noise limited, at

least to the first approximation.

Now let's add some complicating factors to this simple model to see how an ideal system would respond to a primary beam containing fluctuations above shot noise.

A typical Auger (dN/dE) measurement setup with a lock-in amplifier may operate at 8 kHz, with the time constant set to 0.3 sec, a 4 eV p-p modulation, a 4 eV/sec scan rate with E_p = 8 kV and I_p = 25 nA. Since the electron detector in the CMA is capacitively coupled to the lock-in amplifier, the noise rejection of the lock-in amplifier reduces the ~ 8 kHz I_p fluctuations to a negligible value. Borrowing from the results section of this thesis, the spectral density at 8 kHz (extrapolated) for I_p = 30 nA is on the order of $2 \cdot 10^{-25}$ A^2/Hz. For a tuned front-end lock-in amplifier with a Q of 10 at 8 kHz, the bandwidth is 800 Hz and the rms ΔI_p is 12.7 pA which is a noise percentage of .04%. Shot noise at this bandwidth would produce an rms ΔI_p of 2.8 pA, or .009%. This noise is eliminated almost completely by the phase-sensitive detector and the final RC time constant. It is only when the time constant is turned off and multiple scans are computer averaged that this noise could appear in the output.

Having thrown out the high frequency noise by phase sensitive detection and filtering, the portion of the primary beam noise spectrum which gets through the lock-in amplifier and appears at the output is determined by the low pass output filter. These filters typically rolloff at either 6 or 12 dB/octave.

For simplicity, assume that the filter is a sharp-cutoff low pass filter. Then only that part of the primary beam noise spectrum below the filter cutoff will be seen in the output. Since the Zr/W <100> TFE emitter has a plateau on the noise spectral density which extends to ~ 200 Hz (see Figure 7-7) at a level of ~ .03% rms noise/$\sqrt{Hz}$ whereas shot noise for this same current level (30 nA) amounts to ~ .0003% rms noise/$\sqrt{Hz}$, one might expect the field emitter to be 100 times noisier than a thermionic cathode in the Auger application. There are two reasons why this may not be the case.

First, the thermionic cathode used in many scanning Auger systems (LaB_6) doesn't produce a shot-noise beam current. A measurement of this cathode[7] showed a noise level at 100 Hz of ~ .002%/$\sqrt{Hz}$ for an 82 nA beam, whereas the shot-noise associated with 82 nA is .0002%/$\sqrt{Hz}$ (see Figure 4-8). Therefore, the field emitter may appear in comparison to a LaB_6 source to produce ~ 10 times the noise in an Auger signal rather than 100 times.

Second, consider the actual current that passes through the CMA aperture and is amplified by the channeltron and the lock-in amplifier. The Auger yield is typically 10^{-4} and the CMA transmission is ~ 10^{-1} giving a net attenuation to the primary current of 10^{-5}. With a 30 nA primary beam, the detected Auger current is 0.3 pA. The shot noise associated with 0.3 pA is ~ 0.1%/$\sqrt{Hz}$. Of course, this Auger peak is riding on a background current much larger than 0.3 pA, say 3 pA, which corresponds to a shot noise of .03%/$\sqrt{Hz}$, the same as the primary beam noise at 30 nA from the thermal field emitter.

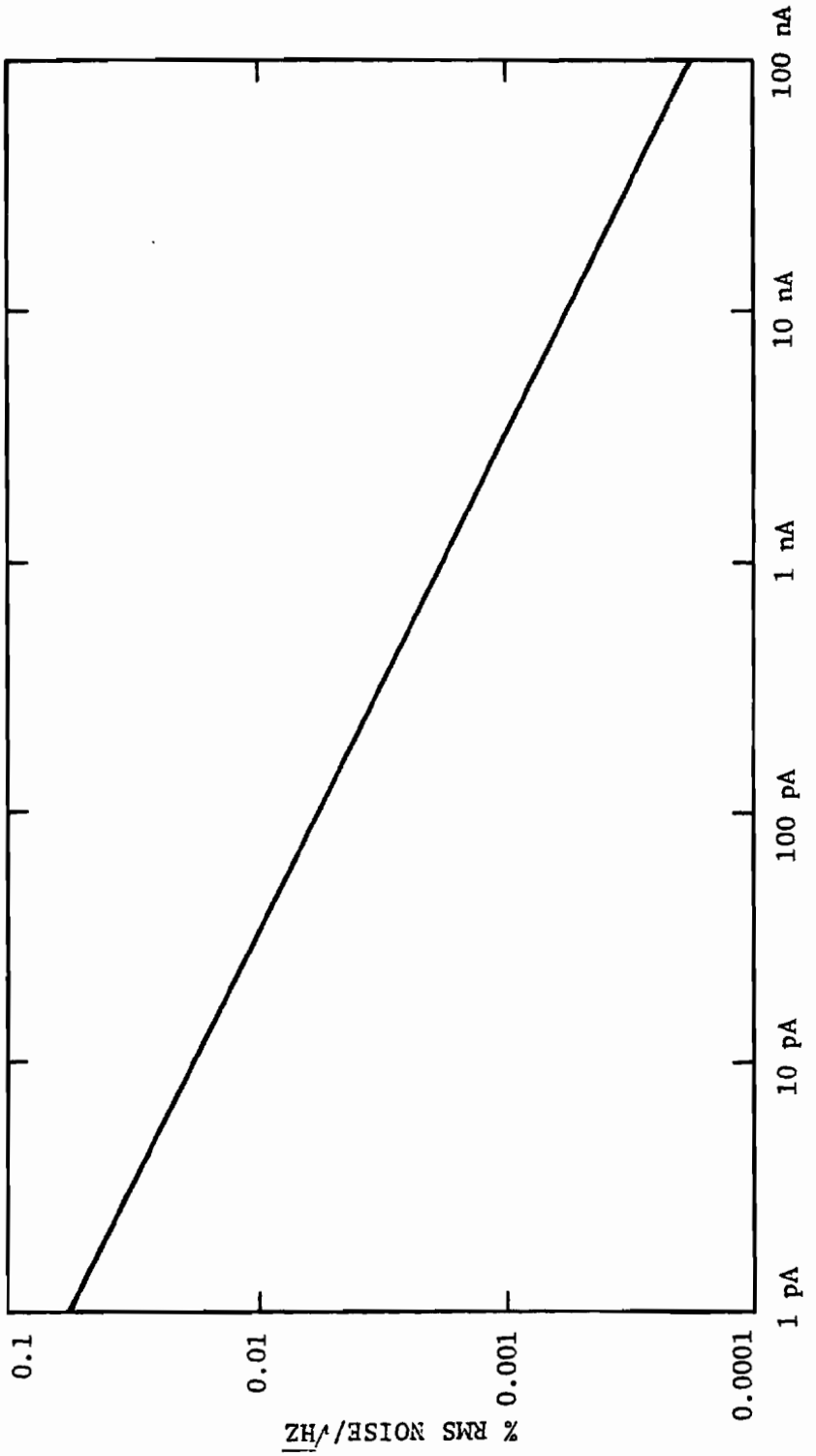

Figure 4-8. Shot noise.

Therefore, the Auger process and the detection efficiency together attenuate the primary current so much that the detected Auger current shot noise is comparable to the primary beam noise. If the attenuation factor were more severe as in the case of a bad CMA or improper alignment, the detected Auger current noise would outweigh the primary beam noise and the system would be shot-noise limited, but not because of low primary beam noise.

The preceeding argument has ignored the fact that the Auger process and the secondary emission process are random processes, which means that they will create secondary electron current fluctuations, even with a noiseless primary beam current. Secondary emission noise is treated by Van der Ziel.[8] It is generally a small effect.

After the above argument was written a paper[9] containing a similar argument was noticed in connection with studies of the voltage contrast mechanism in electron microscopy. That work uses the very descriptive term "noise bottleneck" to refer to the place in the signal path at which the number of signal carrying quanta is minimum.

REFERENCES

1. M. P. Auger, Compt. Rend. 180, 65 (1925).
2. M. P. Seah, Surf. Sci. 32, 703 (1972).
3. P. W. Palmberg, J. Vac. Sci. Technol. 13, 214 (1976).
4. H. Z. Sar-el, Rev. Sci. Instrum. 38, 1210 (1967).
5. The information in this section, including the three figures, is from R. W. Springer and D. J. Pocker, Rev. Sci. Instrum. 48, 74 (1977).
6. N. J. Taylor, Rev. Sci. Instrum. 40 792 (1969).
7. Data taken April 9, 1980 on PHI Scanning Auger Microprobe.
8. A. Van der Ziel, "Noise," (Prentice-Hall, Inc., 1954), p. 112.
9. Y. C. Lin and T. E. Everhart, J. Vac. Sci. Technol. 16, 1856 (1979).

CHAPTER 5

SYSTEM CONFIGURATION

A. Gun, Optics, Alignment

An overall diagram of the field emission (FE) scanning Auger microscope (SAM) system is shown in Figure 5-1. The upper lens was operated at a focal length of 63 mm and collimated the emission transmitted through a 0.30 mm anode aperture located 25 mm from the emitter. The lower lens was operated at a focal length of 139 mm and focused the collimated beam onto the specimen. Geometric constraints of the bell jar system prevented closer working distances than about 13 cm.

For this optical system the overall magnification M is given by the ratio of lower lens focal length f_2 to upper lens focal length f_1

$$M = f_2/f_1$$

The apparent object size at the object plane of the first lens is then obtained by adding in quadrature[1] the Gaussian, diffraction, spherical and chromatic aberration disks d_g, d_d, d_s and d_c, respectively:

$$d_1^2 = (d_g^2 + d_{d_1}^2 + d_{s_1}^2 + d_{c_1}^2)$$

where

$$d_g = 150 \text{ Å (est)}$$

$$d_{d_1} = 15.1/V^{1/2}\alpha(\text{Å})$$

$$d_{s_1} = (1/2)C_{s_1}\alpha^3$$

$$d_{c_1} = C_{c_1}\alpha\Delta V/V$$

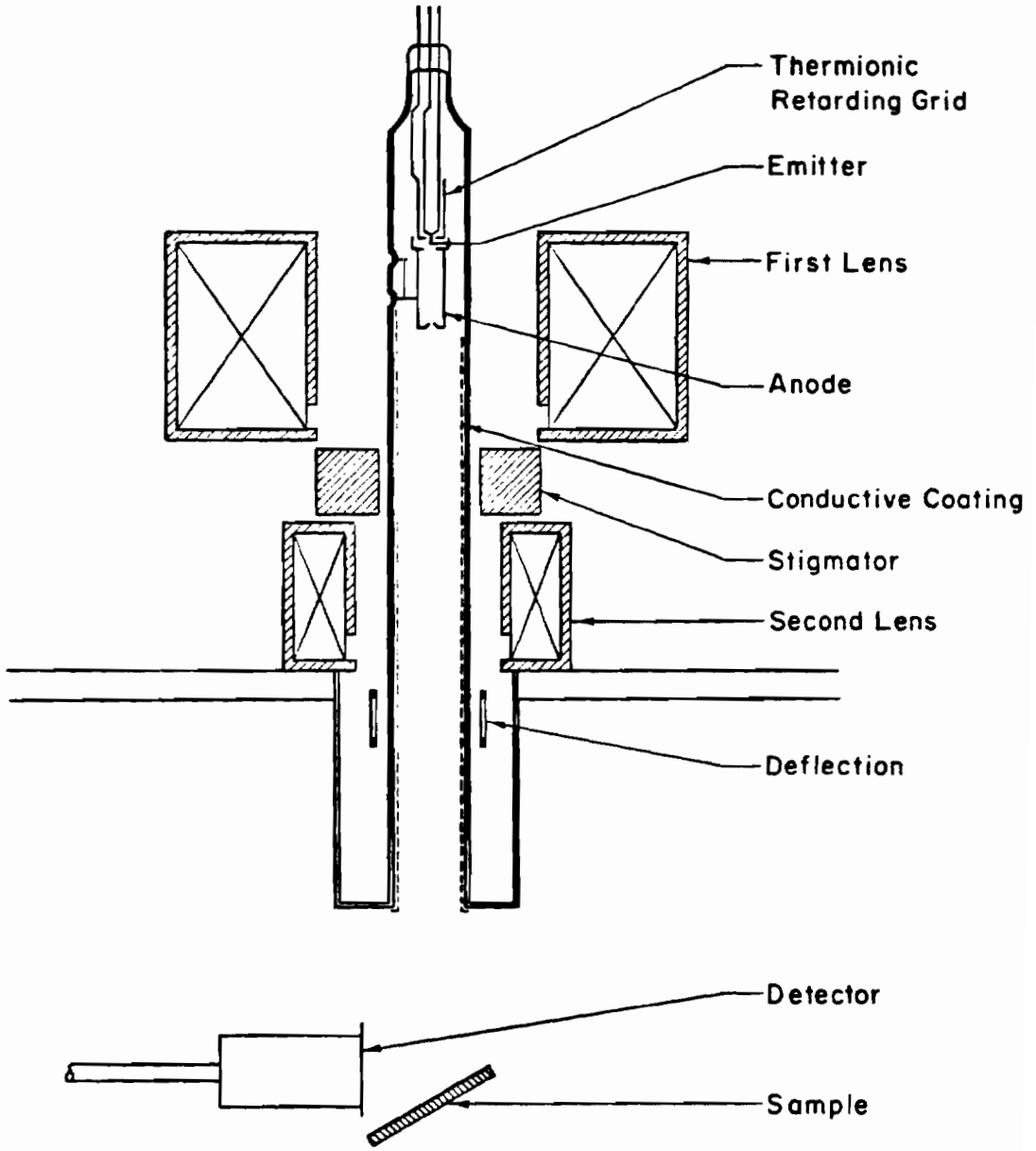

Figure 5-1. Field emission scanning Auger microscope.

In the above formulation V is in volts, α is the aperture half angle subtended at the source and C_{s_1} and C_{c_1} are referred to the object side of the lens. Similarly, for the lower lens the final spot size d_2 is

$$d_2^2 = (Md_1)^2 + d_{s_2}^2 + d_{c_2}^2$$

where d_{s_2} and d_{c_2} are the spherical and chromatic contributions of the lower lens.

The lens aberration coefficients were obtained from a computer program written by Munro,[3] which calculates the axial magnetic field of the lens with boundary conditions determined by the lens gap and bore geometry. The lens aberration coefficients are then found by integrating the paraxial ray equation with the calculated axial field.

The electron gun structure shown in Figure 5-2 consists of a cathode (precision mounted in a molybdenum emitter sleeve), a suppressor electrode and an anode. This gun has previously been described by Wolfe,[4] El-Kareh[2] and Fontijn.[5] The tungsten hairpin filament requires approximately 2.3 A at 0.8 V. This is supplied by a floating high frequency current-regulated dc supply. The suppressor electrode is supplied by a floating battery (300 V). This suppressor electrode prevents the thermionic emission from the tungsten hairpin filament and the field emitter shank from getting through the beam defining aperture. It also reduces the anode current which prevents excessive anode outgassing. The anode connection is brought out through the

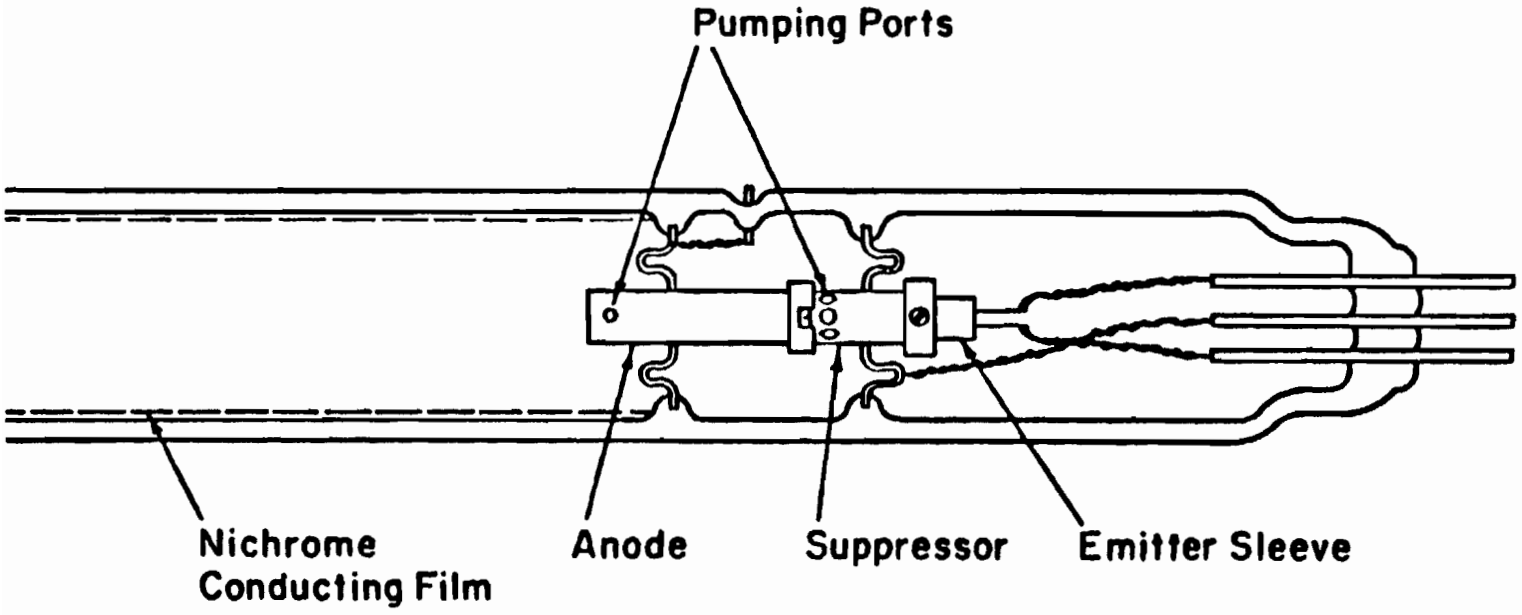

Figure 5-2. Magnetically focused thermal field electron gun.

glass and connected to the total current meter which returns the anode current to ground. Using computed trajectories from the field emission tip, El-Kareh[2] has determined the effective Gaussian source size to be approximately 120 Å for this gun. The replaceable beam-defining aperture at the bottom of the anode was .012 in. diameter and at a distance of 1.0 in. from the field emitter tip.

The upper lens (Celco PF-648-380) was driven by a current regulator (Celco SR1000A). The lower lens was driven directly by a well regulated power supply. Lens alignment was accomplished by first focusing with the upper lens alone at low magnification. A low frequency sine wave modulation was applied to the current regulator input to vary the lens current about its focused value. The resulting motion of the image on the CRT monitor (SEM mode of operation) was minimized by lateral centering of the lens. The stigmator was then aligned by the procedure indicated below. The lower lens was aligned in a similar way to the upper lens. This procedure was iterated to convergence. It was not necessary to adjust the tilt of the upper lens.

An eight pole stigmator was located between the lenses. Two quadrupole saddle coil sets were wound on the same coil form, displaced 45° relative to each other. Each quadrupole was fed from a bipolar current-regulated supply. This arrangement produced the overall effect of an electrically rotatable quadrupole of variable strength. Each set of opposing coils had a potentiometer arranged to balance the currents so as to place the quadrupole center at the

beam axis. Stigmator alignment was accomplished by first adjusting the stigmator for the best image and then modulating the drive current to each quadrupole while adjusting the balancing pots for no motion of the SEM image on the CRT.

The saddle coil deflection yoke was centered between the bottom of the lower lens and the glass-to-metal seal. The metal part of the seal was non-magnetic, but at TV scan rates used in the deflection coils, eddy currents would be induced in the metal which would degrade the field linearity, if the coils were placed near the metal. The deflection yoke consists of two yokes wound on the same form. One is used for high magnification (2 turns) and the other for low magnification (20 turns). This decreases the dynamic range required of the deflection amplifier and lessens the effects of electrical noise generated in the deflection electronics. The yoke is driven by a current feedback amplifier. The area over which the field is uniform within the yoke is large enough so that mechanical centering of the yoke with the glass tube is sufficient. No electrical centering adjustments are necessary.

B. Vacuum Chamber Instrumentation

Two channeltron secondary electron detectors (Galileo Electro-Optics CDEM 4700) were installed in the vacuum system. Due to physical constraints, they were located on nearly the same plane as the specimen and approximately 3 in. distant from it. Since the secondary electron yield shows a cosine dependence on the angle relative

to the normal in the specimen, the detectors are in far from optimum positions. The top view of the chamber shows the location of these detectors, the CMA, and the ion gun. See Figure 5-3. The channeltron adjacent to the CMA lost nearly all (96%) of its video signal when the CMA was moved up to the specimen for Auger work. The other channeltron lost only about 40% of its video signal and so it provided a usable signal for positioning the specimen with the CMA in place.

The output of the channeltron in use was a-c coupled to a FET input operational amplifier (Optical Electronics 9725) which fed a 50 ohm line terminated at the equipment rack. This provided a video bandwidth of 3 MHz. which was adequate for the present work. A higher speed amplifier (Burr-Brown 3554) will replace this one in the future to increase the bandwidth to 10 MHz.

The CMA (PHI 06-150) used an internal channeltron-type multiplier which was operated at approximately 2000 V. The analyzer transmission was 10% and energy resolution was 0.8%. CMA operating voltages were provided by a standard Auger electronics system (PHI 11-500A).

The ion gun, used for sputter cleaning specimens and Auger depth profiling, was a PHI 04-161. The specimen stage (PHI 15-600) had 12 sample positions on a rotatable, removable sample carousel. One of the sample positions had a built-in Faraday cup which was used for spot size measurements.

The spot size measurement device is shown in Figure 5-4.

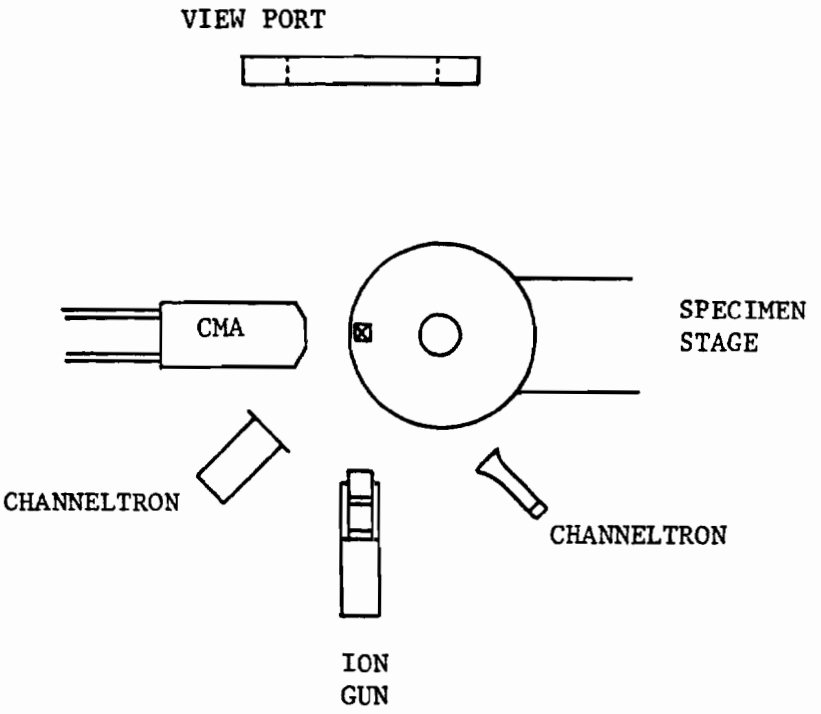

Figure 5-3. Vacuum chamber, top view.

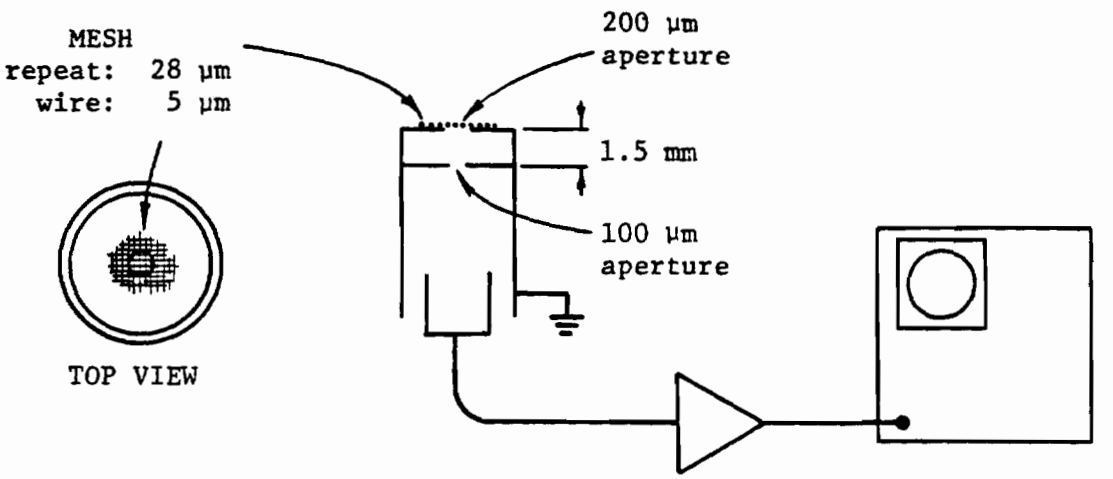

Figure 5-4. Spot diameter measuring device.

The Faraday cup picks up the primary current as the beam is scanned over a mesh of 5 μm wires. The current is amplified by another OEI 9725 op amp operating in the transconductance mode.

C. Magnetic Shielding

The large number of ports at the sides of the vacuum system bell jar prevented effective magnetic shielding. The earth's field (0.5 Gauss) and various stray a-c fields (0.01 Gauss p-p) present were shielded from the electron gun and lenses by a double mu-metal capped cylindrical shield with an aluminum spacer. Another small double shield was placed outside the deflection coils. This extended from the bottom of the lower lens to within about an inch of the specimen. A disadvantage of using this small shield is that it conducts some of the fringing fields outside the lens gap. This

creates two problems. First, the lower lens field is slightly distorted which may increase aberrations. Second, the d-c field in the vicinity of the specimen is increased which degrades Auger electron sensitivity. The combination of the two double shields reduced the effect of the a-c fields to where they contributed only about 0.2 μm p-p modulation of the beam position, which was locked out by line-frequency synchronization of the scan.

When the CMA was positioned close to the sample, its cylindrical magnetic shield concentrated the earth's field at the sample so that approximately 1 Gauss was present at the sample position. This field is anisotropic and not only created astigmatism in the beam but also is probably one reason for the poor Auger S/N ratio.

In retrospect, for systems involving low energy electron beams (such as this one) and especially for Auger work, the magnetic shielding should be considered at the outset to be at least as important as the electron optics. It is very difficult to try to "tack on" adequate shielding if a system has not been designed with this in mind.

REFERENCES

1. O. C. Wells, "Scanning Electron Microscopy," (McGraw Hill, 1974) p. 70.

2. A. B. El-Kareh, J. Vac. Sci. Technol. 12, 1227 (1975).

3. E. Munro, "A Set of Computer Programs for Calculating the Properties of Electron Lenses," (Engineering Dept., Univ. of Cambridge, 1975).

4. J. E. Wolfe, J. Vac. Sci. Technol. 12, 1169 (1975).

5. L. A. Fontijn, J. Vac. Sci. Technol. 15, 1053 (1978).

CHAPTER 6

EXPERIMENTAL PROCEDURE

A. Beam Diameter Measurements

Three different methods all involving measurement of the rise time of a scanned beam were used to determine the size of the focused beam. One of the methods involved the use of an apertured Faraday cup to measure transmitted current past a knife edge. We used a rectangular cross section wire which permitted its use as a knife edge in certain orientations relative to the beam. The grid was scanned in the SEM mode and an edge with suitable orientation was selected. The rise time of the electron current transmitted past the edge into the cup was used to obtain the beam size measurement. The same target was used to measure beam size from the rise time of back-scattered electrons. A third beam size measurement technique was to take a line scan over MgO particles deposited on a clean silicon surface. When particles smaller than the beam were scanned, the secondary electron signal traced out the beam profile. All methods used a line-frequency locked scan to eliminate the perturbation of a small stray 60 Hz field.

Joy[1] has described techniques for measuring spot size for an SEM. Since our system delivers orders of magnitude more beam current than a typical SEM, some of his elaborate measures to optimize S/N ratio for the Faraday cup were not required. Our basic spot size measurement

technique was suggested in a paper by Verhoeven and Gibson.[2] When using a doubly apertured Faraday cup one must ensure that the lower aperture (below the image plane) does not obstruct any part of the beam diverging cone.[3] If the outer edges of the beam are obstructed, even though the obstruction is past the image plane, the convergence angle at the image plane is effectively decreased, as shown in Figure 6-1. Thus the spot diameter will appear better than it actually is.

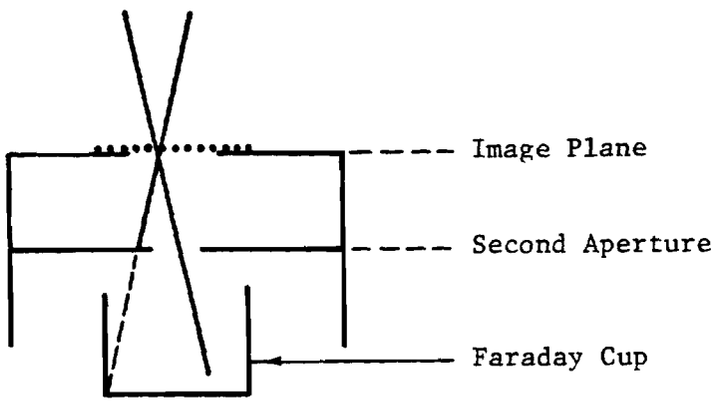

Figure 6-1. Beam diameter measurement device.

A comparison of various methods of spot size measurement can be done if one assumes a Gaussian current density distribution in the beam. This is generally true if the probe size is greater than several hundred angstroms.[1] In scanning an electron beam over a knife edge, the rise time of the current between the 4-96%,[4] 1/12-11/12 (8.3-91.7%),[2] 10-90%,[4] and 15-85% amplitude levels has been used to define the diameter in various publications. In the line scan of the MgO particle, the most convenient measurement was the

FWHM of the Gaussian peak. The current transmitted past a knife edge can be differentiated to yield a Gaussian waveform, and again the most convenient measurement is the FWHM. Another spot diameter definition was used in the paper on electron beam chromatic and space charge broadening by Groves, et al.[5] They used a tangent line at the mid-point of the rise of the transmitted current past a knife edge which was extended to the 0% and 100% amplitude levels. The intersections of the tangent line with those levels defined the beam diameter, as shown in Figure 6-2.

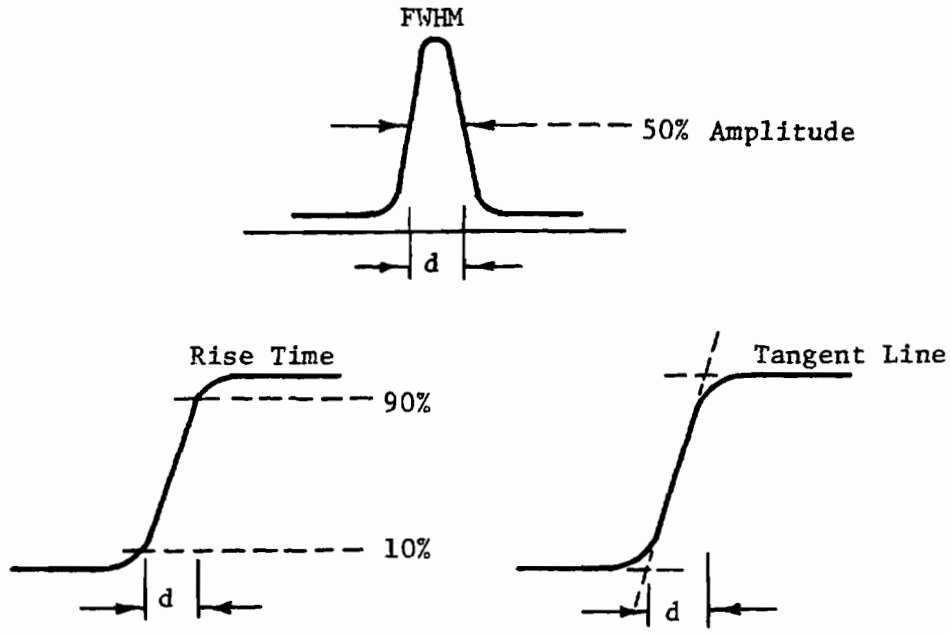

Figure 6-2. Beam size measurement conventions.

Using standard tables of the Gaussian function,[6] Table 6-1 was produced to compare the various methods of spot size measurement to the Gaussian FWHM method, which was used in this study.

TABLE 6-1

BEAM SIZE MEASUREMENT COMPARISONS

Amplitude Points for Rise Times	Method	% Total Beam Current in this Diameter	% Deviation from FWHM Diameter
4 - 96%	Rise Time	80.	49.2%
8.3 - 91.7%	Rise Time	61.6	16.9%
10 - 90%	Rise Time	56.	8.5%
10.5 - 89.5%	Tangent Line	54.8	6.3%
12 - 88%	FWHM	50.	0
15 - 85%	Rise Time	41.8	-11.9%

B. Noise Measurements

The specimen stage current was amplified with a PAR model 181 current sensitive preamplifier and the output was fed to a Quantech model 304 spectrum analyzer. Discrete data points were taken for several runs through the spectrum from 1 Hz to 5000 Hz. A spectrum with the beam turned off was subtracted from the beam noise spectrum to correct for background. These data were analyzed with a computer and integrated to obtain the final overall noise percentage.

Two points are worth noting with respect to noise spectra taken with an analog spectrum analyzer. First, the equivalent noise bandwidth is not the same as the commonly used 3 dB bandwidth.[7] The bandwidth of an amplifier or tuned circuit is classically defined as

the frequency span between half-power points. The noise bandwidth, Δf, is the frequency span of a rectangularly shaped power gain curve equal in area to the area of the actual power gain versus frequency curve (see Figure 6-3).

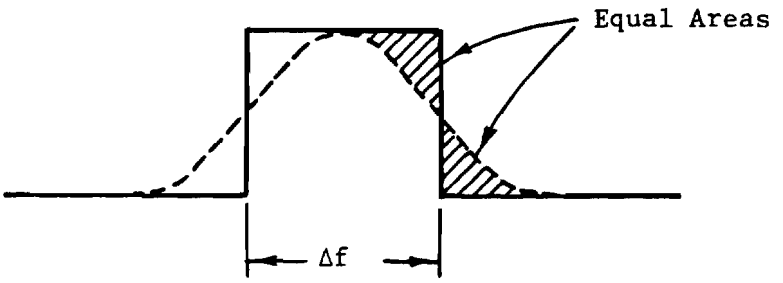

Figure 6-3. Equivalent noise bandwidth.

The second point to mention is that the meters in most of these instruments (including the Quantech 304), while calibrated in terms of rms voltage, are actually average responding meters.[8] Thus, the calibration is only accurate for sine waves, where the average is 0.636 of the peak and the rms is 0.707 of the peak. The rms scale on the meter therefore reads 0.707/0.636 = 1.11 times the voltage measured. Gaussian noise has an average value of 0.798 of rms. The average responding meter indicates 1.11 times higher, so it reads 1.11 × 0.798 = 0.885 of the true rms value. So the reading on the meter must be multiplied by 1/0.885 = 1.13 for an accurate rms reading of Gaussian noise. Other factors to consider when using an analog meter for noise measurement are meter crest factor and bandwidth. These are treated in detail in a book on low-noise electronic design.[7] The most reliable way to measure noise with a meter of

unknown response is to use a calibrated noise source, not a sine wave source, to determine the meter calibration.

More recent noise measurements were done with a Hewlett-Packard 5420A Digital Signal Analyzer. This instrument is capable not only of measuring the noise power spectrum from .0005 Hz to 25 kHz, but also of doing cross spectra between two signals. It was used in the latter mode to determine the coherence between the total (anode) current I_t and the probe (specimen) current I_p. By connecting the analyzer directly to the specimen stage to bypass the preamplifier (which had a DC to 5 kHz response), an attempt was made to follow the high frequency noise spectrum out to 25 kHz. This was not possible because the 1 Megohm input impedance of the analyzer picked up too much background signal. The experimental setup to measure the power spectra and coherence function is shown in Figure 6-4.

The only reason that the 10 μF coupling capacitor was used in the I_t measuring circuit is that one channel of the 5420A analyzer would not switch to the AC coupled mode (a defect in the instrument). In the DC coupled mode, the steady state component of I_t overloaded the input of the analyzer. Measurements involving I_t are therefore not accurate at very low frequencies, on the order of 0.1 Hz and below.

Additionally, in the AC coupled mode, the internal input coupling capacitors limit the low frequency capability to approximately 0.5 Hz, so measurements below this frequency, excepting the coherence function, are not absolutely accurate.

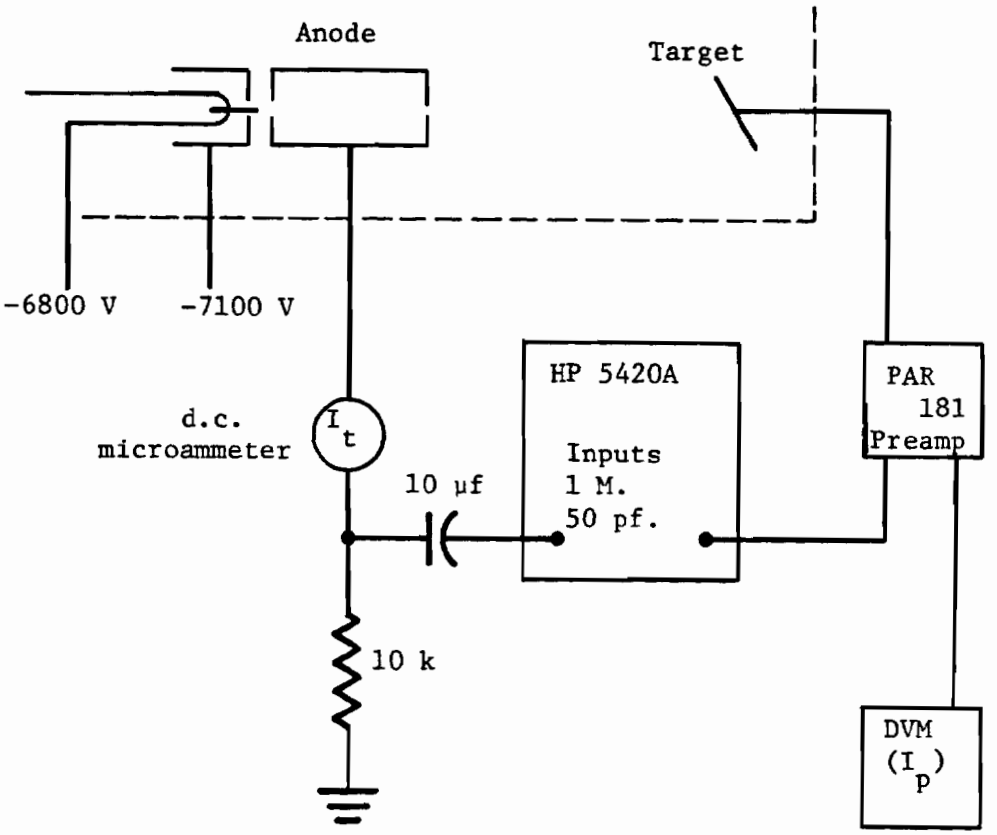

Figure 6-4. Noise spectrum measurement setup.

Several measurement capabilities of the Digital Signal Analyzer were used to analyze the TFE emission noise. The following definitions of the measurements are given for reference.[9] The linear spectrum, $S_x(f)$, is the Fourier transform of the input voltage signal, x(t).

Channel 1 $S_x(f) = F\ x(t)$

Channel 2 $S_y(f) = F\ y(t)$.

The auto power spectrum is the magnitude squared of the linear spectrum,

$$G_{xx}(f) = S_x(f) \cdot S_x(f)^*$$

where * is the complex conjugate. The cross power spectrum is a measure of the mutual power between two signals at each frequency in the analysis band. It is defined as:

$$G_{yx}(f) = S_y(f) \cdot S_x(f)^*.$$

Both magnitude and phase information are contained in this measurement, the phase being the relative phase between the two signals. The coherence function is a measure of the degree of causality between a system input and output. It is defined as:

$$\gamma^2(f) = \frac{\overline{G_{yx}(f) \cdot G_{yx}(f)^*}}{\overline{G_{xx}(f)} \cdot \overline{G_{yy}(f)}} \quad , \quad 0 \leq \gamma^2 \leq 1$$

where $\overline{}$ denotes an average.

The cross power spectrum may have a high value simply because both S_y and S_x happen to be large in a certain frequency interval, not because there is any causal connection between x(t) and y(t). By normalizing the cross power spectrum to the individual power spectra, the coherence function removes this ambiguity in determining causality. If a causal connection is established by means of the coherence function, then the phase of that causality can be

determined by the cross spectrum. The analyzer also had the capability of plotting an amplitude histogram (probability density of amplitude values). For random noise, this plot should be a Gaussian or normal distribution.

C. Auger Measurements

Auger spectra were taken in the standard dN/dE mode. A fixed beam Auger system (PHI 10-155 optics) with a thermionic electron gun mounted coaxially inside a CMA was available for making a comparison of the S/N ratio. This system used a larger CMA with a focus approximately 0.25 in. from the end of the analyzer, in comparison to the CMA in the field emission system which had a focus 0.1 in. from the end of the analyzer.

Auger elemental scans were made by feeding the output of the lock-in amplifier through a variable attenuator to the Z axis input of a Tektronix 605 storage monitor. The X and Y axes were fed with the proper deflection voltages to form a raster and a stored scan was made. The monitor was photographed after the scan and the Auger system was reset to another energy peak. By adjusting the variable attenuator and the lock-in output zero adjust, the z axis voltage window for a stored trace on the 605 could be set above the noise and so that the highest peak occurring in the field of view would not saturate the storage screen (which would smear the image). A test scan was in progress while these adjustments were being made.

REFERENCES

1. D. C. Joy, Seventh Annual Scanning Electron Microscopy Symposium. (IITRI, 1974), page 328.
2. J. D. Verhoeven and E. D. Gibson, J. Phys. E, 9, 65 (1976).
3. James F. Norton, General Electric Corp., private communication.
4. K. C. A. Smith, Ph.D. Dissertation, Cambridge (1956).
5. T. Groves, D. L. Hammond and H. Kuo, J. Vac. Sci. Technol. 16, 1680 (1979).
6. M. Abramowitz and I. Stegun, "Handbook of Mathematical Functions," (Dover, 1972), page 966.
7. C. D. Motchenbacher and F. C. Fitchen, "Low-Noise Electronic Design," (Wiley, 1973), page 13.
8. Ibid., page 299.
9. "Digital Signal Analysis: Time and Frequency Domain Measurements," Hewlett Packard Application Note 240-0.

CHAPTER 7

RESULTS AND DISCUSSION

A. Beam Diameter

The relevant lens parameters are: f_1 = 63 mm; C_{s_1} = 139 mm; C_{c_1} = 53.7 mm; f_2 = 139 mm; C_{s_2} = 3000 mm; C_{c_2} = 133 mm; M = 2.2; α = 0.006 rad; Ω = 0.113 msr. The effective beam aperture seen by the emitter was .006 rad half angle. Spot size data was taken for two different emitters. The "emitter voltage" (V_Ω) was taken to be that required to obtain 1.0 mA/sr at a temperature of 1800 K. The higher voltage emitter, at 12000 V, produced a limited amount of data, as far as spot size is concerned. Problems occurred with the high voltage wiring since the system had not originally been designed to operate at this voltage.

In Table 7-1 the experimental and calculated beam diameters for the "12000 V emitter" are given. Beam currents were varied by changing the beam voltage from 8.5 to 12.0 kV. An assumed Gaussian source diameter of 150 Å[1,2] was included in the calculations. Contributions of the spherical (d_s) and chromatic (d_c) aberration disks of both the upper (subscript 1) and lower (subscript 2) lenses are also indicated. The value of the energy spread ΔV is known to increase with source angular intensity (I_p/Ω);[3,4] thus, experimental values for ΔV obtained previously from a lower voltage emitter were used.[4] If we take the experimentally determined spot size, subtract in

TABLE 7-1

EXPERIMENTAL AND PREDICTED GUN OPERATING PARAMETERS FOR 12000 V EMITTER

(Values of d in μm)

I_p(na)	T(K)	V(kV)	ΔV(eV)*	I_p/Ω $\frac{mA}{sr}$	d_{c_1}	d_{s_1}	d_{c_2}	d_{s_2}	d(calc)	d(exp)	ΔV(eV)**
40	1800	8.5	1.08	0.35	.091	.033	.046	.030	.116	.108	0.99
60	1800	9.5	1.32	0.53	.099	.033	.050	.030	.125	.095	0.92
66	1850	10.0	1.40	0.58	.100	.033	.051	.030	.125	.100	1.05
98	1850	11.5	1.79	0.87	.110	.033	.056	.030	.136	.105	1.28
110	1850	12.0	1.93	0.97	.114	.033	.058	.030	.140	.104	1.32

*Estimated values from data on a smaller radius emitter.

**Calculated from experimental spot diameter.

quadrature the spherical aberration contributions, we can then infer the beam energy spread. This is tabulated in the last column. The three different methods of spot size measurement agreed within ± 0.02 μm. Typical SEM images of two different specimens are shown in Figure 7-1.

The results show that the experimental values of d achieved between 40 and 110 nA beam current and with M = 2.2 are all of the order of 0.10 μm.

The electron beam broadening effect as computed by Groves, et al.[5] can be estimated for this optical column as follows:

$$d_b = C_b \frac{I_p}{\alpha'}$$

where

d_b = blur diameter due to broadening

C_b = broadening coefficient

I_p = beam current

α' = beam convergence semi-angle at image plane

$= \frac{\alpha}{M} = \frac{.006}{2.2}$ for our system.

For a 25 cm column length, C_b = .164 cm/A. Thus, for our system

$$d_b = (.164)\frac{(.1\ \mu A)}{(.0027)} = 6 \cdot 10^{-6}\ \text{cm} = 0.06\ \mu\text{m}.$$

Since this is the diameter defined by the "tangent line" method, it corresponds to a FWHM diameter of .06/1.06 = .057 μm. When this is added in quadrature with the nominal 0.1 μm spot diameter, the result

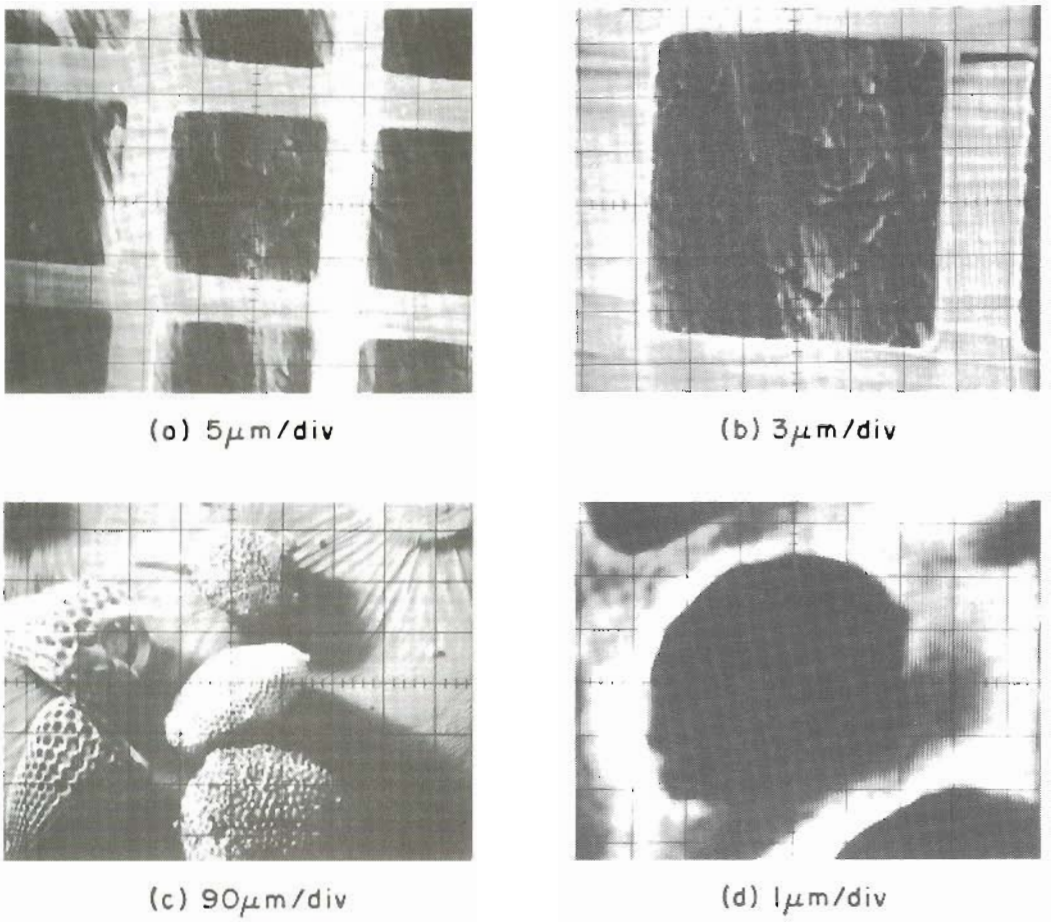

Figure 7-1. SEM images from scanning Auger microprobe.

(a) and (b) -- 5 μm wires.

(c) and (d) -- Gold-coated radiolaria.

is approximately 0.115 μm. This effect has therefore increased the diameter by only 150 Å. Since the error in any measurement is on the order of ± 100 Å, to see this effect, we would have to take the beam current up to 1 μA or so. The present measurements taken on this system do not go beyond 0.11 μA.

The above calculation can only be considered an estimate, since the broadening coefficient C_b was calculated for a case of zero initial energy spread. The actual procedure used in the paper[5] was to assume an initial energy spread corresponding to the angular intensity at the source and incorporate both lateral space charge broadening and longitudinal "Boersch" effect and its effect due to the chromatic aberration of the particular lens system used into the d_b value. The data were not provided in the paper for calculating C_b for a system with an initial energy spread and a given value of C_c.

Because of the large value of dI/dT for the low work function Zr/W <100> TF source, the beam current can also be varied by changing the emitter temperature while keeping the beam voltage constant. However, at low temperatures, gas adsorption on the emitter becomes an increasing problem in low (e.g., 10^{-8} torr) vacuum environment. More extensive data were accumulated for the low voltage (9000 V) emitter by varying beam current by means of temperature at several selected voltages. Figures 7-2 and 7-3 show typical experimental variation of beam current with voltage and temperature. To some extent the grid voltage can also be used to vary both the beam and

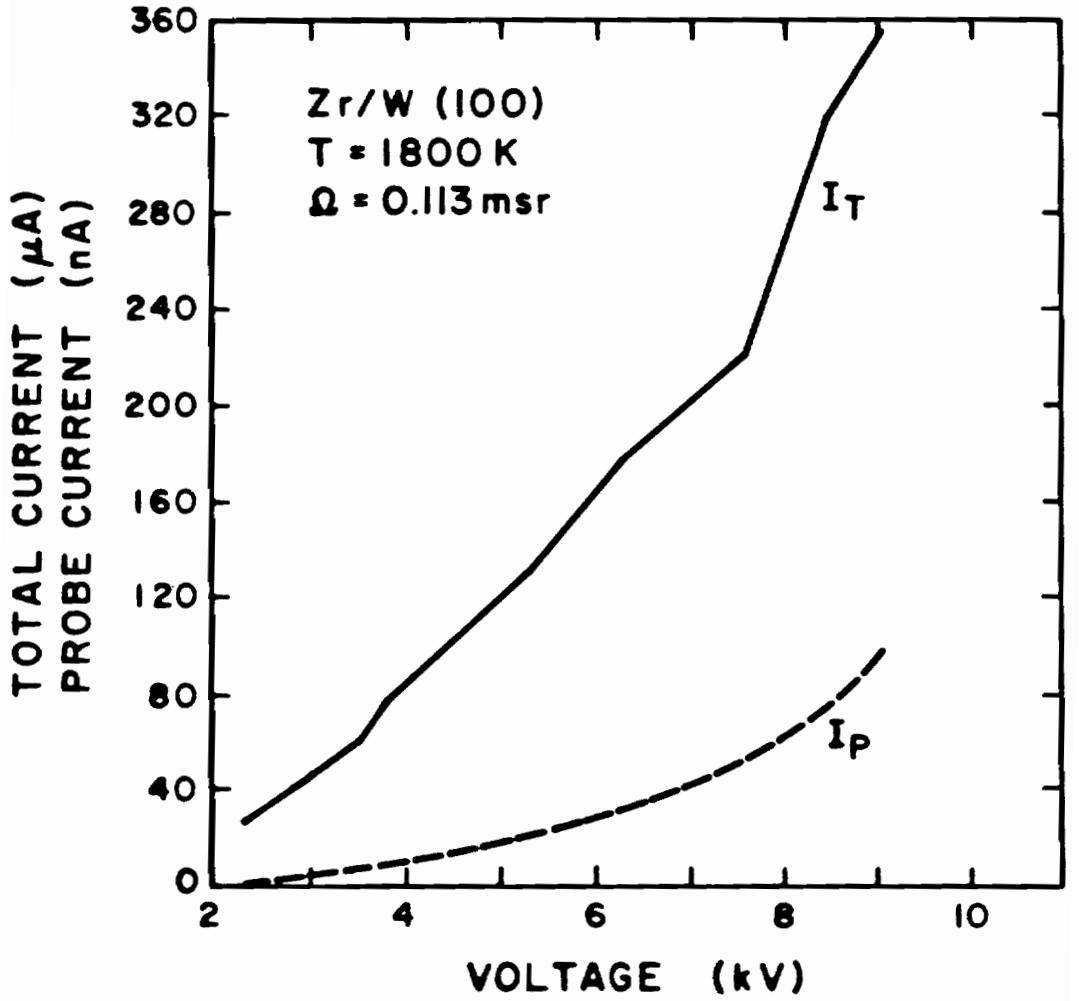

Figure 7-2. I-V characteristic curves.

V = 9.0 kV, V_Ω = 9000 V.

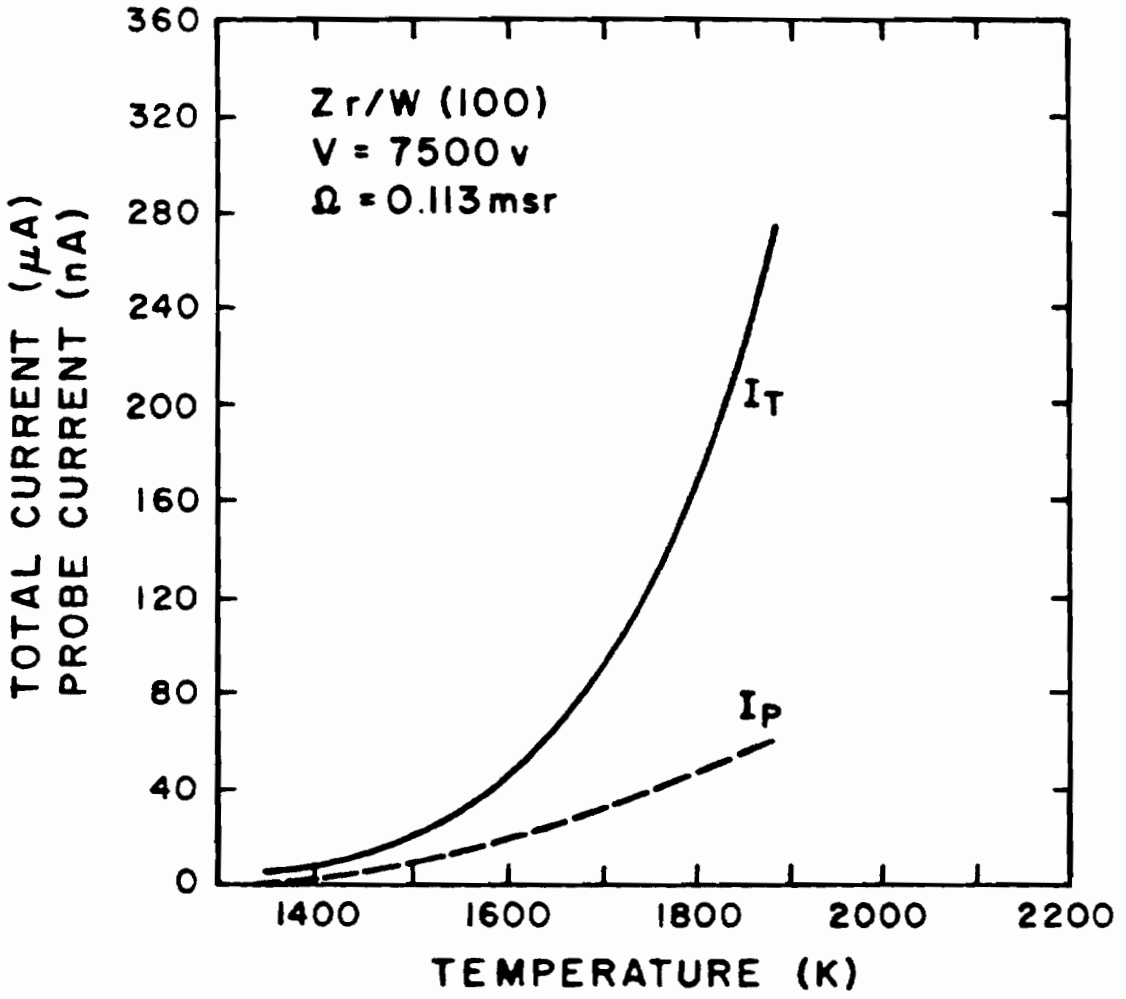

Figure 7-3. Current vs. temperature characteristic curves.

V = 9.0 kV, V_Ω = 9000 V.

total currents at constant beam voltage. This is shown in Figure 7-4.

By plotting beam size vs. inverse volts for the low voltage emitter, the energy spread at a given angular intensity can be inferred from the slope of the lines as shown in Figure 7-5. It would seem that the higher voltage emitter starts out with a larger energy spread than the low voltage emitter, and at high angular intensities the low voltage emitter's energy spread becomes greater. However, if one looks at the size of the error bars, it appears that in order to say any more about this effect a more sophisticated experimental setup would be required to reduce the error to < 50 A.

Figure 7-6 shows a comparison of 8.5 and 12.0 kV emitters in a beam diameter vs. beam current plot. The voltage was varied in both cases to vary the beam current. It can be seen that even though the beam energy spread ΔV increases with current in both cases, its effect on the beam diameter is cancelled for the higher operating voltage, in part due to the greater denominator in the $\Delta V/V$ factor and in part due to less ΔV from a larger radius emitter at a given angular intensity.

A plot of the voltage variability of the 9000 V emitter at a constant 85 nA probe current is shown in Figure 7-7. Temperatures above 1900 K approach the melting temperature of zirconium, while temperatures below approximately 1600 K allow adsorbed gases to build up which after a sufficient time ($\sim$ 1 hour) will "kill" the emission.

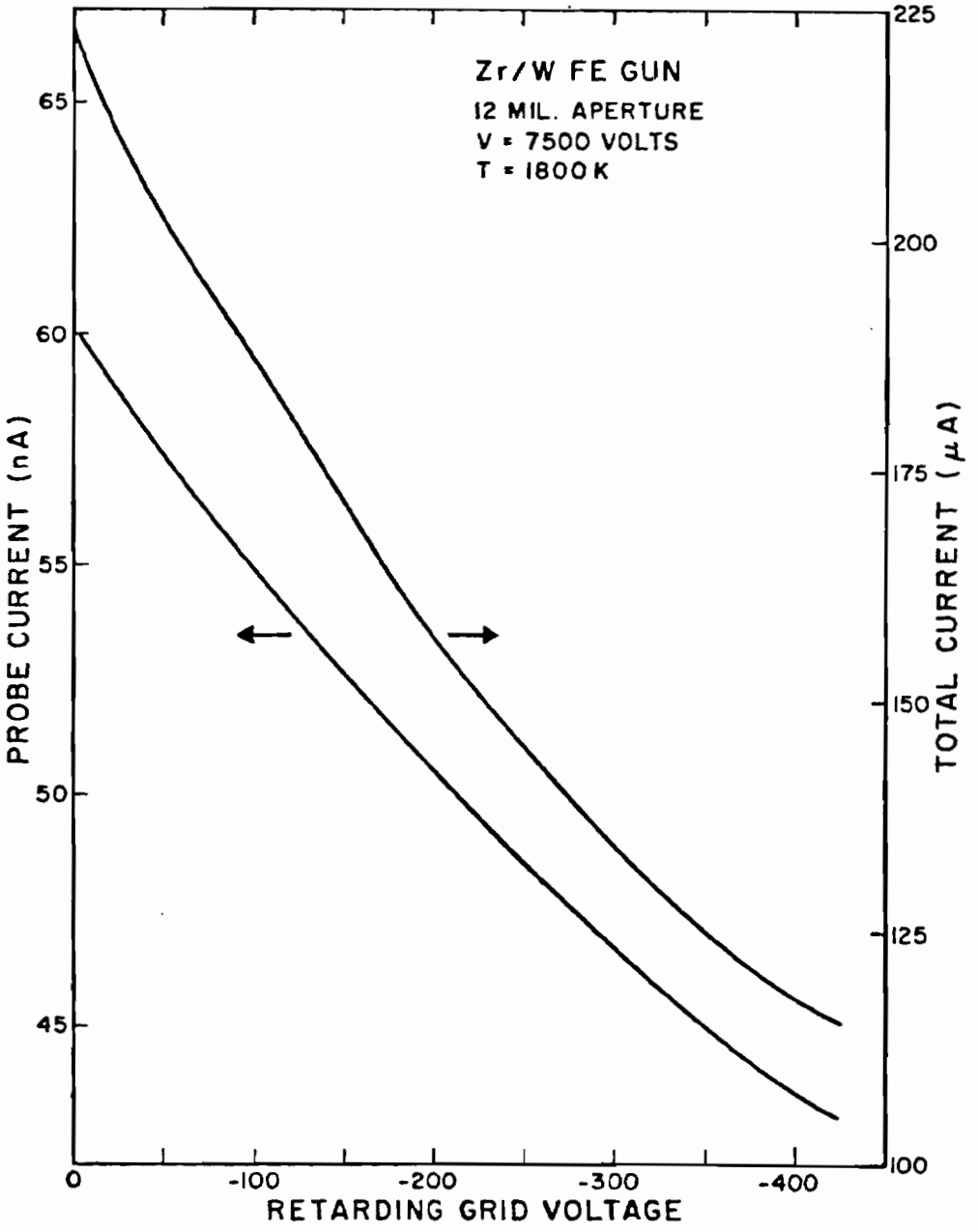

Figure 7-4. Grid control of current.

V = 9.0 kV, V_{Ω} = 9000 V.

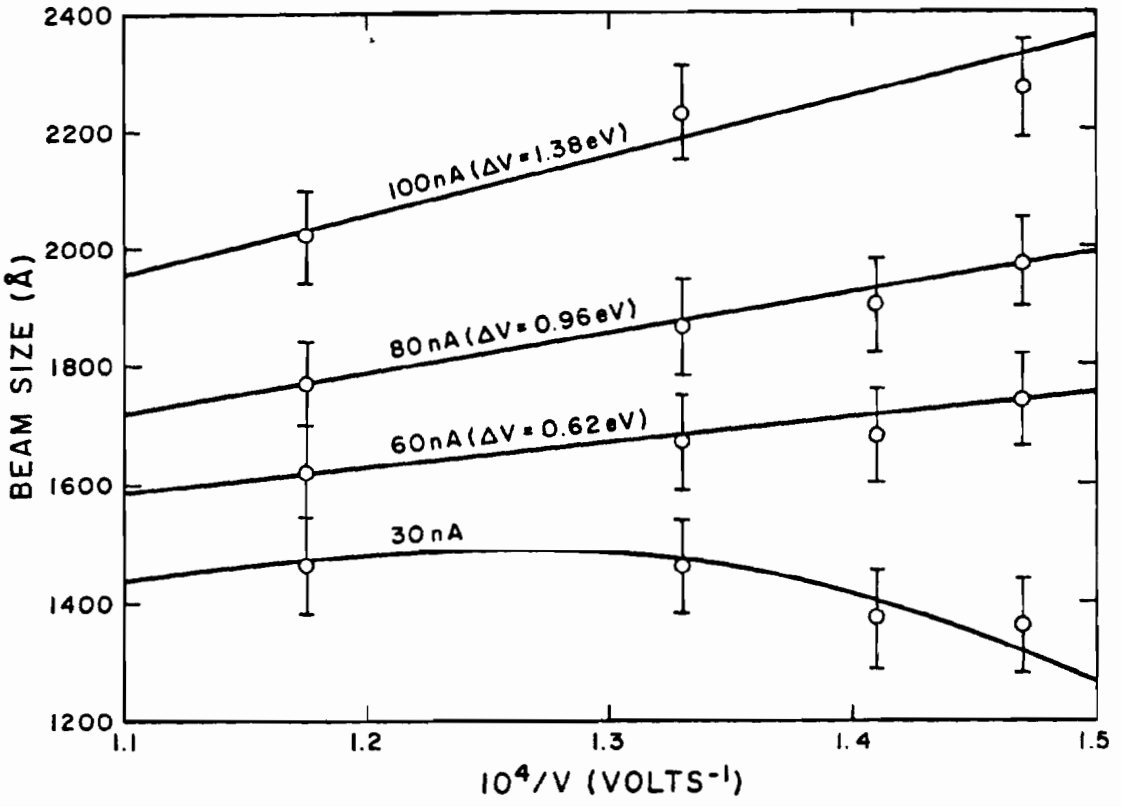

Figure 7-5. Beam size for low voltage emitter.

V = 9.0 kV, V_{Ω} = 9000 V.

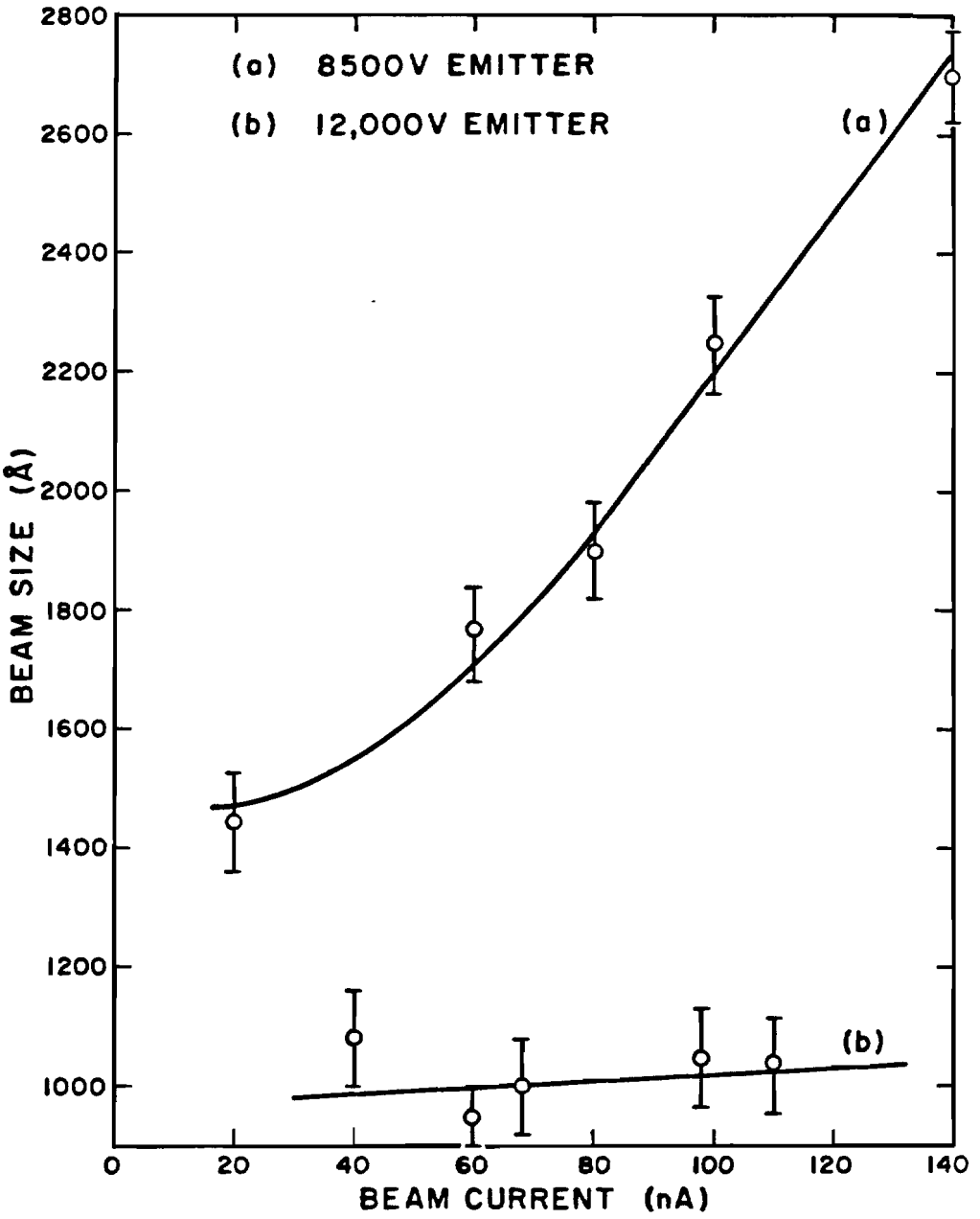

Figure 7-6. Beam diameter vs. beam current for two different emitters.

$V = 9.0$ kV, $V_{\Omega} = 9000$ V.

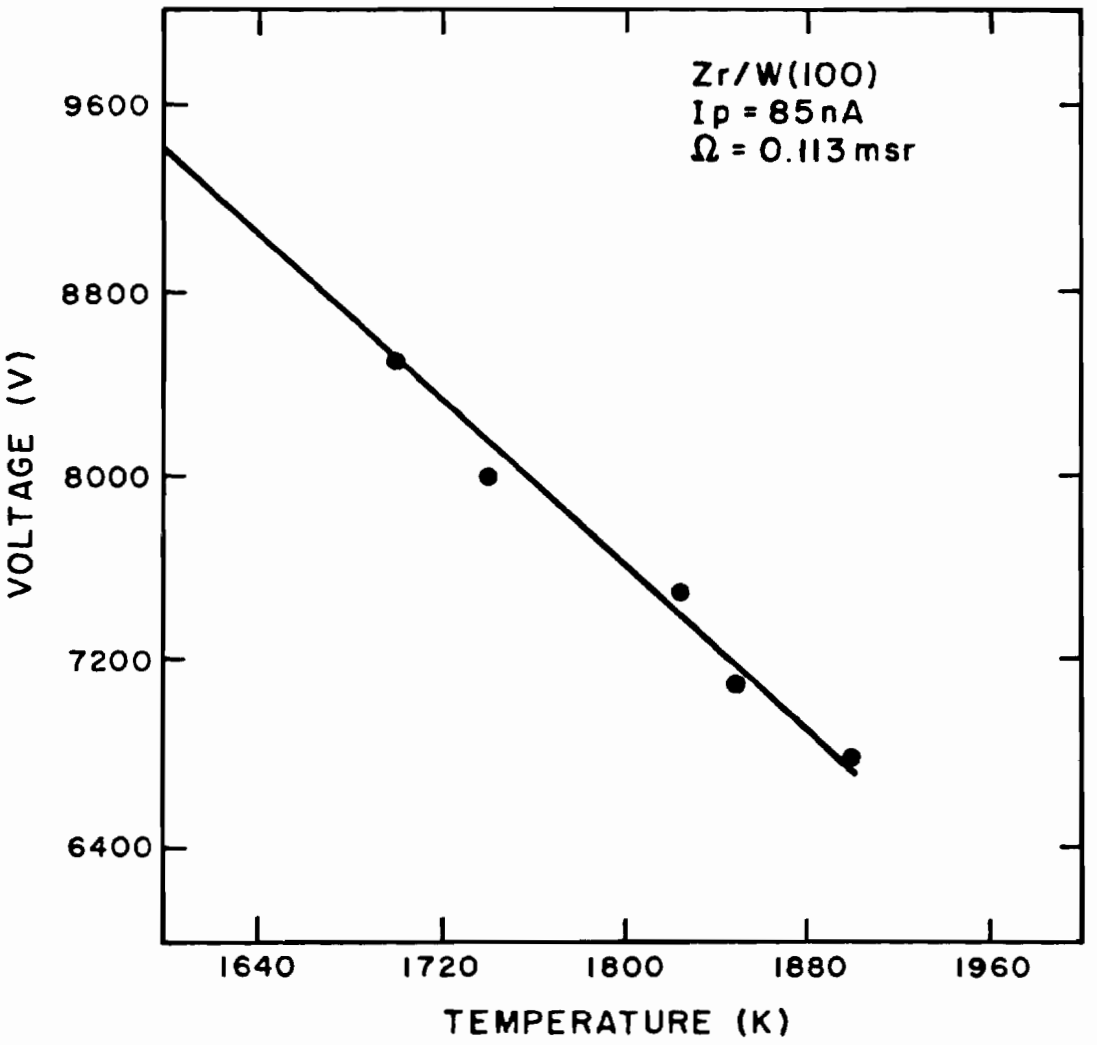

Figure 7-7. Voltage variability with a constant probe current.

V = 9.0 kV, V_{Ω} = 9000 V.

B. Noise Data

The shot noise level for a probe current of 30 nA is 9.6×10^{-27} A^2sec or 98 fA/$\sqrt{Hz}$. The noise spectrum for a 9100 V emitter as measured on the Quantech 304 is shown in Figure 7-8. As mentioned in the experimental procedure section, this instrument is calibrated in terms of a sine wave reference signal. To correct this spectrum for a Gaussian noise signal, the graph should be moved up by a factor of $(1.13)^2 = 1.28$. The total integrated noise from 1 Hz to 5000 Hz is 0.23% uncorrected, or 0.26% corrected.

Note that the high frequency end of the spectrum falls of as 1/f (-3 dB/octave). Assuming that this behavior continues all the way down to shot noise level, we can determine the frequency at which this occurs and the additional contribution that this extrapolated high frequency portion would make to the total rms noise percentage. The frequency at which the extrapolated noise level would reach shot noise is 190.5 kHz. The additional rms noise in the > 5 kHz region is 0.27%. Therefore, the total rms noise percentage would be 0.53%, if one can assume that the 1/f falloff continues all the way to shot noise.

Since the analog spectrum analyzer indicated a large low frequency noise component (< 2 Hz), a complete spectrum was run on the digital spectrum analyzer down to 5×10^{-4} Hz. The data scatter increased for the extremely long data runs; the lowest frequency range required 17 hours to accumulate samples required for 20

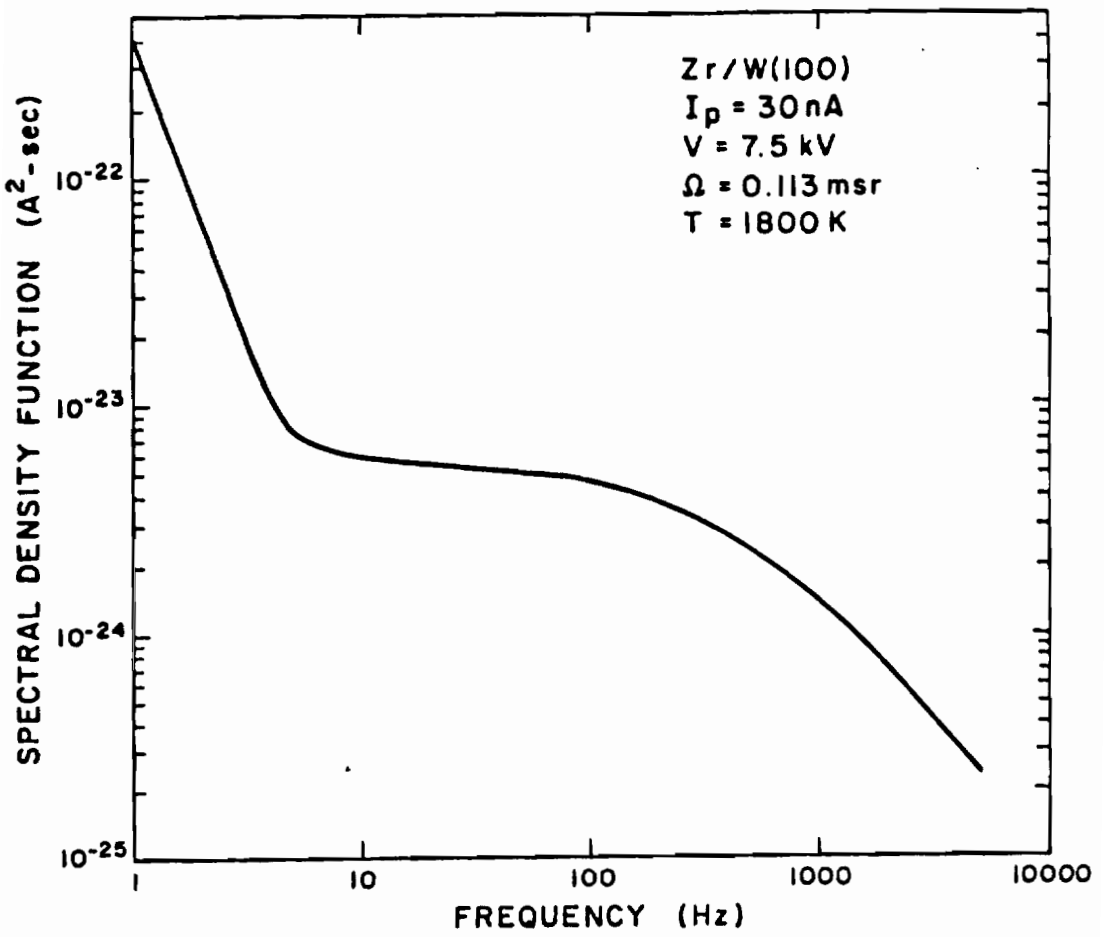

Figure 7-8. Noise spectral density.

V = 9.1 kV, V_Ω = 9100 V.

averages. Most of the digital spectra were the results of 60 to 100 averages. Figure 7-9 shows the results of the entire probe current spectrum for I_p = 50 nA. Note that the emitter used in this experiment was yet another radius, since V_Ω = 7500 V. Also note that the falloff in noise power below 0.5 Hz is probably due to input coupling capacitors in the spectrum analyzer.

A clue to the nature of the low frequency (< 2 Hz) noise power was seen in a cross spectrum done in the 0.1 to 20 Hz range. The relative phase between the probe and total noise currents was random for frequencies above 2.1 Hz but the noise currents abruptly fell into phase (0°, taking into account the 180° shift from the preamp and the small phase shift due to the 10 μF coupling capacitor) at 2.1 Hz and below.

The coherence function between the probe and total currents (Figure 7-10) shows the same behavior: an essentially uncorrelated relationship > 2 Hz and almost complete correlation < 2 Hz. If the individual I_p and I_t noise power spectra are multiplied by the coherence function, the coherent noise power in each spectrum can be plotted, as in Figure 7-11.

An attempt was made to effectively change the size of the aperture by placing the upper magnetic lens gap at the position of the emitter and pulling in the divergent electron trajectories by magnetic focusing before the beam hit the aperture, thereby effectively increasing the aperture. The results are as follows:

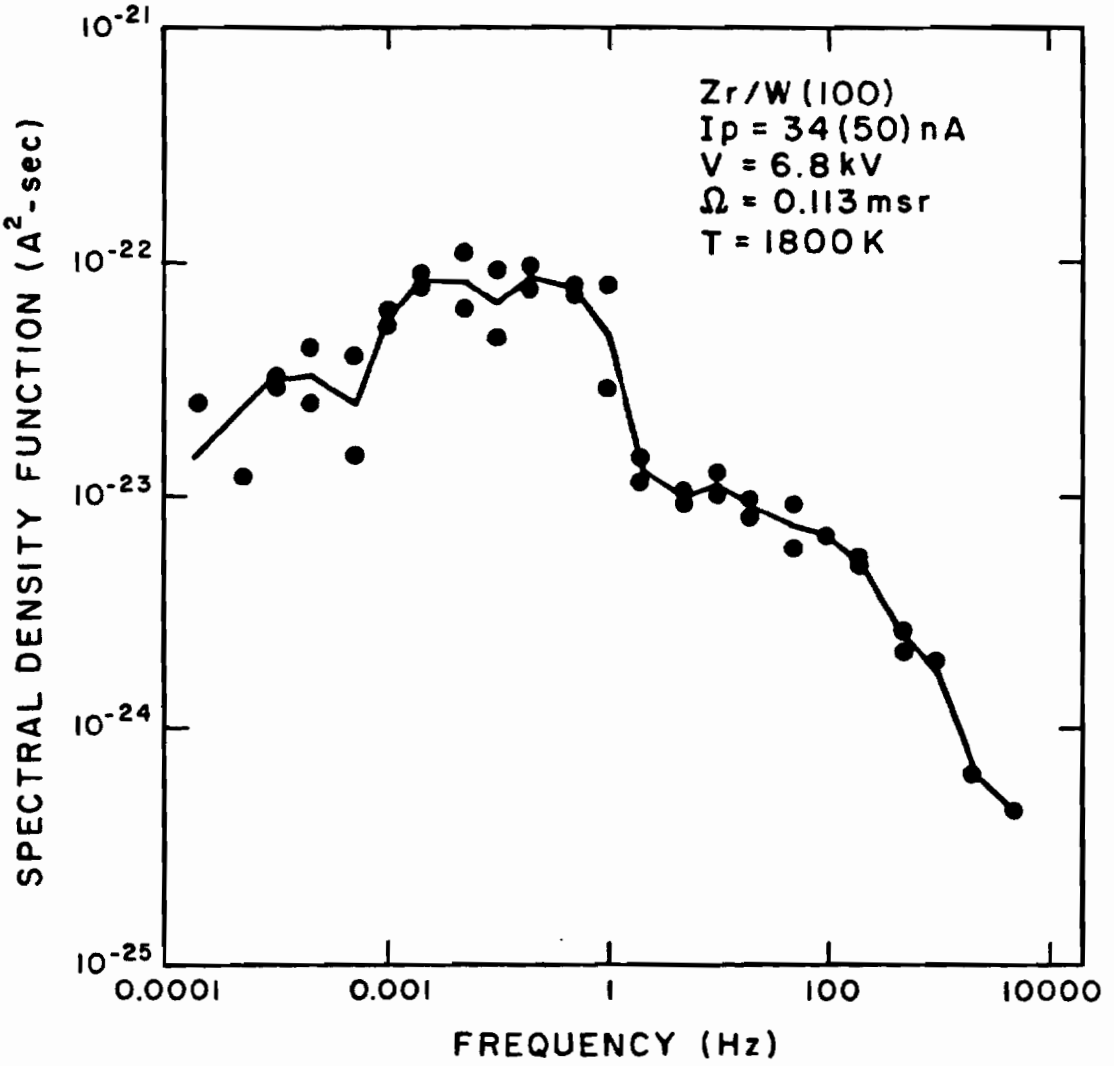

Figure 7-9. Noise spectral density.

Ip = 34 nA unbiased stage
Ip = 50 nA biased stage

Spectrum taken with unbiased stage.

V = 7.5 kV, V_{Ω} = 7500 V.

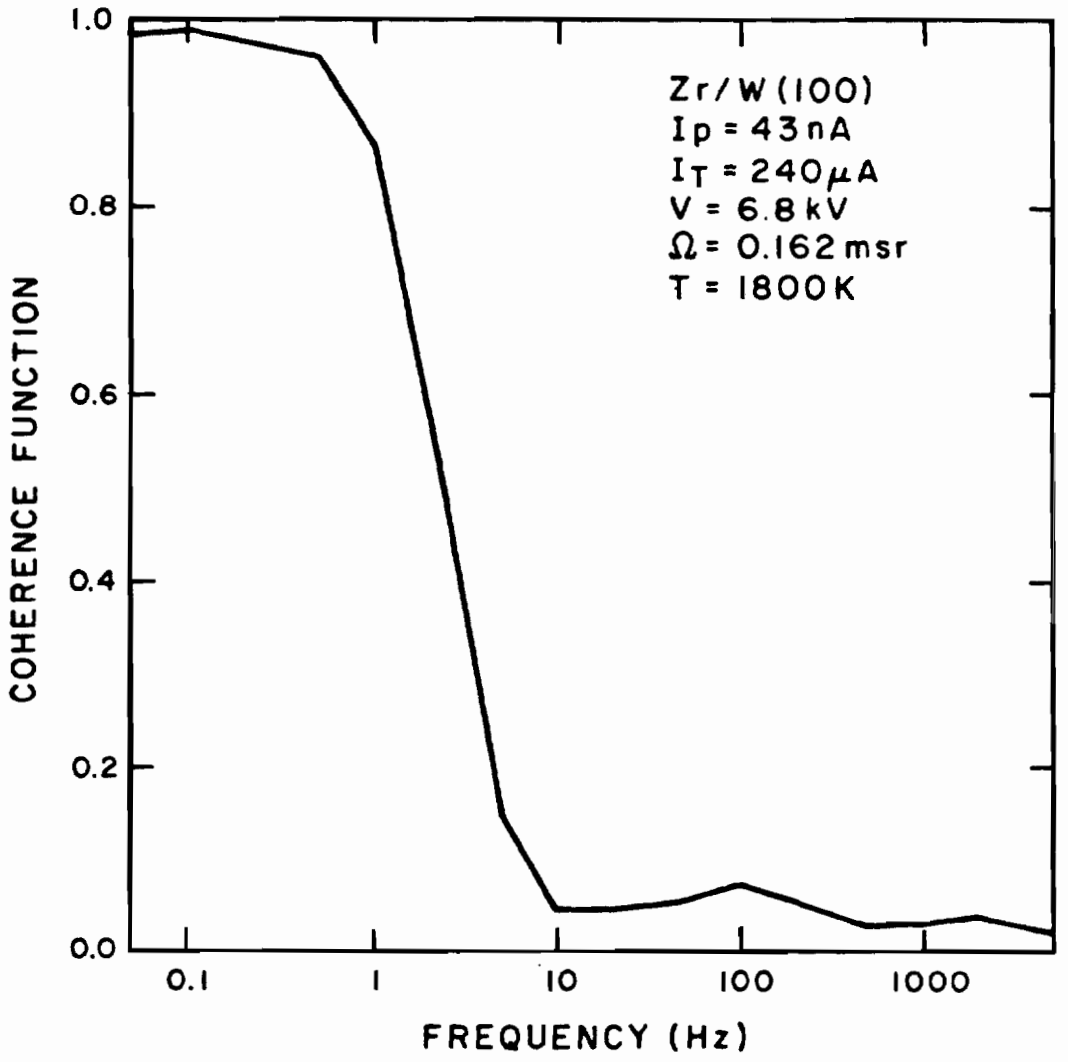

Figure 7-10. Coherence function.

V = 7.5 kV, V_Ω = 7500 V.

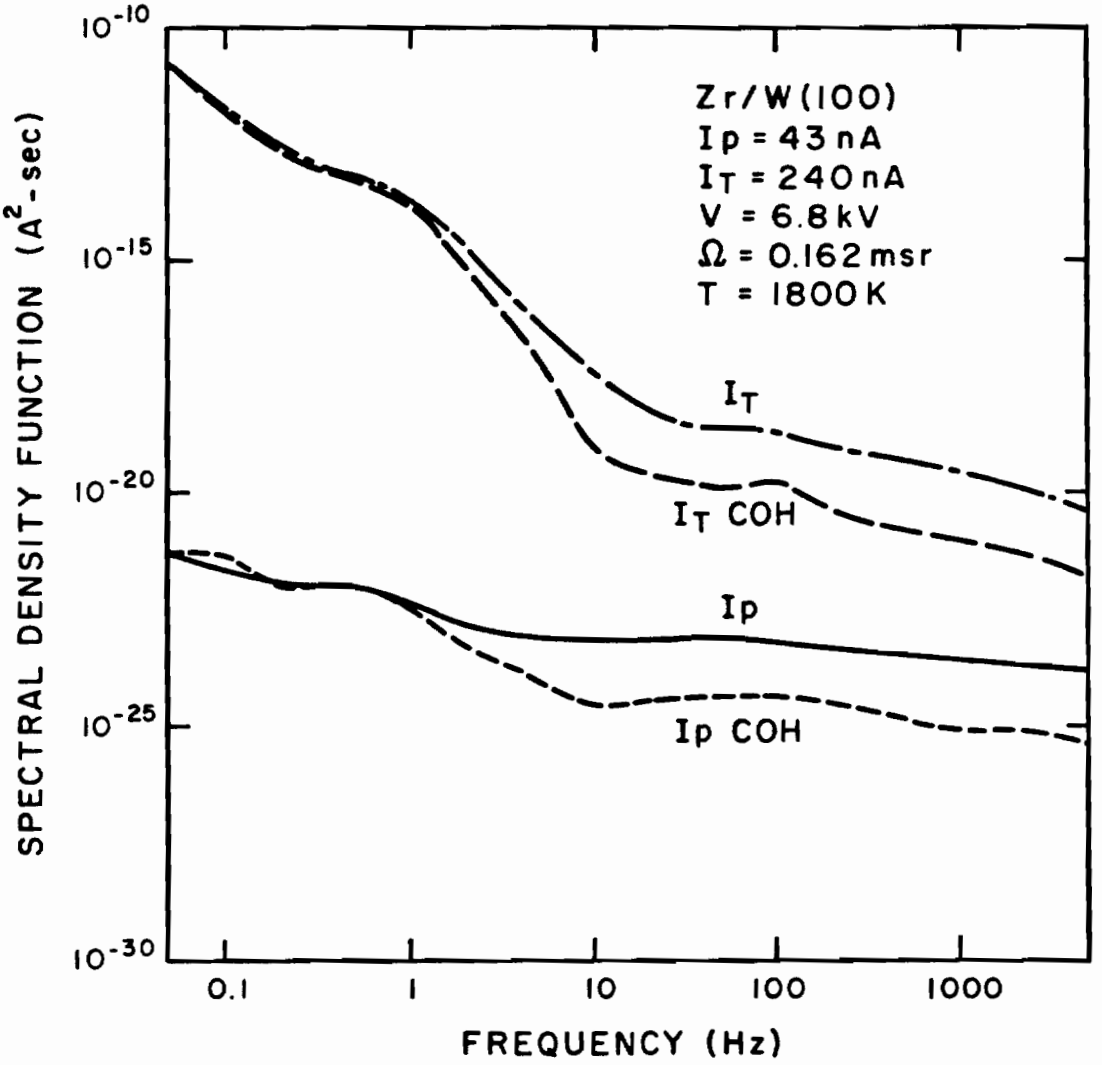

Figure 7-11. Noise spectral density.

Ip = 43 nA unbiased stage

V = 7.5 kV, V_Ω = 7500 V.

Figure 7-12: Variable aperture noise spectra for I_p = 110, 385, 1930 nA.

Figure 7-13: Same spectra with results normalized to the 110 nA spectrum.

Figure 7-14: Log ratio of normalized spectra.

Figure 7-15: Linear ratio of normalized spectra.

The last two figures are different plots of the same results, namely that the high frequency components of the noise spectra (> 2 Hz) decrease (percentagewise) as the aperture is opened up. However, the figure also shows that the low frequency, coherent component of noise current increases with increasing aperture.

Figure 7-16 plots the total rms noise current percentage over a band 10 Hz $\leqslant$ f $\leqslant$ 5 kHz as a function of aperture semi-angle. Figure 7-17 is a replot of this data as a function of aperture solid angle. There are only three points on each of these graphs and the lines are 2nd order polynomial regression fits. Since the noise power integral is relatively insensitive to power below 10 Hz in the spectrum, these plots are unchanged by the inclusion of the low frequency part of the spectrum. The noise in the beam current will decrease with increasing aperture angle, as might be expected since a large emitting area is subtended which produces a better statistical smoothing of the emission fluctuations due to microscopic surface effects.

The low frequency (< 2 Hz) part of the spectrum is possibly a result of random thermal fluctuations which are confined to the low

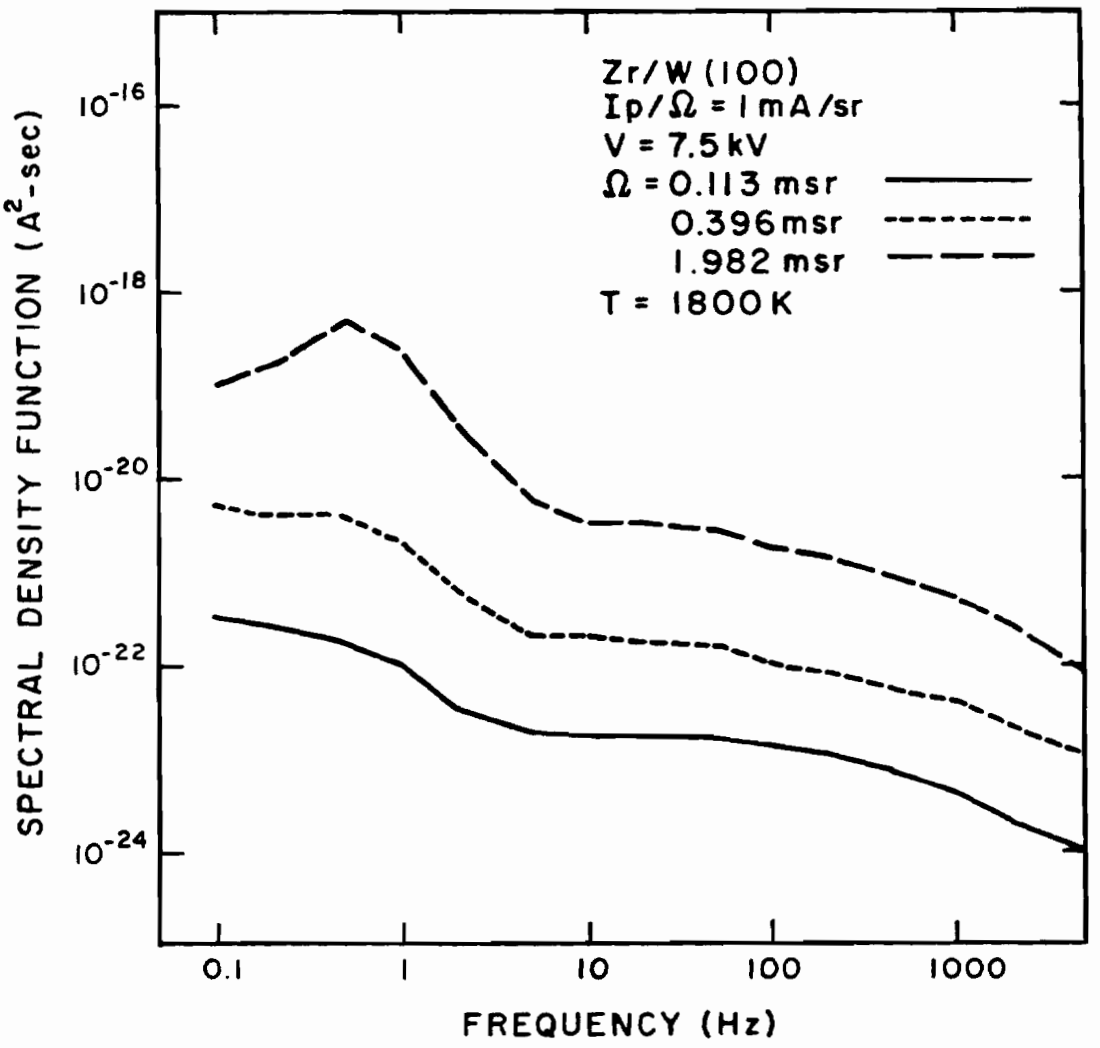

Figure 7-12. Variable aperture noise spectra.

Ω = 0.113 msr, Ip = 57(110) nA, no magnetic focusing
Ω = 0.396 msr, Ip = 200(385) nA, magnetic focusing
Ω = 0.982 msr, Ip = 1000(1930) nA, magnetic focusing

Current Ip given for: no target bias (positive bias).
Ip/Ω referred to biased target.
Noise spectra taken on unbiased target.

V = 7.5 kV, V_{Ω} = 7500 V.

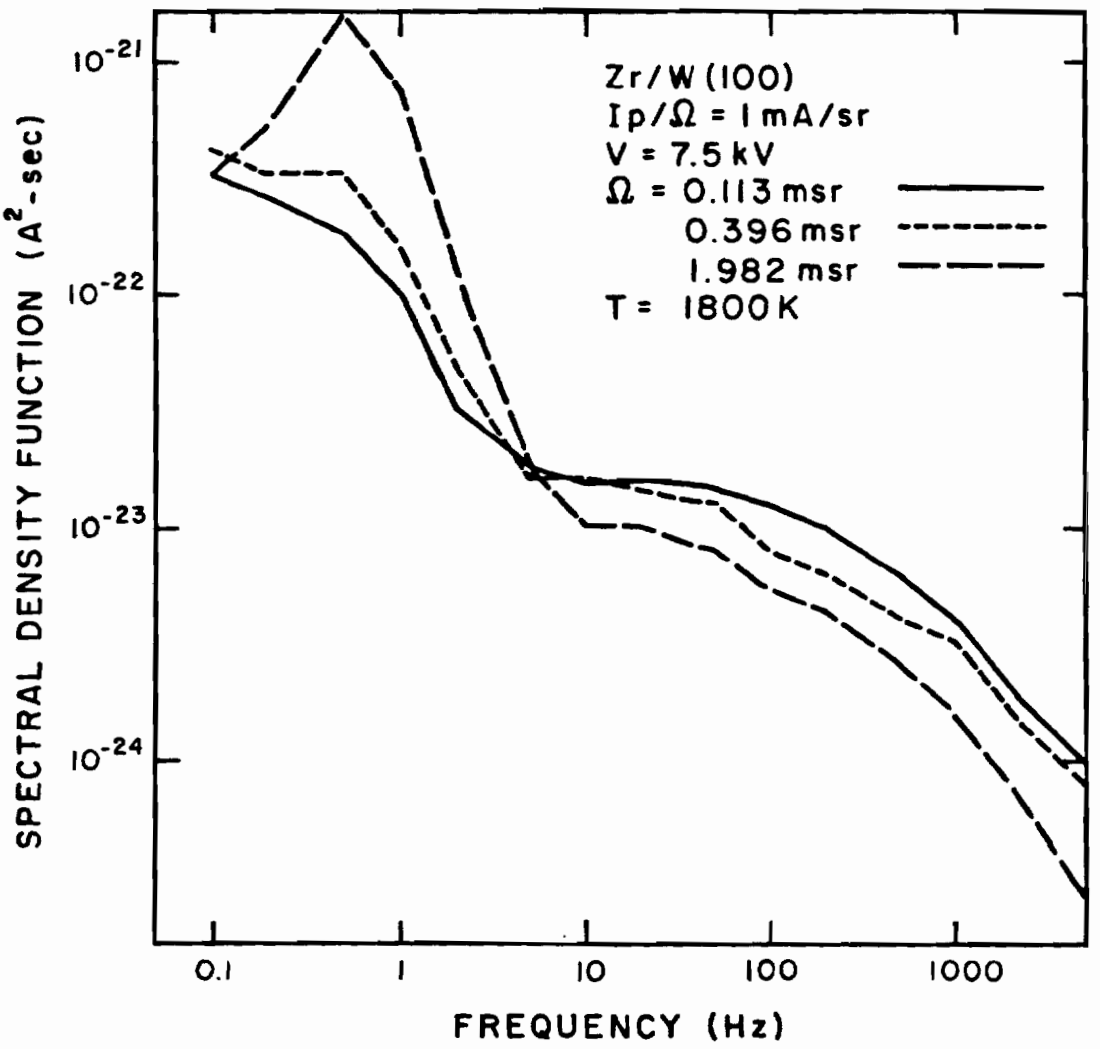

Figure 7-13. Variable aperture noise spectra normalized to 57 nA = Ip.

V = 7.5 kV, V_{Ω} = 7500 V.

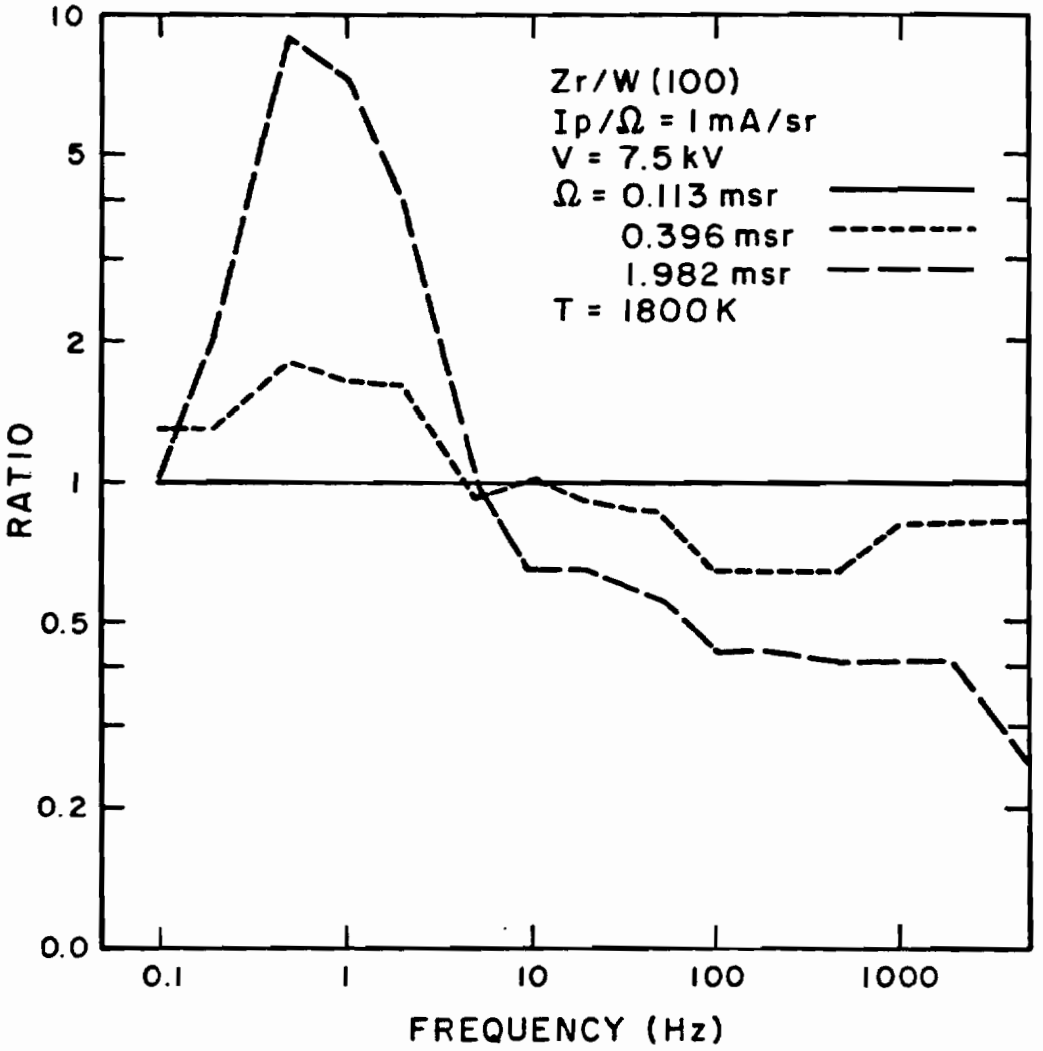

Figure 7-14. Ratio of normalized spectra to the 57 nA spectrum.

V = 7.5 kV, V_{Ω} = 7500 V.

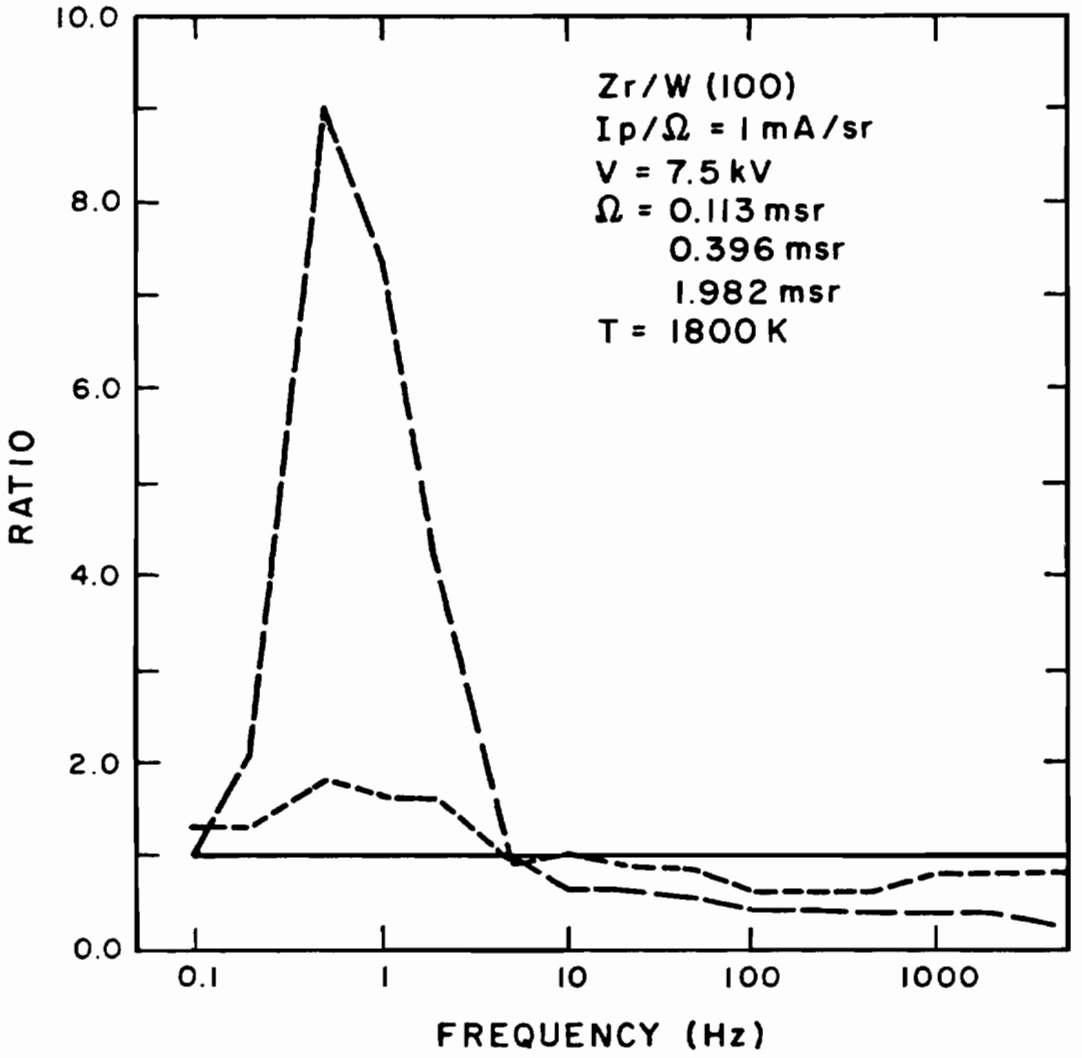

Figure 7-15. Ratio of normalized spectra to the 57 nA spectrum.

(Linear plot)

V = 7.5 kV, V_{Ω} = 7500 V.

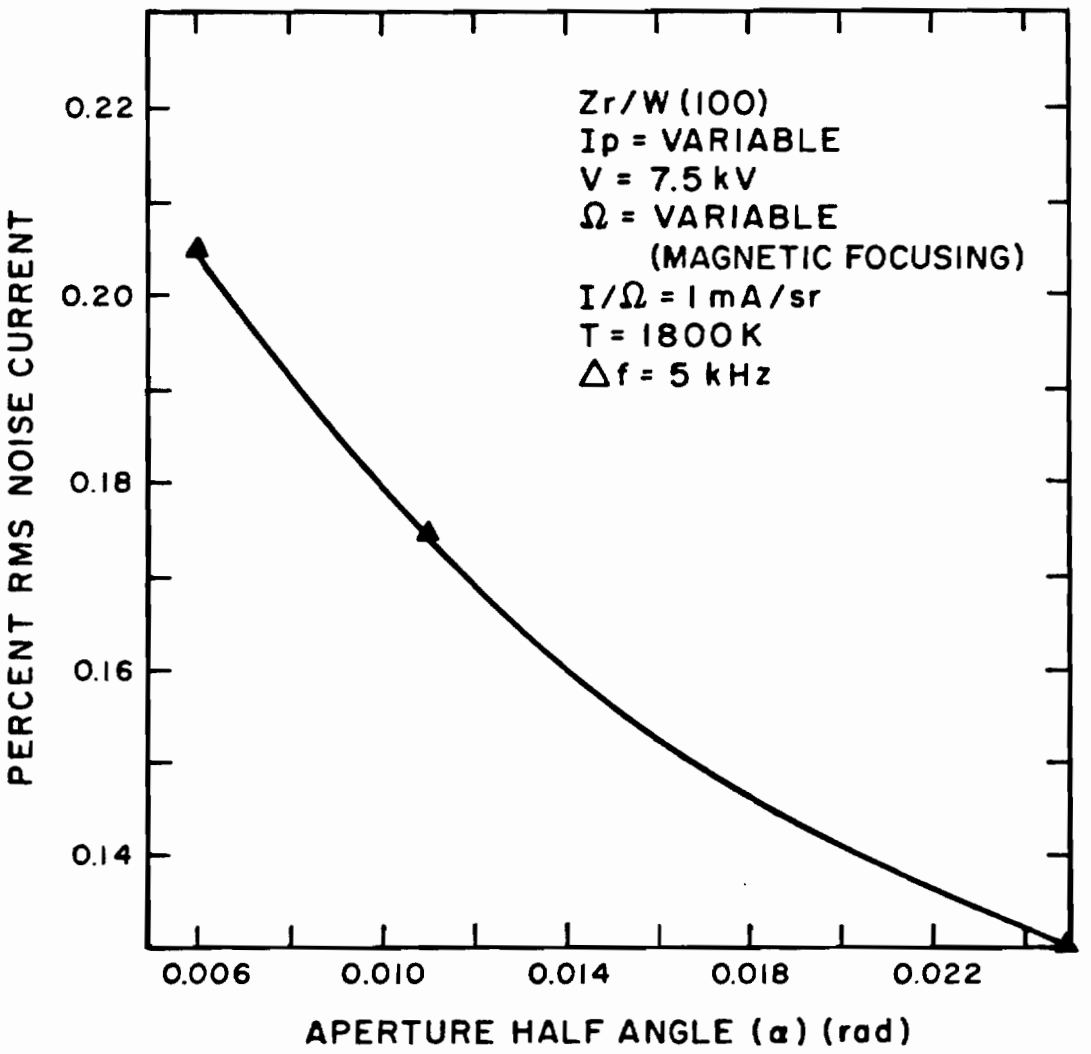

Figure 7-16. RMS noise current vs. aperture half angle.

$V = 7.5$ kV, $V_{\Omega} = 7500$ V.

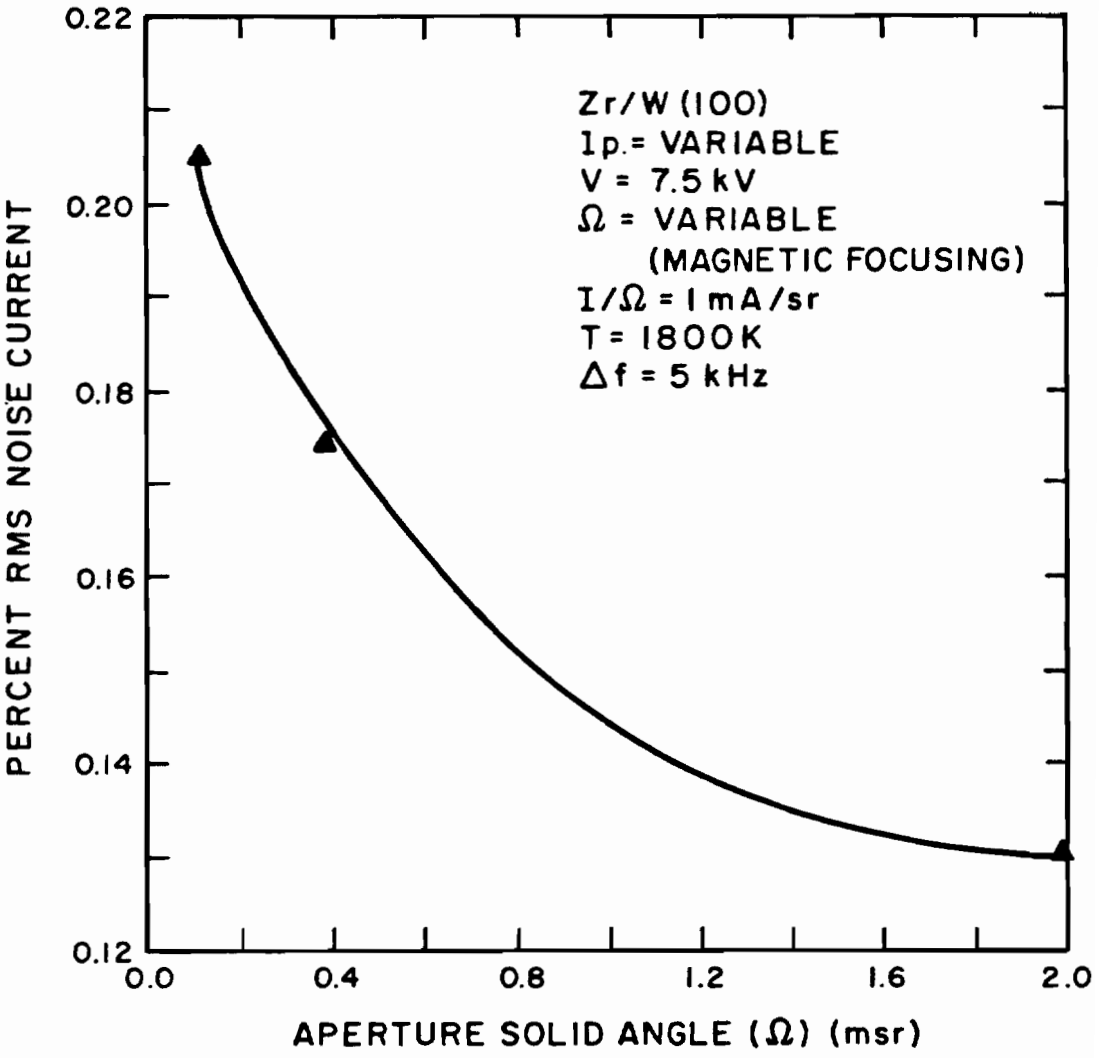

Figure 7-17. RMS noise current vs. aperture solid angle.

V = 7.5 kV, V_{Ω} = 7500 V.

frequencies by the thermal time constant of the tungsten wire. Since the fluctuations are in phase, they apparently cannot be due to a partition effect. A treatment of the emitter and its supporting structure should include resistive heating, conduction, radiation and emission cooling effects and is too complicated to attempt in the present thesis.

Only two amplitude histograms were taken. The conditions for these were: V = 6800 V, I_p = 30 nA, I_t = 240 nA, T = 1800 K, and Δf = 16 Hz (bandwidth of analyzer). The I_p histogram was essentially a Gaussian curve centered on the average value of I_p. The I_t histogram was definitely non-Gaussian. There appeared to be a Gaussian peak imbedded in the I_t distribution which was centered on the average I_t value, but there were significant amplitude probabilities displaced from the average. This is another confirmation that the low frequency domain contains non-random fluctuations. From Figure 7-11, one can see that the low frequency peak in I_p noise is about 2 orders of magnitude greater than the 10 to 100 Hz region. The I_t noise, however, exhibits a low frequency peak 6 or 7 orders of magnitude greater than the 10 to 100 Hz region noise. This large low frequency noise power shows up in the I_t histogram as a non-random component.

C. Auger Data

Auger area maps have been obtained for a barium scandate/tungsten dispenser cathode with good results. Figure 7-18 shows the results of a series of 5 minute elemental scans, along with the SEM images of the

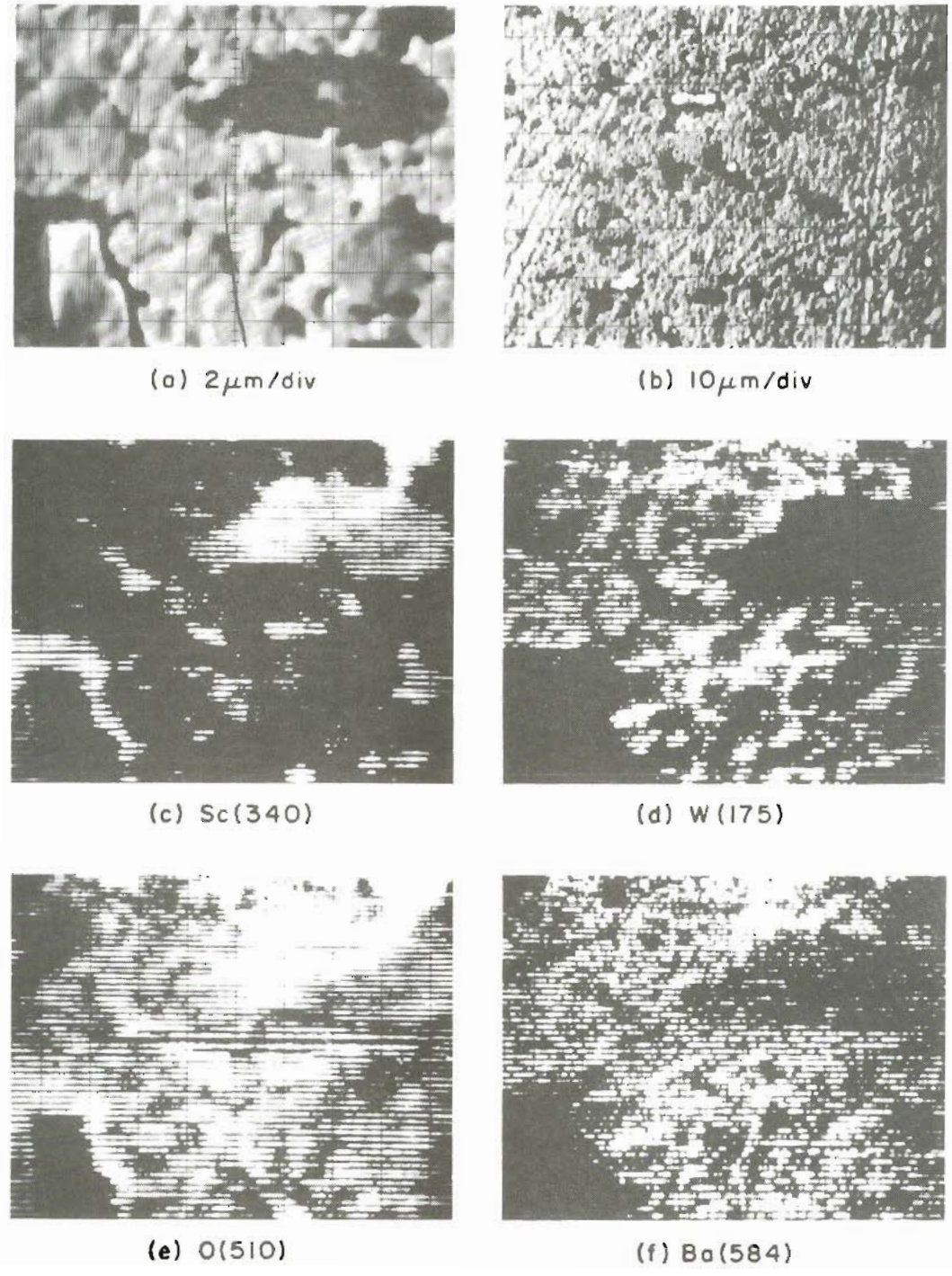

Figure 7-18. Secondary electron images (a) and (b) of a barium scandate/tungsten dispenser cathode. Auger images (c), (d), (e) and (f) correspond to secondary electron image (a).

same area. These were taken with the 12000 V emitter operating at 8500 V, 30 nA. For Auger work the probe current was not increased much above 30 nA to minimize specimen damage. Typical spectra for the barium scandate cathode are shown in Figures 7-19 and 7-20.

The 9000 V emitter was used to do an oxygen scan of the Au-SiO_2 sample after sputter cleaning (Figure 7-21). The amplitude of the oxygen peak permitted a 1 minute high resolution elemental scan. This scan shows shadowing of the Auger electrons from the analyzer due to the right angle geometry between the primary beam and the CMA axis. It also shows an "edge" to the gold pattern, apparently due to the forward scattered primaries from the edge of the gold.

An LaB_6 planar cathode specimen was thermally cleaned and the 179 eV Boron peak was used to demonstrate that the Auger noise level is essentially shot-limited by the Auger process and the detection efficiency and not limited by primary beam noise. The results are shown in Figure 7-22. In this figure, the S/N at three different primary beam currents was taken from the Auger dN/dE plots. As described in the section of this thesis on Auger S/N considerations, the signal to noise ratio of the detected Auger signal will be proportional to $\sqrt{I_p}$ for a shot noise limited primary beam. So if $(S/N)^2$ is proportional to I_p, this indicates that the process is essentially shot-noise limited.

LaB_6 cathodes were also used in a comparison of the fixed beam thermionic coaxial gun AES system and the field emission SAM. This experiment used the same primary current (50 nA) in both systems and

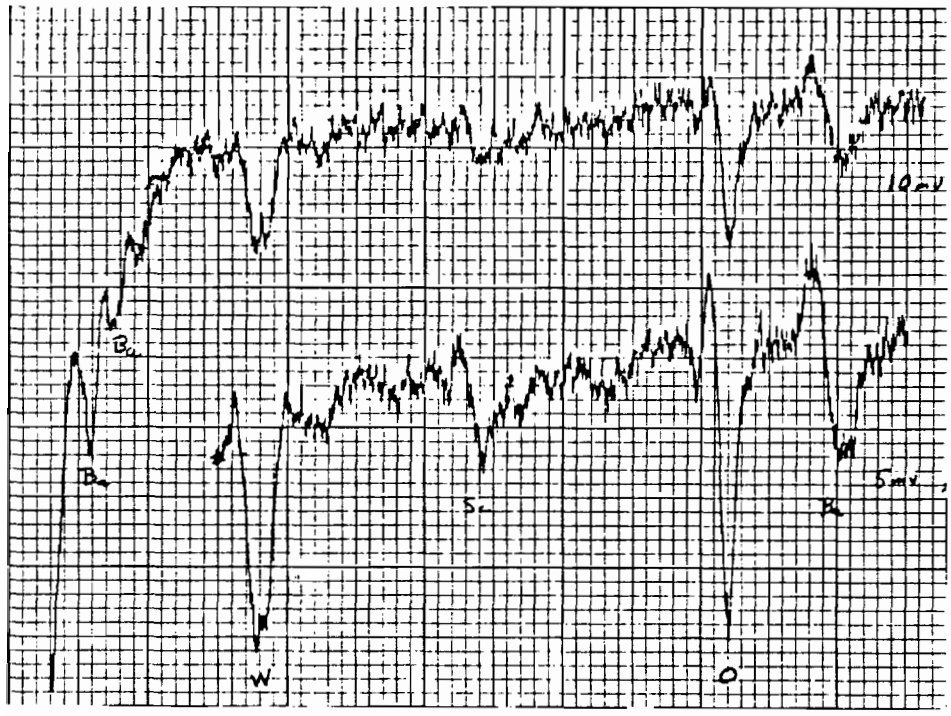

Figure 7-19. Thermally cleaned barium scandate dispenser cathode Auger specimen.

E_p	8500 V	Upper trace
I_p	25 nA	10 mV sens. .3 s time constant 4 eV/sec
V_{mod}	4 eV p-p	
V_{mult}	2100 V	Lower trace
		5 mV sens. 1 sec 1 eV/sec

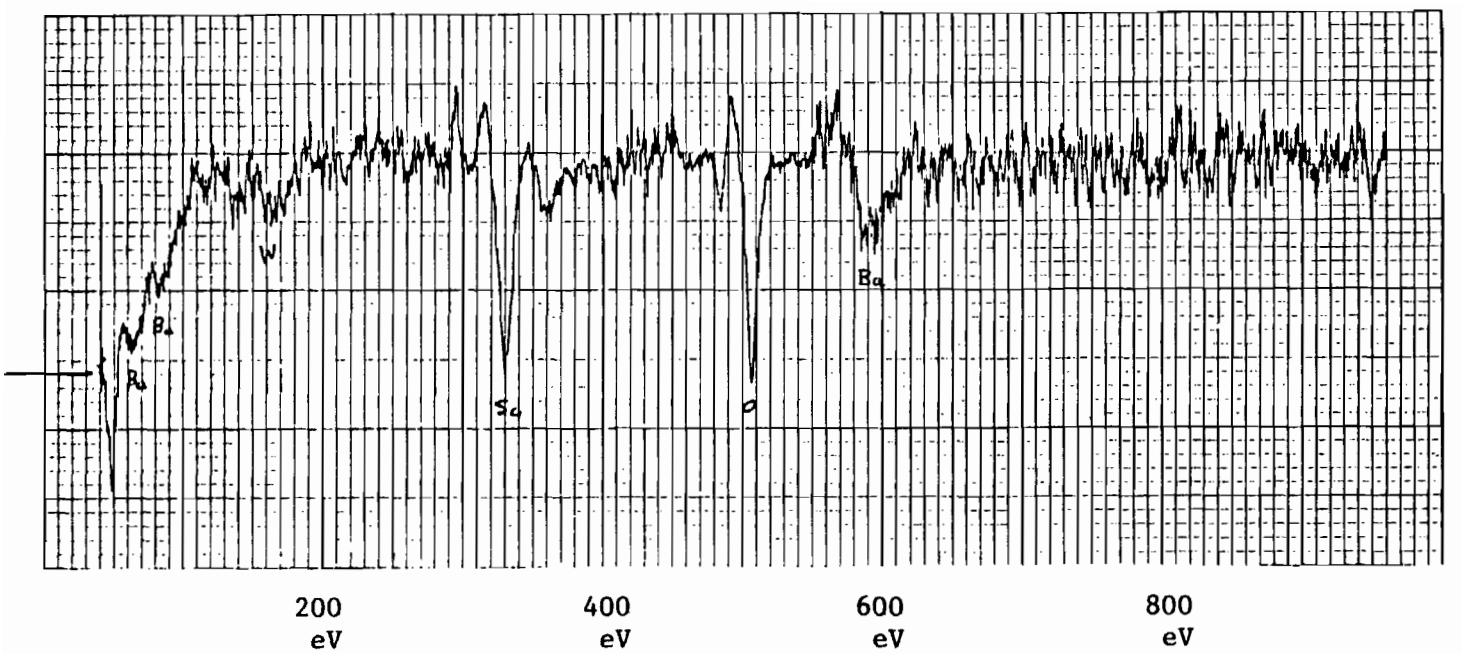

Figure 7-20. Barium scandate dispenser cathode fixed beam on unknown particle.

E_p = 8500 V	TC = .3 S	V_{mult} = 2100 V
I_p = 38 nA	4 eV/S	4 eV p-p

Lock-in Sensitivity	2 mV	5 mV	2 mV	5 mV	2 mV

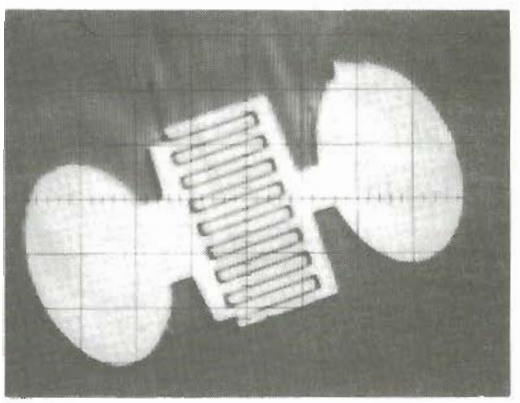

(a) GOLD ON SiO_2 SUBSTRATE

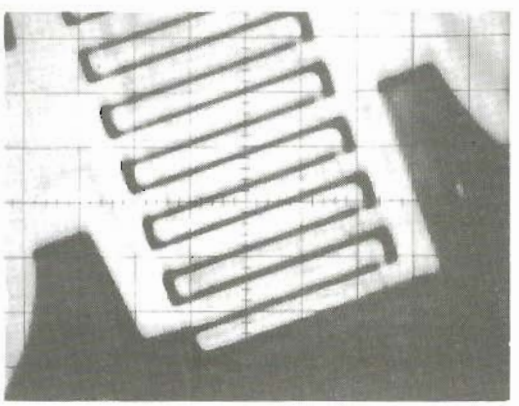

(b) MAGNIFICATION = 5 μm/div

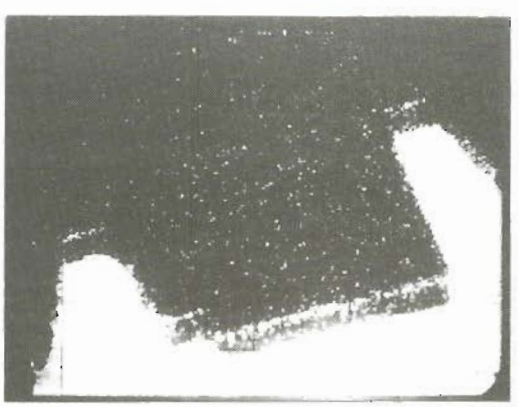

(c) ONE MINUTE SCAN-OXYGEN

Figure 7-21. Secondary electron images (a) and (b) and Auger image (c) corresponding to area in (b).

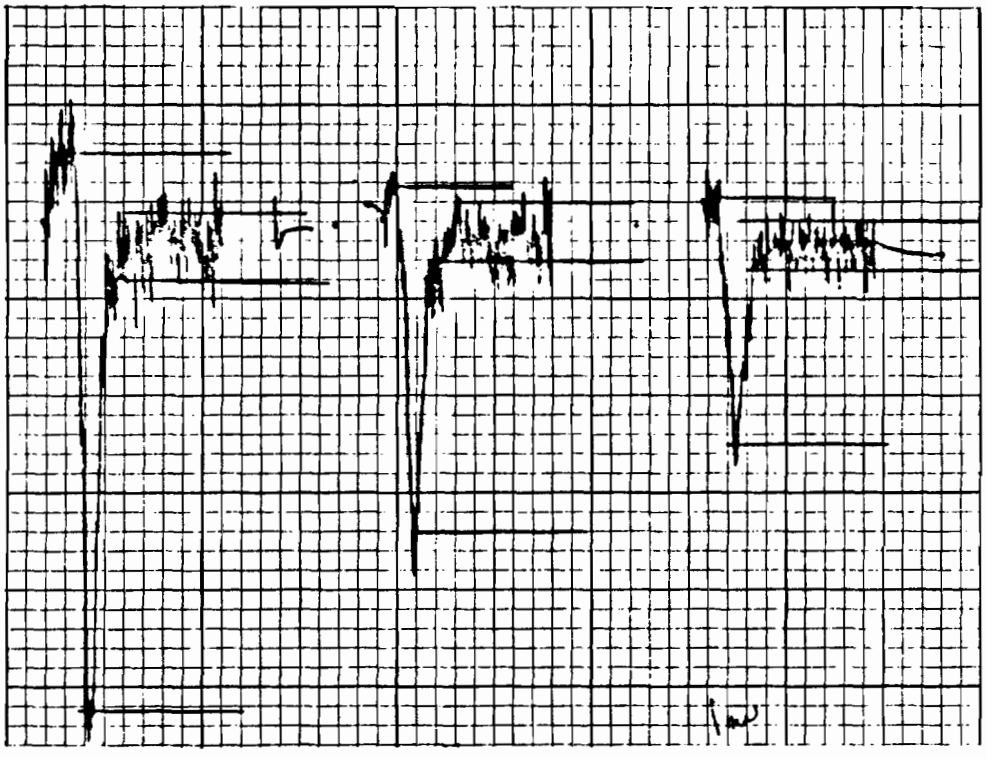

Figure 7-22. Boron peak from LaB_6 cathode Auger specimen.

I_p	90 nA	50 nA	35 nA
S/N_{p-p}	8.21	5.93	5.08
S/N Normalized	1.62	1.17	1.00
Square of S/N Normalized	2.62	1.36	1.00
I_p Normalized	2.57	1.43	1.00

measured the Auger S/N ratio. For similar system setups, the Auger S/N for the SAM was approximately five times worse than that for the fixed beam system. This result indicates that either the 90° beam-CMA geometry or the relatively high magnetic field at the specimen (~ 1 Gauss) will have to be corrected to make full use of the greater probe current available for a given resolution in the field emission SAM. There may be problems with the CMA itself which would produce a loss of signal.

REFERENCES

1. A. B. El-Kareh, J. Vac. Sci. Technol. 12, 1227 (1975).

2. L. A. Fontijn, J. Vac. Sci. Technol. 15, 1053 (1978).

3. L. W. Swanson, J. Vac. Sci. Technol. 12, 1228 (1975).

4. A. E. Bell and L. W. Swanson, Phys. Rev. B, 19, 3353 (1979).

5. T. Groves, D. L. Hammond and H. Kuo, J. Vac. Sci. Technol. 16, 1680 (1979).

CHAPTER 8

CONCLUSIONS

The objective of the construction of the scanning Auger microprobe was to determine the suitability of the Zr/W<100> TFE source in a SAM application. The current vs. spot size data indicate a performance superior to the LaB_6 thermionic cathode. A current density of 1300 A/cm^2 or power density of $1.6 \cdot 10^7$ W/cm^2 has been achieved in a 0.1 μm beam spot size. This corresponds to an image plane brightness of $5.5 \cdot 10^7$ A/cm^2sr at 12 kV. This far exceeds the SAM requirements, and can actually destroy the surface under analysis. With this current capability, the aperture could be reduced to reduce the spot size and still have plenty of current for a SAM application.

An increasing beam energy spread with current was inferred for both the high voltage and low voltage emitter, but in the case of the low voltage emitter the chromatic aberration effects on spot diameter were much greater. It appears that the higher voltage emitter displays less of the "Boersch effect" energy broadening with angular intensity.

The beam noise is greater than that of the thermionic cathode, but an explicit measurement of the effect of beam noise on the Auger signal noise was hampered by a low electron collection efficiency, which appears to be due to a problem in the CMA. Arguments based

on shot noise indicate that at the current levels detected by the CMA, the shot noise of the detected current may mask the effects of noise from the primary beam. The overall noise level of an Auger system using a given primary beam current on the order of tens of nanoamps may therefore be much more affected by the transmission of the CMA than by primary beam noise.

The beam noise spectrum shows a "knee" at ~ 200 Hz, with an approximately constant spectral density from 2 to 200 Hz and 1/f behavior beyond 200 Hz. There is a large low frequency noise (< 2 Hz) in the probe current which varies approximately as $1/f^2$ and which is completely coherent with the noise detected in the total (anode) current. This suggests that thermal fluctuations may contribute to the low frequency noise, while emitter surface condition fluctuations contribute to the high frequency noise.

The total noise in the beam is reduced by increasing the aperture size, as would be expected for a noise process occurring due to surface work function fluctuations. The low frequency noise in the beam increases with aperture angle, however, but further measurements are necessary to determine if this is an artifact of the magnetic focusing technique for changing the aperture angle.

The geometric stability of the emitter structure is excellent once it achieves equilibrium temperature. Measurements show the emitter drift over 16 h periods to be < 0.05 μm/h for the TFE emitter operating at 1800 K.

The capabilities of an electron optical system based on the Zr/W<100> TFE electron source suggest several other applications, some of which have already been realized. The long working distance permits a large scanned field with low deflective aberrations. For such applications as electron beam lithography and electron beam addressable archival memories the large working distance is important and this distance is a direct result of using a source with small virtual size.

The small virtual source also implies a high degree of spatial coherence in the quantum mechanical wave function of the electron beam. Therefore, electron beam holography and electron interference experiments are possible with a reasonable beam current.

The high current sensity in a small spot produced by the thermal-field emission system is useful in applications where an electron stimulated event produces a low quantum yield, so that the S/N ratio is highly dependent on the primary beam current. In addition to Auger spectroscopy, other processes include x-ray spectroscopy, characteristic loss spectroscopy and electron stimulated desorption.

Stroboscopic scanning electron microscopy involves beam blanking with a typical duty cycle of 1% or less. This technique requires a large beam current since the effective current seen on the specimen surface is 1% or less of the steady-state beam current.

The power density in the electron beam is useful in such applications as controlled annealing of silicon and e-beam machining.

VITA

The author was born in Portland, Oregon on October 30, 1946. His public school education was completed in Portland schools where he graduated from Benson High School in 1964. After a year at Portland State University, the author made a big mistake by joining the Navy for six years, during which time he became an electronics technician and a nuclear reactor technician in the submarine service and a semi-vegetable. After being released, the author completed his undergraduate education at Oregon State University, receiving a B.S. in Physics in 1974, at which time he immediately bought a commercial fishing boat which turned out to be a mistake also, although not as bad as the first one. After the first fishing season, the author got a job at Tektronix where he worked until starting his graduate education in 1976 at the Oregon Graduate Center.

Publications by the author are:

D. Tuggle, L. W. Swanson, and J. Orloff, "Application of a thermal field emission source for high resolution, high current e-beam microprobes," J. Vac. Sci. Technol. 16, 1699 (1979).

L. W. Swanson and D. Tuggle, "Recent progress in thermal field electron source performance," Appl. Surf. Sci. (in press).

L. W. Swanson and D. W. Tuggle, "High Brightness Electron Source Investigation," Hughes Research Laboratory Purchase Order S1-004499-7.